

**Universität
Rostock**



Traditio et Innovatio

Synthesis and Characterization of Magnetic Nanoparticles for Bioactive Bone Implant Materials

Dissertation

zur Erlangung des akademischen Grades

doctor rerum naturalium (Dr. rer. nat.)

der Mathematisch-Naturwissenschaftlichen Fakultät

der Universität Rostock

vorgelegt von

Marcel Benjamin Wetegrove, geb. am 21. Oktober 1991 in Reinbek

Rostock, den 26. April 2019

https://doi.org/10.18453/rosdok_id00002532

Betreuer und 1. Gutachter: Prof. Dr. Eberhard Burkel
Institut für Physik
Universität Rostock

2. Gutachterin: Prof. Dr. Sylvia Speller
Institut für Physik
Universität Rostock

Datum der Einreichung: 26.04.2019

Datum des Kolloquiums: 24.07.2019

Teilergebnisse der vorliegenden Arbeit wurden vorab publiziert in: M. Wetegrove, K. Witte, W. Bodnar, D.-E. Pfahl, A. Springer, N. Schell, F. Westphal, E. Burkel. Formation of maghemite nanostructures in polyol: tuning the particle size via the precursor stoichiometry. *CrystEngComm*, 21:1956-1966, 2019

Abstract

This work presents the development of a poly(methyl methacrylate) based composite coating containing magnetic nanostructures that has the potential to equip passive titanium-based bone implants with the functionality of exercising an electromagnetic stimulus on bone regeneration. To achieve this, the thermal synthesis of maghemite nanoflowers is investigated, using iron(II) and iron(III) chlorides in the presence of sodium hydroxide in a solvent mixture of N-methyldiethanolamine and diethylene glycol. The aggregation process leading to the formation of nanoflowers showing cooperative magnetic behaviour is examined by varying synthesis conditions such as temperature, synthesis duration and precursor concentrations. Samples are characterized using transmission electron microscopy, AC susceptometry, high energy X-ray diffraction and Mössbauer spectroscopy. The stoichiometric ratio of Fe^{2+} and Fe^{3+} ions is varied in the precursor solution and it is shown to have a strong influence on particle and crystallite sizes, and thereby on the magnetic properties. Stable, mostly monodisperse suspensions of multicore particles with diameters ranging from 18.4 nm to 28.7 nm are obtained, featuring magnetic moments $(0.8 \pm 0.1) \text{ A} \cdot \text{nm}^2$ to $(3.7 \pm 0.5) \text{ A} \cdot \text{nm}^2$. The enhanced magnetic properties of nanoflowers are illustrated by comparison with single-core particles. Finally, a coating routine is developed to obtain a thin polymer film containing evenly dispersed magnetic nanoflowers. Layer thickness and roughness are measured by atomic force microscopy and the final coating is investigated by scanning electron microscopy.

Zusammenfassung

In der vorliegenden Arbeit wird die Entwicklung einer Polymethylmethacrylat-basierten und magnetische Nanostrukturen enthaltenden Kompositbeschichtung präsentiert, die das Potential hat, Titan-basierte Knochenimplantate mit der Funktionalität auszustatten, Knochenregeneration elektromagnetisch zu stimulieren. Um dies zu erreichen, wird die thermische Synthese magnetischer Nanoflowers mittels Eisen(II)- und Eisen(III)chlorid in der Gegenwart von Natriumhydroxid und einer Mischung der Lösungsmittel N-Methyldiethanolamin und Diethylenglycol untersucht. Der Aggregationsprozess, der zur Bildung von Nanoflowers mit kooperativem magnetischem Verhalten führt, wird untersucht, indem Synthesebedingungen wie Temperatur, Synthesedauer und Konzentrationen der Ausgangsstoffe variiert werden. Die Proben werden mittels Transmissionselektronenmikroskopie, Dynamischer Suszeptometrie, Hochenergie-Röntgendiffraktion und Mössbauerspektroskopie charakterisiert. Das stöchiometrische Verhältnis der Fe^{2+} und Fe^{3+} -Ionen der Ausgangsstoffe wird variiert und dessen starker Einfluss auf Partikel- und Kristallitgrößen, sowie auf die magnetischen Eigenschaften nachgewiesen. Stabile, hauptsächlich monodisperse Suspensionen von multicore Partikeln mit Durchmessern zwischen 18.4 nm und 28.7 nm und magnetischen Momenten zwischen $(0.8 \pm 0.1) \text{ A} \cdot \text{nm}^2$ und $(3.7 \pm 0.5) \text{ A} \cdot \text{nm}^2$ werden hergestellt. Der Vergleich mit single-core Partikeln illustriert die überlegenen magnetischen Eigenschaften der Nanoflowers. Schließlich wird eine Beschichtungsroutine entwickelt, die gleichmäßig verteilte Nanoflowers in einen dünnen Polymerfilm einbettet. Schichtdicke und Oberflächenrauigkeit werden mittels Rasterkraftmikroskopie gemessen, die endgültige Beschichtung wird rasterelektronenmikroskopisch untersucht.

Contents

| | |
|--|-----------|
| Motivation | 1 |
| Introduction | 7 |
| 1 Physics and biomedical applications of magnetic nanoparticles | 7 |
| 2 Synthesis of maghemite nanoflowers | 11 |
| 3 Choice of composite coating | 14 |
| 4 Choice of characterization methods | 15 |
| Methods and experimental details | 17 |
| 1 Electron microscopy | 17 |
| 1.1 Transmission electron microscopy | 17 |
| 1.2 Scanning electron microscopy | 18 |
| 2 X-ray diffraction | 19 |
| 2.1 Synchrotron radiation | 20 |
| 2.2 Rietveld refinement | 22 |
| 3 Mössbauer spectroscopy | 23 |
| 4 AC susceptometry | 28 |
| 5 Atomic force microscopy | 30 |
| Results | 35 |
| 1 Synthesis and optimization of magnetic nanoflowers | 35 |
| 1.1 Investigation of synthesis parameters | 36 |
| 1.2 Variation of the precursor stoichiometry | 39 |
| 2 Comparison with spherical iron oxide nanoparticles | 48 |
| 2.1 Magnetic properties in dependence of the particle size | 48 |
| 3 Preparation and optimization of polymer coatings | 53 |
| 3.1 Single dip coatings on glass substrate | 53 |
| 3.2 Double dip coatings on glass substrate | 57 |
| 3.3 Application of magnetic nanoflowers to titanium surfaces | 59 |

| | | |
|-----|--|-----------|
| 3.4 | Composite coatings on titanium substrate | 63 |
| | Discussion | 69 |
| | Conclusions | 77 |
| | Outlook | 81 |
| | Appendix | 83 |
| 1 | Magnified TEM image | 83 |
| 2 | Mössbauer fit parameters | 84 |
| | Bibliography | 87 |

Motivation

Every year in Germany, a few hundred thousand implantations are undertaken to replace a patient's joint with an artificial prosthesis [1], as illustrated in figure 1. The majority of these operations - more than a half - is related to the replacement of the hip joint. Replacements of the knee joint account for just over 40 % of operations. The rest is divided up between the joints of the upper and lower extremities. The numbers of operations show a tendency to increase which is arguably connected with the demographic development of an ageing society. Joint replacement offers tremendous benefits such as the maintenance or the restoration of mobility, relief of pain and disability [2, 3]. Nevertheless, there is a risk of implant failure owing to a lack of stability, inflammation or complications caused by abrasion products [4, 5]. In order to achieve a long-lasting, optimal osseointegration of orthopaedic implants, the development of new implant materials, surface modifications and implant designs is needed.

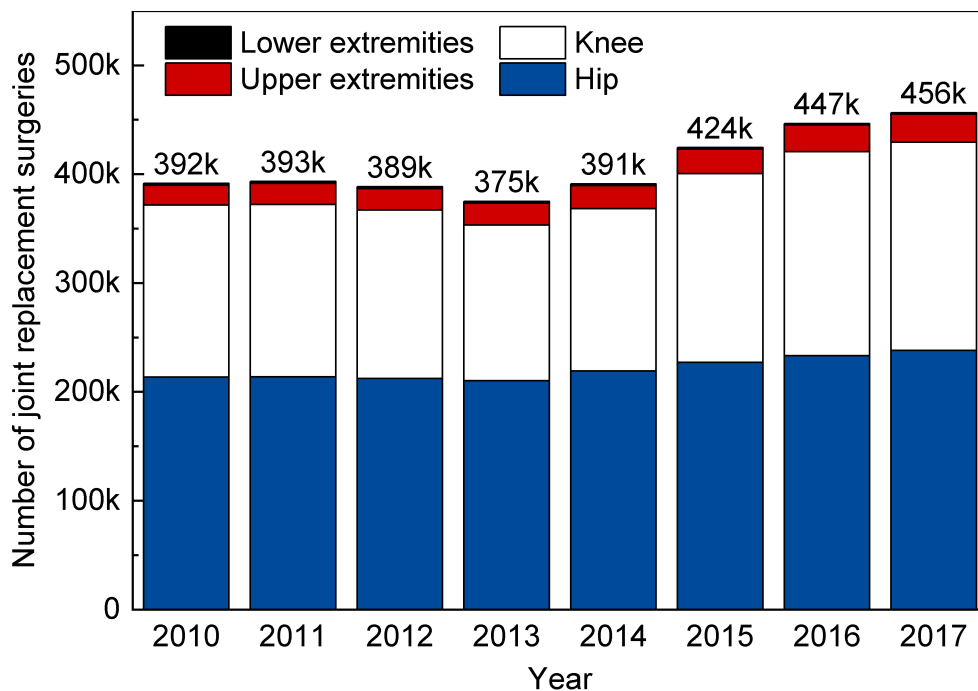


Figure 1: Number of primary implantations of joint prostheses in Germany per year. Data taken from [1].

For the assessment of potential implant materials, a number of parameters need consideration. The most fundamental requirement is biocompatibility, meaning that any substances are released from the implant in non-toxic concentrations [2]. A biocompatible implant is integrated into a layer of connective tissue. A bioinert implant, on the other hand, releases no toxic substances at all and is healed into the bone, causing no reaction of the tissue [2]. Biocompatibility is not only determined by the chemical composition of a material, but also by biomechanical properties such as wear and corrosion resistance and elasticity [6, 7]. The ultimate aim is to achieve a strong bond between implant and bone, minimizing any movement between the two. This is often achieved by materials mimicking structural features and properties of natural bone [5].

Titanium and titanium-based alloys are the most commonly used load-bearing bone implant materials thanks to their good mechanical stability, corrosion resistance, low density and good biocompatibility [7]. The adhesion of bone with the implant strongly depends on surface roughness and porosity. It was observed that a network of interconnected pores with diameters between 200 μm and 500 μm , at a porosity of 50%, provides good conditions for bone ingrowth, allowing the migration of cells and the circulation of nutrients and waste products [7]. Titanium-based foams with a pore structure in this regime have been prepared using the field-assisted sintering technique (FAST), achieving a modulus of elasticity similar to that of natural bone [8, 9, 10].

While titanium based implant materials are well-established providers of structural and load-bearing functionality, they are limited to playing a passive role in bone regeneration. A bioactive implant material, on the other hand, exhibits a positive interaction with bone, allowing tissue differentiation and the formation of bone at the bone-implant interface [2]. In a lifelong remodelling process, bone is being formed by osteoblast cells and resorbed by osteoclast cells. It takes place in healthy bone, but is also responsible for the healing of fractures. The regeneration of bone is not a random process. According to Wolff's law, bone is able to respond to mechanical stress by selectively increasing bone density in order to resist this stress [11]. Bone shows piezoelectric behaviour [12] which is the main cause for electric strain generated potentials in bone. These potentials are a possible trigger for the deposition of new bone [13].

However, immediately after the implantation of a bone prosthesis, patients suffer a limitation of mobility, causing a reduction of mechanic loading and therefore reducing the stimulus that would trigger bone regeneration. This makes it desirable to develop implant systems that can actively stimulate bone regeneration using electromagnetic fields. The effectiveness of electrical stimulation of bone regeneration has been shown by numerous studies [14, 15, 16, 17]. The design of suitable stimulation devices and also the optimization of stimulation parameters are topics of ongoing research [18, 19]. There are three main types of stimulation devices [20, 21, 22]: Stimulation via direct current operates with implanted electrodes driven by either an implanted or an external power source, delivering currents of 5 μA to 100 μA [22]. Capacitive coupling stimulation makes use of electrodes placed externally on the skin at opposite sides of the target site, providing an alternating electric field of 1 mV/cm to 100 mV/cm

[20]. Inductive coupling stimulation is another externally applied method, generating variable or pulsed electromagnetic fields with a coil, producing magnetic fields of 0.01 mT to 2 mT and inducing electric fields in the tissue ranging from 1 mV/cm to 100 mV/cm [21].

For the development of new bone implants, it is desirable to realize electromagnetic stimulation without the need of an internal or external stimulation device, but rather as an intrinsic property of the implant. Thus, the goal of the present work is to develop a surface coating that has the potential to equip passive titanium-based bone implants with a bioactive functionality. As shown schematically in figure 2, the porous surface of a titanium-based alloy being the structural and load-bearing component receives a composite coating containing magnetic nanoparticles embedded in a protective polymer coating. Magnetic nanoparticles have a permanent magnetic dipole moment that below a certain particle size limit exhibits a random flipping of its orientation due to thermal effects [23]. Therefore, variable electromagnetic fields can be permanently induced on the implant surface. It is worth mentioning that such an implant system can alternatively be triggered by an external electromagnetic stimulation device.

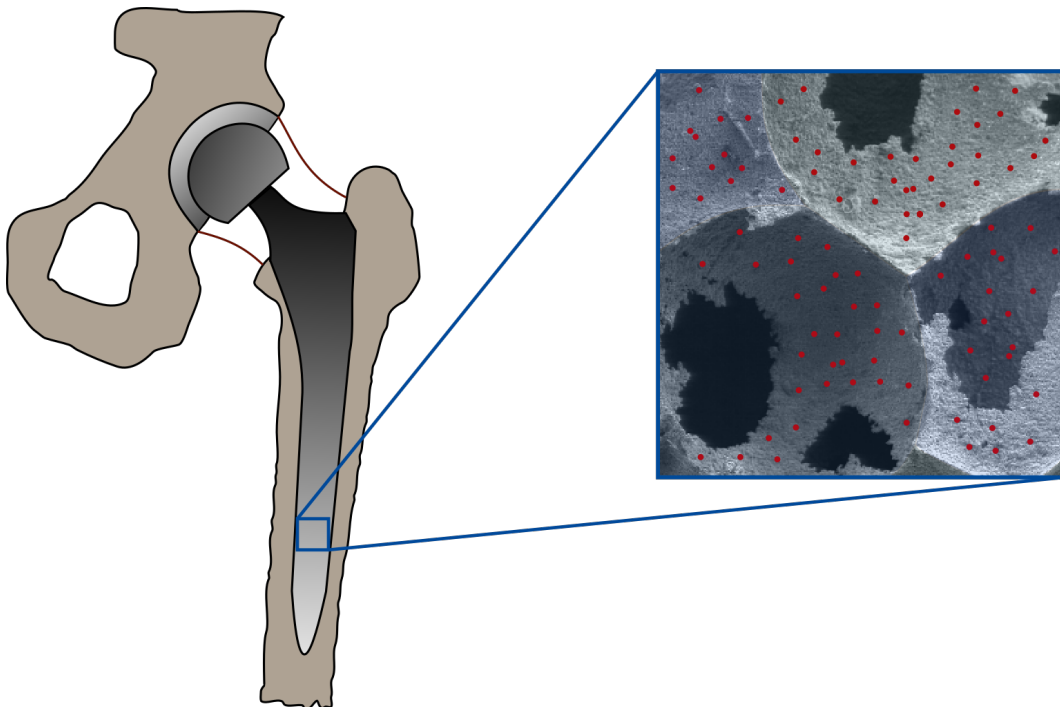


Figure 2: Schematic depicting the bone implant system presented in this work. A porous titanium-based alloy [9] provides structural and load-bearing functionality (shown as a greyscale image). A composite coating containing magnetic nanoparticles (shown in red) and a protective polymer layer (shown as blue overlay) are applied to achieve bioactive functionality using electromagnetic stimulation of bone regeneration.

In the following, the working principle of the implant system presented in this work is illustrated by estimating the achievable electromagnetic stimulus. A temporally variable magnetic field \vec{B} induces an electric vortex field \vec{E} :

$$\vec{\nabla} \times \vec{E} = -\frac{\partial \vec{B}}{\partial t}$$

For simplicity, a rotating magnetic dipole is assumed with a rotation period $T = 2\tau$, where τ is the average time between two flips of the magnetic moment's direction, called relaxation time. The electric field induced by a rotating magnetic field is

$$\vec{E}(\vec{r}) = -(\vec{\omega} \times \vec{r}) \times \vec{B},$$

where \vec{r} is the distance vector between the origin of the magnetic field and a given location and ω is the angular velocity of the rotation. The magnetic moment $\vec{\mu}$ at the origin generates the magnetic field $B(\vec{r})$:

$$\begin{aligned} \vec{B}(\vec{r}) &= \frac{\mu_0}{4\pi} \left(\frac{3\vec{r}(\vec{\mu} \cdot \vec{r})}{|\vec{r}|^5} - \frac{\vec{\mu}}{|\vec{r}|^3} \right) \\ &= \frac{\mu_0}{4\pi|\vec{r}|^3} \left(3 \cdot (\vec{\mu} * \hat{r})\hat{r} - \vec{\mu} \right). \end{aligned}$$

The maximum magnetic field B_{\max} at a given distance r from its origin is in its rotational plane (where $\vec{\omega} \perp \vec{r} \parallel \vec{B}$):

$$B_{\max} = \frac{\mu_0 \mu}{2\pi r^3}.$$

Assuming a period of the rotation $T = 2\tau$, with $\omega = \frac{2\pi}{T}$, the maximum electric field is

$$E_{\max} = \frac{\mu_0 \cdot \mu}{2\tau r^2}.$$

For the effective value of a sinusoidal signal, one obtains:

$$\begin{aligned} E_{\text{eff}} &= \frac{E_{\max}}{\sqrt{2}} = \frac{\mu_0 \cdot \mu}{2\sqrt{2}\tau r^2}, \\ B_{\text{eff}} &= \frac{B_{\max}}{\sqrt{2}} = \frac{\mu_0 \mu}{2\sqrt{2}\pi r^3}. \end{aligned}$$

A typical value for the magnetic moment of such a nanoparticle is $\mu = 2 \text{ A} \cdot \text{nm}^2$ [24]. The effective electric and magnetic field strength for a rotating magnetic dipole with $\mu = 2 \text{ A} \cdot \text{nm}^2$ is plotted in dependence of the relaxation time τ for different distances from the origin r in figure 3. The electric field regime from 1 mV/cm to 100 mV/cm which is viable for the stimulation of bone regeneration [17, 21], is reached for relaxation times in a microsecond to nanosecond range (or equivalent external driving frequencies). Magnetic fields between 0.01 mT and 2 mT, as commonly used in electromagnetic stimulation [21], are exceeded in close proximity to a particle.

Depending on the distribution of magnetic nanoparticles on the implant surface, the superposition of field contributions from neighbouring particles may lead to a stronger stimulus. For the development of a composite coating with the functionality of exercising an electromagnetic stimulus on bone regeneration, it is important to adjust the properties of magnetic nanoparticles, maximizing their magnetic moment μ and tuning the relaxation time τ in dependence of the desired frequency regime.

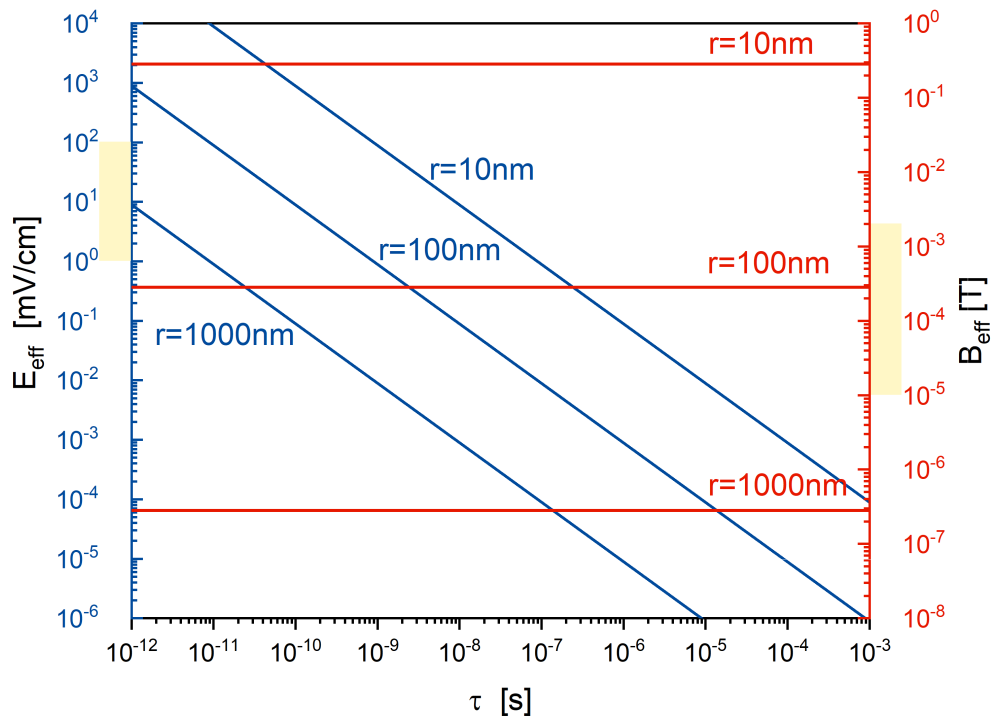


Figure 3: The effective electric and magnetic fields E_{eff} and B_{eff} are plotted in dependence of the relaxation time τ for different distances r . The intervals from 1 mV/cm to 100 mV/cm and from 0.01 mT to 2 mT are marked yellow.

Introduction

1 Physics and biomedical applications of magnetic nanoparticles

The term magnetic nanoparticles refers to nanoscale particles, i.e. particles in a size regime ranging from 1 nm to 1000 nm in at least one dimension, containing ferromagnetic or ferrimagnetic materials. These materials are characterized by an ordering of elementary magnets which is permanent without the presence of an external magnetic field and by the existence of domains, being regions of uniform magnetization separated by domain walls [25]. Particles of a sufficient size therefore contain a number of magnetic domains and are called multidomain particles, showing a hysteresis, remanence and coercivity close to bulk values. Domain magnetizations are not necessarily aligned, leading to a weakening of the external magnetic stray field [26]. Below a certain size limit D_C , the energy needed for the formation of domain walls exceeds the energy required to support an increased external magnetic stray field of a single domain particle [27]. At this point, a transition from multidomain to single domain particles is observed, with coercivity reaching its maximum (see figure 1). In this size regime, magnetization reversal takes place by rotation of spins inside the material rather than by moving domain walls. This, as well as shape anisotropy, is a reason for the high coercivity [27]. When particle size is further decreased, coercivity drops to zero at the transition to the superparamagnetic state. At this point, the anisotropy energy barrier KV reaches the same order of magnitude as the thermal energy $k_B T$. The magnetic anisotropy energy E is

$$E = KV \sin^2 \theta,$$

with the anisotropy constant K , particle volume V and angle θ between anisotropy axis and magnetization [28]. In the superparamagnetic state, thermal energy allows the flipping of the magnetization vector around the particle's easy axis [23]. The temperature above which superparamagnetism occurs is called blocking temperature. Superparamagnetic nanoparticles show a behaviour similar to a huge paramagnetic atom with a large magnetic moment, while remanence and coercivity are close to zero [27]. For iron oxide nanoparticles, this limit is typically encountered around 10 nm particle size [29]. The process of reaching an energetic minimum after perturbation is referred to as relaxation. The time between two such orientation changes of the

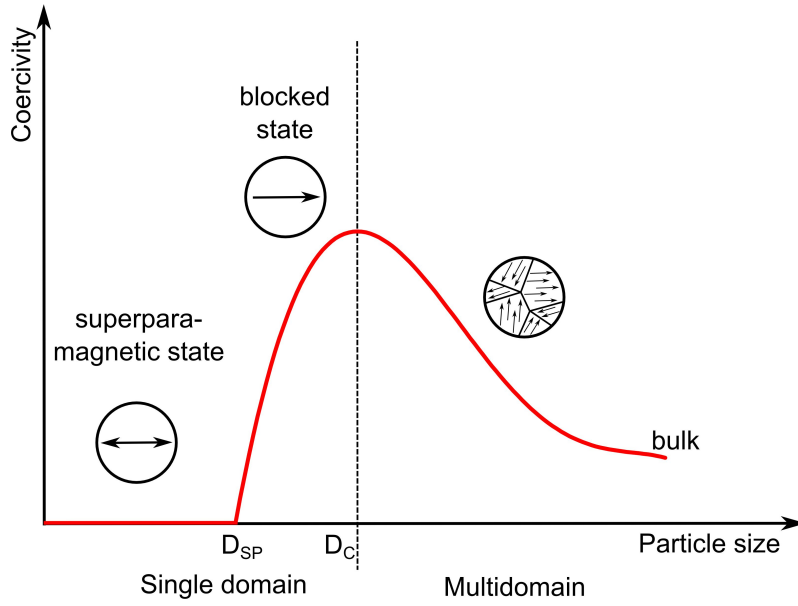


Figure 1: Coercivity of magnetic nanoparticles is shown in dependence of the particle size. Critical sizes for the transition between multidomain and single domain particles D_C and for the transition between the blocked and the superparamagnetic state D_{SP} are marked. Image source: [23].

magnetization vector is characterized by the Néel relaxation time τ_N [30],

$$\tau_N = \tau_0 \cdot e^{\frac{KV}{k_B T}},$$

with anisotropy energy barrier KV , thermal energy $k_B T$ and the attempt time or time constant τ_0 which is in the order of 10^{-9} s [23, 28]. It has to be noted that superparamagnetic behaviour can only be observed if the characteristic time constant of the measurement is smaller than the superparamagnetic relaxation time. Therefore, the observation of the transition from the blocked state to the superparamagnetic state is always related to a distinct observation method.

Suspended particles are subject to Brownian motion. The random rotation away from the magnetization direction is described by the Brownian relaxation time t_B [31, 32]:

$$\tau_B = \frac{4\pi r_H^3 \eta}{k_B T},$$

where r_H is the hydrodynamic radius of a particle, η is the viscosity of the liquid phase, k_B is the Boltzmann constant and T the temperature. Obviously, particle size is a crucial factor influencing both Néel and Brownian relaxation times. A distribution of particle sizes will also cause a distribution of relaxation times. Besides this, in most samples, interactions between particles are not neglectable [33]. The two main types of inter particle interactions are dipole-dipole interactions and exchange interactions between particles in direct contact [28].

Magnetic nanoparticles can be further categorized into single core and multicore particles. While a single core particle is a single-domain crystal, multi-core particles contain multiple single-domain crystals [34]. Besides changed hydrodynamic properties, organization in multicore structures leads to cooperative magnetic behaviour due to interactions between the cores [34, 35]. The magnetic moment of a multicore particle is the vector sum of the magnetic moments of all single domains contained (see figure 2) [36]. The magnetic moments of single domains in multicore structures are not oriented randomly but show partial alignment, leading to an increased magnetic moment [34]. Flower-shaped superstructures, so-called magnetic nanoflowers, are densely packed aggregates of (iron oxide) crystallites [37]. Inspired by particle morphology, the term nanoflower is not restricted to magnetic iron oxide nanoparticles, but can be generalized to nanostructures of various inorganic compounds sharing a roughly similar morphology [38]. Magnetic nanoflowers often show irregular shapes due to their formation in an aggregation process [37], during which primary particles may align with parallel crystallographic orientation minimizing surface free energy [39, 40]. However, such alignment may be only partial [34]. Generally, magnetic nanoflowers can be described as polycrystalline superstructures composed of single crystalline primary particles [37]. These primary particles are individual magnetic cores but show cooperative magnetic behaviour within the multicore superstructure, leading to magnetic properties different from both bulk and single-core behaviour [40, 41]. On one hand they show little remanence, similarly to superparamagnetic particles, making them highly dispersible. On the other hand in the presence of an external magnetic field, a ferrimagnetic hysteresis is observed (see figure 3). This effect is referred to as superferrimagnetism [42]. Stray fields of these clusters are enhanced compared to the stray fields of their superparamagnetic primary particles [43].

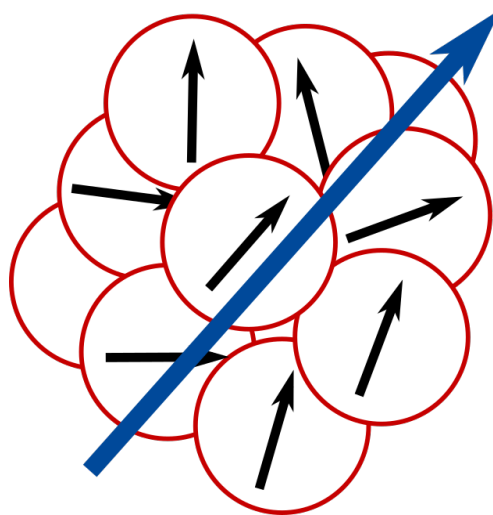


Figure 2: Schematic picture of a magnetic nanoflower showing the nanoflower's effective magnetic moment (blue) being the vector sum of the primary particle's magnetic moments (black).

Magnetic nanoparticles have various applications in biomedicine such as magnetic separation, drug delivery, magnetic hyperthermia treatment and as contrast agents in magnetic resonance imaging [44, 45, 46]. Magnetic hyperthermia uses heat generated by magnetic nanoparticles in response to an alternating external magnetic field. These heating losses are caused by a number of processes [47]. For magnetic hyperthermia used for cancer treatment, Brownian heating due to the physical rotation of particles and hysteresis heating are most viable [47]. As a consequence, the heating power of a particle depends on its size, shape and coercivity. In magnetic particle imaging, magnetic nanoparticles act as tracers inside the biologic tissue and are directly detected by exposure to a magnetic drive field in the radio frequency regime [48]. A static magnetic field, called selection field, is superimposed to the drive field, forcing all particles outside a field free point into a state of magnetic saturation and thereby suppressing their response to the drive field [48]. The field free point can be moved to collect a spatial image. This method relies on the magnetization behaviour of superparamagnetic nanoparticles showing a saturation behaviour in strong external magnetic fields but no remanence or coercivity. It is desirable that magnetic nanoparticles for this application have a high degree of monodispersity and uniformity both in size and shape [49].

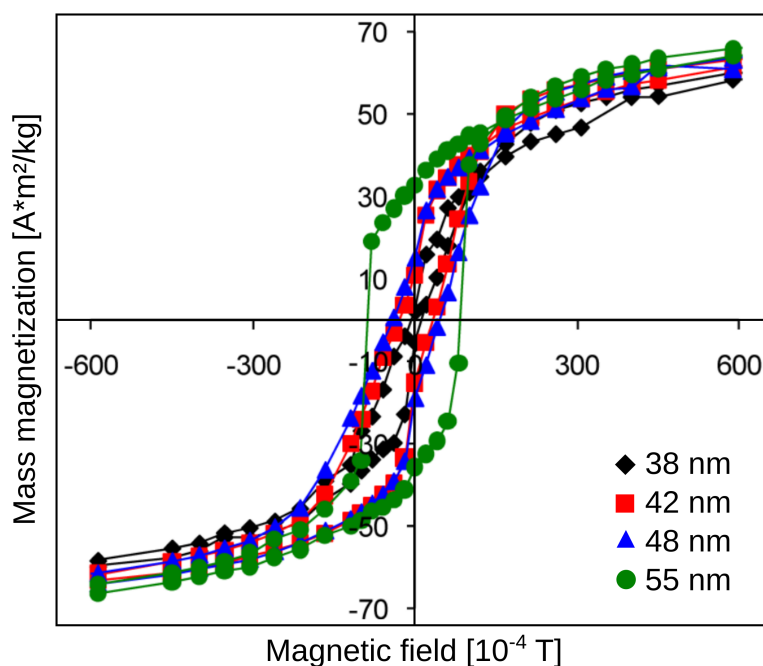


Figure 3: Hysteresis loops measured at 200K for iron oxide nanoflowers of different sizes. Image taken from [50] with modifications.

Ferrimagnetic iron oxides such as maghemite ($\gamma\text{-Fe}_2\text{O}_3$) and magnetite (Fe_3O_4) are suitable materials for these applications [46, 51]. With a wide range of synthesis methods, it is possible to tailor the properties of these particles with respect to their magnetic relaxation behaviour, their colloidal stability in hydrophilic or lipophilic solvents, their

lifetime in organisms and their functionality [27, 44]. Iron oxide multicore structures are particularly promising candidates for applications in hyperthermia treatment and magnetic particle imaging. They show enhanced magnetic properties due to collective magnetic behaviour including increased susceptibility, heating power and relaxivity [40]. For the purpose of this work, magnetic nanoflowers are of particular interest due to their enhanced magnetic moments and their resulting strong external stray fields. Besides this, their relaxation time can be tuned via the particle size [52].

2 Synthesis of maghemite nanoflowers

Maghemite ($\gamma\text{-Fe}_2\text{O}_3$) is a trivalent form of iron oxide and is most stable in a tetragonal crystal lattice configuration [53]. Iron atoms are found at tetragonal and octahedral sites (see figure 4). Some of these octahedral sites contain vacancies. In the case of randomly distributed vacancies, the crystal structure of maghemite could be described by a cubic lattice. In the case of vacancy ordering, vacancies are distributed only over a certain set of octahedral sites [53]. This crystal structure can be described by a supercell of three cubic cells which in the fully ordered configuration has the space group $P4_12_12$ [54]. Lattice parameters for this tetragonal structure are $a = 8.332 \pm 0.001 \text{ \AA}$ and $c = 25.113 \pm 0.006 \text{ \AA}$ [55].

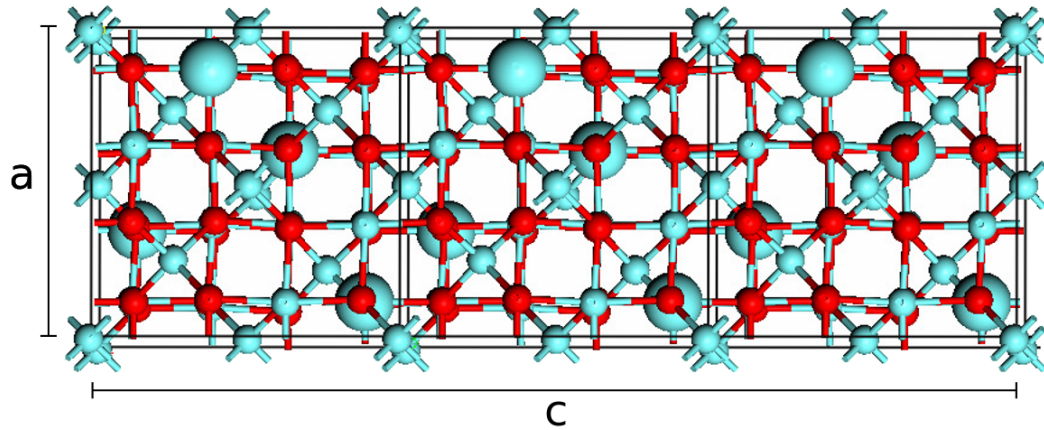


Figure 4: Schematic of the crystal structure of $\gamma\text{-Fe}_2\text{O}_3$ (maghemite) in its tetragonal configuration, being a supercell containing a stack of three cubic cells. Iron atoms are shown in blue, oxygen atoms in red. Out of the 12 iron sites marked by larger spheres, 4 are populated with iron atoms, the remaining 8 sites are vacancies. Image source: [53].

Maghemite is ferrimagnetic at room temperature and shows superparamagnetic behaviour approximately below 10 nm particle size [29]. It is formed by oxidation of magnetite (Fe_3O_4), by heating of lepidocrocite ($\gamma\text{-FeO(OH)}$) or by thermal decomposi-

tion of organic complexes [29]. The formation of multicore structures is possible by self-assembly. Synthesis routes include the thermal decomposition of iron complexes [56, 57] and the polyol assisted hydrolysis of iron salts [41, 43]. These methods have in common the use of surfactants. The reduction of surface free energy is a main driving force for aggregation and superstructure formation [39, 41]. For this reason, the choice of solvents and surfactants is decisive with respect to their polarity and viscosity. The term polyol refers to polyhydric alcohols such as ethylene glycol or propylene glycol and etherglycols such as diethylene glycol or triethylene glycol [58]. In a broader sense, any organic compounds containing multiple hydroxyl groups may be described as polyols. Polyol based synthesis methods deliver particles uniform in shape and with a narrow size distribution while allowing excellent control over particle size and morphology [58]. The synthesis of solid particles takes place by precipitation from solution, precursors may dissolve either completely or progressively [58]. The precipitation process can be divided into two steps: nucleation and growth. A supersaturated solution of monomers is formed from which nuclei will appear if a critical monomer concentration is exceeded. This type of nucleation is referred to as burst nucleation [59, 60]. Following burst nucleation, monomer concentration drops below the nucleation barrier (see figure 5) and further nucleation is inhibited which is an essential factor for obtaining a narrow size distribution [58, 59]. The rate at which monomers are formed can be controlled either by the progressive dissolution of precursors or by equilibrium reactions involved in the formation of monomers [58]. In a second step, diffusive growth takes place by adsorption of monomers. Aggregation-based growth by coalescence of primary particles and the formation of secondary particles (superstructures) may also occur [58].

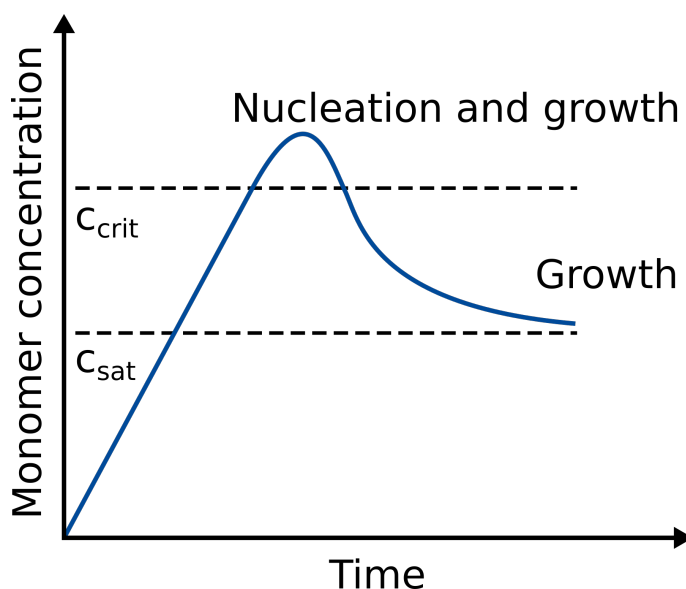
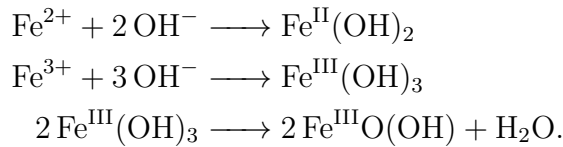


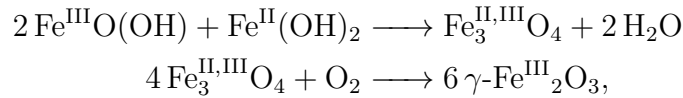
Figure 5: Monomer concentration is plotted in dependence of the reaction time with burst nucleation and growth taking place. c_{sat} is the saturation and c_{crit} is the critical supersaturation of the monomer concentration. Graph after [60].

The present work makes use of a synthesis procedure in which iron(II) and iron(III) chlorides are used to form maghemite in the presence of NaOH in a 1:1 solvent mixture of N-methyldiethanolamine (NMDEA) and diethylene glycol (DEG) near the mixture's boiling point. It was found that polyols can simultaneously act as solvents, surfactants and reducing agents for the iron precursor [41, 61]. The reducing environment provided by the polyol can therefore produce divalent iron. At the same time, at elevated temperature and in the presence of oxygen, the oxidation of iron is likely. Particle surfaces are passivated by adsorption of the solvent, preventing agglomeration and allowing excellent dispersibility in water [62].

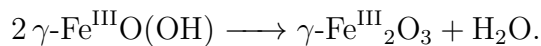
After the dissolution of iron chlorides in polyol, in the presence of hydroxyl ions, iron hydroxide and oxide-hydroxide intermediates are formed at divalent and trivalent oxidation states [63]:



The nucleation reaction leading to the formation of maghemite is not quite clear. Either magnetite is formed in a condensation reaction between iron(III) oxide-hydroxide and iron(II) hydroxide and later oxidized to become maghemite,



or iron(III) oxide-hydroxide assumes the configuration of lepidocrocite and decays to maghemite [63]:



For both of these reaction pathways, the initial ratio of iron(II) and iron(III) ions will impact the rate at which the intermediates involved in the nucleation reaction are formed. As described earlier, the rate at which monomers are formed is an important factor influencing nucleation and growth. If the first of the two reaction pathways takes place, the presence of both divalent and trivalent iron is required for nucleation. In this case, varying the ratio of iron(II) and iron(III) ions in the precursor solution opens up a particularly promising way of influencing nucleation and nanoflower formation.

Given the influence of the iron oxidation state on particle nucleation, the effect of varying the ratio of iron(II) and iron(III) chlorides in the initial precursor solution is investigated. Successful syntheses have been reported at temperatures ranging between 200°C and 220°C and at holding times from 0.5 h to 48 h [50, 63]. As observed in preliminary tests, the synthesis solution undergoes a colour change from light to dark brown along with an increase in opacity upon heating at temperatures already below 200°C. This indicates an onset of particle nucleation at lower temperatures. In order to test the onset of the reaction, further samples have been prepared at 180°C.

The solvent mixture ratio of NMDEA and DEG is crucial for nanoflower formation. When using either of these solvents alone, globular, non-aggregated particles are obtained [50, 62]. For comparison with nanoflowers, a series of samples is prepared in pure DEG as solvent, yielding primary particles in a superparamagnetic size regime.

3 Choice of composite coating

Given the versatility of magnetic iron oxide nanoparticles for applications in biomedicine, considerable efforts are being made to characterize their toxicity. The wide range of biomedical applications documents that generally a good tolerance of the organism towards magnetic iron oxide nanoparticles is assumed [51]. Accordingly, these particles can be processed by the iron metabolism which is responsible for regulating iron in the organism [51]. However, cellular alterations caused by DNA damage and oxidative stress are potential hazards [64]. The toxicity of magnetic nanoparticles depends strongly on the way of admission, area of application, particle size and surface modification [65]. Iron oxide particles in a size regime ranging from 10 nm to 100 nm are suitable for intravenous admission and are non-cytotoxic at concentrations below 10 $\mu\text{g}/\text{ml}$ [64]. Nevertheless, little is known about long-term effects and further research is needed [65].

The application of iron oxide nanoparticles proposed in this work differs fundamentally from established applications, making it very difficult to predict their toxicity when presented to the organism via a bone implant surface. Introducing a non-biodegradable composite coating helps to avoid the release of particles into the organism and therefore lowers the risk of adverse effects. Additionally, the coating offers protection from chemical degradation of particles, leading to diminished magnetic properties. This point is supported by the fact that in the organism, superparamagnetic iron oxide nanoparticles are degraded to non-superparamagnetic iron oxides [51].

As a material for a bioinert composite coating as suggested earlier, a polymer is chosen. Polymer-based materials already have various applications in biomedicine [66]. Polymer-based materials can be easily adapted to match application-specific chemical and physical properties. Tunable parameters include chain length, chemical composition of monomers, assembly of copolymers, branching and the addition of functional groups, opening up possibilities to design biomaterials capable of influencing cell differentiation and cell growth [66]. Polymer-based bone implant materials offer possibilities for drug delivery by releasing growth factors and antibiotics in a controlled manner [5, 67]. Functional groups can be added to the surface to aid cell attachment [5, 68]. After extensive literature research comparing the advantages and disadvantages of various polymers used in biomedicine, poly(methyl methacrylate) (PMMA) was chosen as a non-biodegradable polymer for the development of a composite coating (chemical structure shown in figure 6). PMMA is in use as a bone cement, responsible for the fixation of joint prostheses [67, 69]. PMMA has excellent mechanical strength, high scratch resistance, good chemical resistance towards most aqueous solutions and is non-toxic [70]. By preparing PMMA with enhanced surface roughness and modified

surface chemistry, osteoblast cell adhesion can be improved [71]. In particular, adding carboxylate and sulfonate groups to the surface increases osteoblast adhesion and inhibits bacterial adhesion [68].

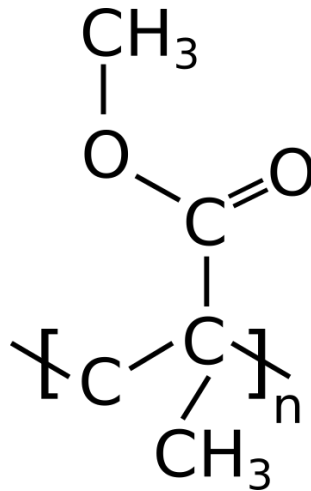


Figure 6: The chemical structure of poly(methyl methacrylate)(PMMA), shown for one repeat unit. n is the degree of polymerization.

As a coating method, dip coating is chosen. To apply thin films of PMMA by dip coating, the polymer is dissolved in acetone and the substrate, i.e. the titanium-based bone implant material, is dipped into the solution. While the substrate is withdrawn from the solution, the solvent evaporates and a PMMA layer is formed on the substrate surface. This procedure is straightforward to implement and particularly useful in combination with a three-dimensional, porous substrate structure which is no longer accessible for other coating methods such as spin coating.

4 Choice of characterization methods

The present work is divided in three main parts: The synthesis and optimization of maghemite nanoflowers, a comparison with non-aggregated primary particles and finally the preparation and optimization of a PMMA-based composite coating. In order to tailor the nanoflowers to match the requirements for the application in a bioactive coating for bone implants, a profound understanding of processes involved in the synthesis and of the structural and magnetic properties is required. The most critical parameters in this context are the magnetic moment and the relaxation time. Therefore, the first part of this work aims to investigate parameters of the polyol-assisted synthesis of maghemite nanoflowers, namely the synthesis temperature and duration, as well as the precursor stoichiometry. A series of samples is prepared under identical conditions

with a variable iron precursor stoichiometry. Particle size and morphology are characterized by transmission electron microscopy. High-energy X-ray diffraction and Mössbauer spectroscopy are used for the characterization of crystallographic and chemical phases contained in the obtained samples, including crystallite sizes. Mössbauer spectroscopy allows not only to obtain information on the chemical and crystallographic environment of iron atoms, but also gives important information on magnetic interactions and the magnetic hyperfine fields. The effect of crystallite and nanoflower size on the sample's magnetic properties, which is also visible in Mössbauer spectra, is further investigated by alternating current (AC) susceptometry, measuring the frequency dependent complex magnetic susceptibility.

The findings related to maghemite nanoflowers are then compared to spherical, non-aggregated primary particles in a superparamagnetic size regime which are characterized by transmission electron microscopy and AC susceptometry. Combining the results from these measurements, magnetic moments can be calculated and compared with the magnetic moments of nanoflowers synthesized as part of this work, as well as with literature values.

For the characterization of PMMA surface coatings, atomic force microscopy and scanning electron microscopy are employed. Topography scans are conducted from which roughness can be calculated. The layer thickness is determined by preparing cross sections. Using scanning electron microscopy, PMMA-based composite coatings containing maghemite nanoflowers are investigated. Due to the penetration depth of the electron beam, it is possible to image particles covered by a thin polymer layer, showing how particles are distributed over the titanium substrate surface.

Methods and experimental details

1 Electron microscopy

Electron microscopy makes use of the wave character of electrons in order to resolve structures which are not visible using a light microscope. By acceleration in an electric field, these electrons obtain high kinetic energies and reach de Broglie wavelengths $\lambda_{\text{de Broglie}}$ [72] much shorter than the wavelength of visible light,

$$\lambda_{\text{de Broglie}} = \frac{h}{p} = \frac{h}{\sqrt{2m_e \cdot e \cdot U_{\text{acc}} \left(1 + \frac{e \cdot U_{\text{acc}}}{2m_e c^2}\right)}},$$

where h is the Planck's constant, p is the electron's momentum, m_e the electron's mass, e the elementary charge, U_{acc} is the acceleration voltage and c is the speed of light. A shorter wavelength is equivalent to a higher resolving power of the microscope, as stated by the Abbe diffraction limit,

$$d = \frac{0.61\lambda}{n \cdot \sin(\alpha)},$$

where d is the resolving power, λ is the wavelength and $n \cdot \sin(\alpha)$ is the numerical aperture [73]. To achieve a beam of electrons with high kinetic energy, an electron source is used in combination with a strong electric acceleration field inside a vacuum chamber.

1.1 Transmission electron microscopy

In the case of the transmission electron microscope (TEM) used in this work, electrons are emitted from a LaB₆ cathode. It consists of a single crystal with a sharp tip and is heated prior to operation. A narrow beam of thermal electrons is emitted from the tip and passes an acceleration voltage in the order of usually a few hundred kilovolts. Using electromagnetic lenses, the beam is concentrated by condenser lenses and focused onto the sample quite similarly to an optical light microscope [74]. The interactions between the beam and the sample are, however, more complex: Contrast is induced by various scattering effects to a much greater extent than by simple beam absorption due to the small sample thickness. Contrast is induced by using an aperture diaphragm to remove electrons that are deflected as a result of beam-sample interaction. The following

types of interaction are responsible for contrast in TEM: Scattering contrast, caused by incoherent, elastic scattering of electrons represents the main source of contrast in amorphous samples. During the passing of the electron beam through the sample material, amplitude and phase contrast are caused by the weakening of the electron's wave amplitude due to absorption, and by a phase shift due to local variations of the diffractive index, respectively. The image contrast is caused by the interference of the waves, which obtained a phase shift or a weakened amplitude, with those that passed by a sample object without interacting. Diffraction contrast is a result of the diffraction of electrons at the crystal lattice of a crystalline sample. [75]

Samples for TEM were prepared by drop casting thinned suspensions of the respective samples onto a 300 mesh copper grid with formvar coating. Images were taken at the Electron Microscopy Centre, University Medicine Rostock, using a Zeiss Libra 120 with an acceleration voltage of 120 kV and 0.3 nm maximum resolution. For the determination of particle sizes, TEM images were evaluated with ImageJ software [76] by fitting circles around visible particles and measuring their diameter. Histograms showing the particle size distribution were fitted with normal distributions and the particle size is given as the mean value.

1.2 Scanning electron microscopy

In contrast to a transmission electron microscope, the beam in a scanning electron microscope does not cover the full sample area at once. Instead, electromagnetic condenser and focus lenses are used to focus the beam onto a spot with a diameter of approximately 1 nm to 10 nm [75]. To achieve an electron beam of such a small diameter, an electron source with a fine primary beam is necessary. The setup used for this work contains a field emitter cathode which is a fine, monocrystalline needle from which electrons are extracted by a strong acceleration voltage. In contrast to the LaB₆ crystal used in the TEM, the field emitter cathode is operated without heating. Additional deflection coils are used to move the beam over the sample surface, scanning line by line. The beam interacts with the sample surface in multiple ways. For the generation of image contrast, the formation of secondary electrons and backscattered electrons are of particular interest [77]. Backscattering describes the elastic scattering of electrons at atomic nuclei in the sample. Secondary electrons, on the other hand, originate from the interaction of the beam with the electron shells of atoms near the sample surface. These have a kinetic energy of only about 3 eV to 5 eV [75], so that only secondary electrons close to the surface can exit the sample. Those backscattered electrons and secondary electrons that leave the sample are collected by an electric field and then directed into a detector. One can distinguish between backscattered and secondary electrons that are produced by a single scattering event and those that originate from multiple scattering events. Generally, singly scattered electrons are ejected at angles close to the surface normal, while others tend to be emitted at lower angles. Therefore, the detection of these electrons emitted into the direction of the electron beam is only possible with in-lens detectors [78]. As singly scattered secondary

electrons are emitted from a smaller volume, they carry topographic information at higher resolution. The yield of singly backscattered electrons is connected with the type of surface atoms which generates a strong material contrast. The scanning electron microscope in this work uses an in-lens duo detector which can select secondary and backscattered electrons by changing the retarding voltage on a filtering grid [78]. The spatially resolved electron count is represented as an intensity modulation in a graphic image. The signal strength is strongly dependent on the sample topography. Surfaces facing away from the detector appear darker, while protrusions and sharp edges generate a stronger signal and appear brighter [75].

Samples in this work were analyzed at the Electron Microscopy Centre, University Medicine Rostock, using a Zeiss Merlin VP Compact scanning electron microscope with a typical acceleration voltage of 5kV.

2 X-ray diffraction

XRD allows the qualitative and quantitative detection of crystalline phases of a material, usually with a sensitivity of a few mass percents. The x-ray wavelength is in the same range as the common interatomic distances in a crystal lattice. For this reason, the diffraction of x-rays can be used for structural analysis. For the constructive interference of reflections off two adjacent lattice planes with distance d , the Bragg equation holds [25]:

$$n\lambda = 2d \sin \theta \quad (1)$$

n is the order of the interference maximum, λ the x-ray wavelength, and θ is the incident angle relative to the lattice plane. The intensity distribution of the diffracted radiation is proportional to $|F|^2$, with F being the scattering amplitude and the scattering vector $\vec{Q} = \vec{k}_i - \vec{k}_f$ [79]:

$$F(\vec{Q}) = \sum_n f_n \cdot e^{-i\vec{Q} \cdot \vec{r}_n} \quad (2)$$

It is summed over n lattice points, their positions are described by a linear combination of the basis vectors of the lattice, $\vec{r}_n = n_1\vec{a} + n_2\vec{b} + n_3\vec{c}$. f_n is the atomic structure factor which can be understood as the Fourier transform of the local electron density $n_e(\vec{r})$ [79]:

$$f_n(\vec{Q}) = \int n_e(\vec{r}) e^{i\vec{Q} \cdot \vec{r}} dV.$$

For constructive interference, the scattering amplitude F has to be nonzero [79]:

$$\begin{aligned} F(\vec{Q}) &= f(\vec{Q}) \sum_n e^{-i\vec{Q} \cdot (n_1\vec{a} + n_2\vec{b} + n_3\vec{c})} \\ &= f(\vec{Q}) \left(\sum_n e^{-in_1\vec{Q} \cdot \vec{a}} \right) \left(\sum_n e^{-in_2\vec{Q} \cdot \vec{b}} \right) \left(\sum_n e^{-in_3\vec{Q} \cdot \vec{c}} \right) \\ &\neq 0. \end{aligned}$$

This leads to three equations which have to be fulfilled simultaneously, known as the Laue condition [25]

$$\vec{Q} \cdot \vec{a} = 2\pi h ; \quad \vec{Q} \cdot \vec{b} = 2\pi k ; \quad \vec{Q} \cdot \vec{c} = 2\pi l$$

The Laue condition is solved by a scattering vector $\vec{Q} = h\vec{A} + k\vec{B} + l\vec{C}$, with $\vec{A}, \vec{B}, \vec{C}$ being reciprocal lattice vectors, and h, k, l the Miller indices of a lattice plane. This means that a reflection is possible under the condition that the scattering vector is equal to a reciprocal lattice vector \vec{G} :

$$\vec{Q} = \vec{G}$$

In an experimental scattering setup, a powder sample contains crystallites with statistical orientation. Each lattice plane present in the sample creates a reflection at a characteristic angle according to equation (1). The reflection can be imaged by an area detector, e.g. a CCD detector. The diffraction pattern is a conic section of the diffraction cone with the detector plane. This pattern can be transformed into intensity as a function of the scattering angle 2θ by integration along the diffraction rings.

2.1 Synchrotron radiation

Synchrotron radiation is a broad spectrum of electromagnetic waves emitted by charges travelling in a circle. Inside synchrotrons or storage rings, a beam of electrons or positrons reaches relativistic speed, with kinetic energies in the range of GeV. The radiation pattern differs from that of a classical radiating dipole. The pattern is distorted tangentially to the path of the beam, creating a narrow cone shaped pattern [79]. The power of emitted synchrotron radiation is proportional to

$$P \approx \frac{2e^2c}{R^2} \left(\frac{v}{c} \right)^2 \left(\frac{E_{el}}{mc^2} \right)^4 \propto \frac{\gamma^4}{R^2},$$

where R is the radius of the trajectory, e is the elementary charge, c is the speed of light and E_{el}, v, m are the charged particle's energy, velocity and rest mass, respectively [79]. γ is the reduced energy, $\gamma = E_{el}/mc^2$. Therefore, locally forcing the beam onto a trajectory with a decreased radius will improve brightness. In an undulator, a periodic array of magnets with opposed field directions lets the beam follow an oscillating path

in the shape of opposed circular arc segments [80]. This trajectory is realized with the help of an array of magnets, generating opposed magnetic fields in every bend. The segments are arranged in such a way that the radiation emitted by a charge in one segment is in phase with the radiation from the following segment. Constructive interference between wavelets emitted in each of the periodical bends additionally increases the photon flux. The coherent addition of amplitudes is only applicable to a single wavelength, rendering the emitted radiation quasi-monochromatic. The quality of such a setup is measured by its brilliance. Brilliance is defined as the number of photons received per second and per source area, within 0.1% of the bandwidth [80]:

$$Brilliance = \frac{Photons}{s \cdot mrad^2 \cdot mm^2 \cdot 0.1\% \frac{\Delta E}{E}}$$

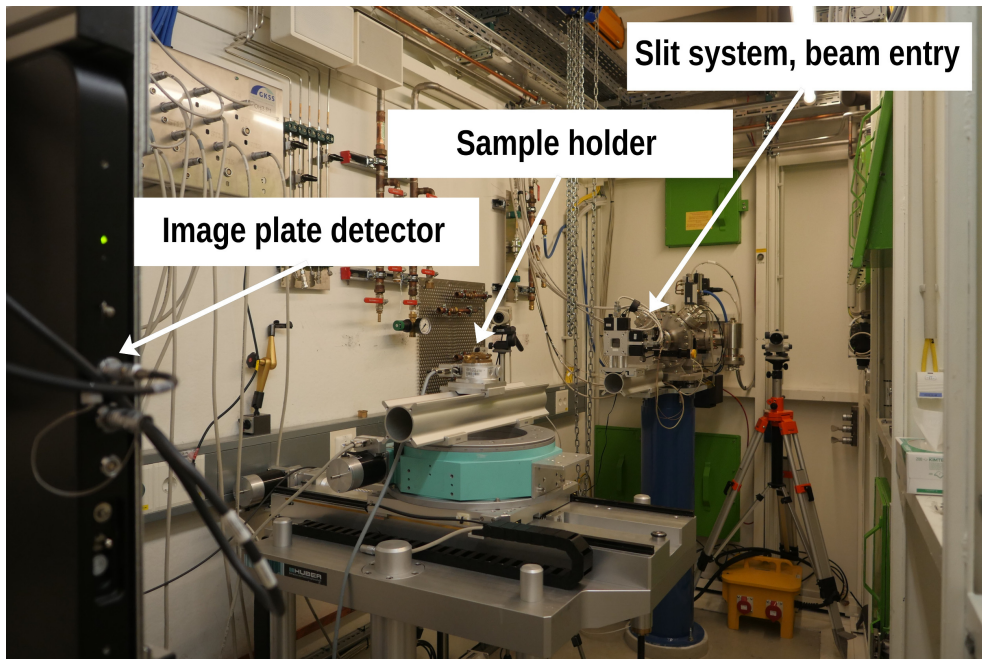


Figure 1: High energy X-ray diffraction setup at High Energy Material Science (HEMS) beamline P07 at the storage ring PETRA III, DESY Germany.

High energy X-ray diffraction experiments were performed at the High Energy Material Science (HEMS) beamline P07 located at the high brilliance synchrotron radiation storage ring PETRA III, DESY Germany (see figure 1). The basic design parameters of the storage ring are an energy of 6 GeV and a current of 100 mA. The source of X-rays for HEMS was a 2 m long standard PETRA undulator. The investigations were performed in the test facility EH1 using an indirectly water-cooled single bounce monochromator with a Si(220) Laue single-crystal leading to monochromatic synchrotron radiation with a wavelength $\lambda = 0.1424 \text{ \AA}$ [81, 82]. The experiments were carried out in Debye-Scherrer geometry with a sample to detector distance of 1183 mm. The diffraction

patterns were collected with a Perkin Elmer image plate detector ensuring fast data acquisition. The patterns were radially integrated over 5° intervals to calculate intensity over scattering angle 2θ .

2.2 Rietveld refinement

X-ray diffractograms can be analysed quantitatively by means of Rietveld refinement. With the help of literature values for the crystal structures that are assumed to be present in the sample, theoretical diffraction patterns can be calculated. This model for a crystal structure can be refined in numerous calculation steps to get as close as possible to the measured diffractogram. For this numerical procedure, the method of least squares is used. The function M is minimized, it depends on the measured intensities I_i^{Exp} and the calculated intensities I_i^{Theo} [83]:

$$M = \sum_i w_i (I_i^{\text{Exp}} - \frac{1}{c} I_i^{\text{Theo}})^2.$$

w_i are the statistical weights, c is a scale factor.

The intensities are calculated from a model that takes into account the chemical and microstructural properties of the phases contained in the sample, as well as the geometry and characteristics of the measuring instrument and sample. An example for such an equation is the following one [84]

$$I_i^{\text{calc}} = \sum_{p=1}^N S_p \sum_{k=1}^M L_k |F_{k,j}|^2 S_j(2\theta_i - 2\theta_{k,j}) P_{k,j} A_j + b_i(2\theta).$$

S_p are the scale factors for each of the N phases. All quantities with the index k are summed over the number of peaks M . L_k is the Lorentz polarization factor, describing the geometry of the measuring setup, $|F_{k,j}|^2$ is the structure factor which is related to the scattering amplitude (eq. (2)). The function S_j takes account for the profile shape, $P_{k,j}$ describes texture, i.e. preferred orientations of the crystallites, A_j is the absorption factor. The background is approximated by a polynomial function $b_i(2\theta)$.

The profile shape function S_j describes line broadening due to both microstrain and crystallite sizes. The line broadening caused by crystallites with a size d is described by the Scherrer equation [85],

$$d = \frac{C \cdot \lambda}{B \cdot \cos(\theta)},$$

where C is a dimensionless shape factor, λ is the X-ray wavelength, B is the peak's FWHM in radians and θ is the Bragg angle.

The quality of the refinement can be assessed with the help of the R_{wp} factor. It is calculated from the square root of the minimized function M , divided by the weighted

intensities for scaling [86]:

$$R_{\text{wp}} = \sqrt{\frac{\sum_{i=1}^N [w_i(I_i^{\text{Exp}} - I_i^{\text{Calc}})]^2}{\sum_{i=1}^N [w_i I_i^{\text{Exp}}]^2}}.$$

The diffractograms were analysed using the MAUD software [87, 88]. For all samples, the fitting procedure was performed assuming the tetragonal crystal structure of maghemite ($\gamma\text{-Fe}_2\text{O}_3$, space group $P4_12_12$) [55] which showed the closest match with the measured patterns.

3 Mössbauer spectroscopy

Mössbauer spectroscopy is used to obtain information both on the chemical environment of atomic nuclei and on its magnetic interactions [29]. It makes use of the recoilless resonant absorption of gamma radiation by nuclei in solids which is referred to as the Mössbauer effect [89]. If a free nucleus emits a gamma quant during its transition between two nuclear energy levels, the energy of the emitted gamma quant is reduced in comparison to the energy difference between these two levels due to nuclear recoil. Analogously, the energy of an incoming gamma quant required for resonant absorption is greater than this energy difference. In the case of a nucleus embedded in a crystal lattice, the recoil energy is transferred as a lattice vibration, a phonon. For recoil energies below the lowest quantized phonon energy, recoilless emission and absorption are possible [90]. The gamma radiation source contains ^{57}Co which decays by electron

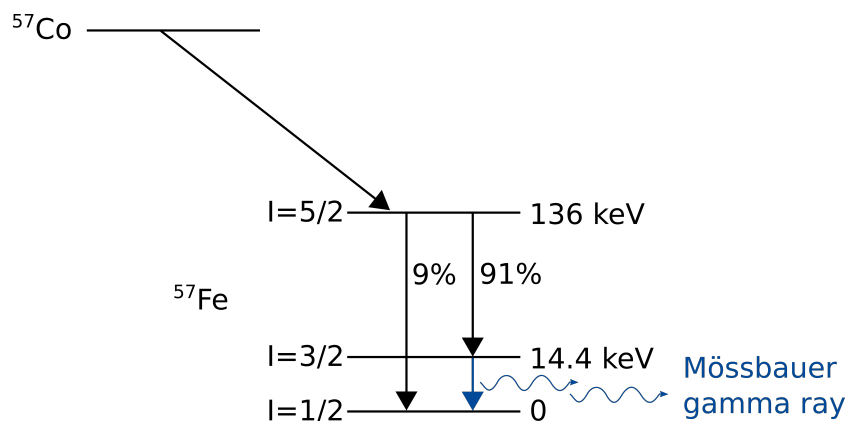


Figure 2: Nuclear decay scheme showing the decay of ^{57}Co to ^{57}Fe . The gamma radiation emitted at 14.4 keV is commonly used for Mössbauer experiments. After [90].

capture to metastable ^{57}Fe . The latter decays by emitting gamma radiation, either in a direct transition to its ground state or in a cascade via the energy level of 14.4 keV which is commonly used for Mössbauer experiments (see figure 2) [90].

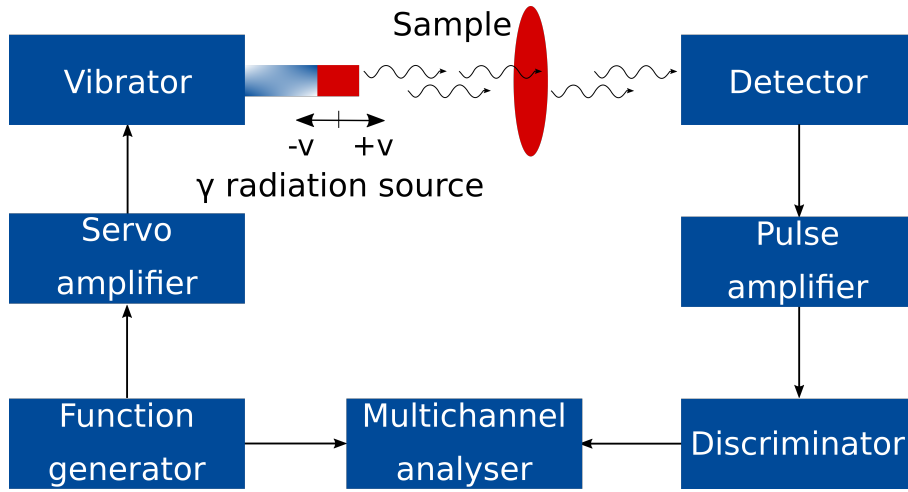


Figure 3: Schematic picture of the setup used to acquire Mössbauer spectra.

The setup for the acquisition of Mössbauer spectra is presented schematically in figure 3. A very fine variation of the radiation's energy is achieved by vibrating the source relative to the sample, making use of the relativistic Doppler effect [91]. The transmission signal of gamma radiation through the sample is detected and amplified while rejecting non-resonant background radiation. Finally, the measured counts are collected in channels corresponding to the respective velocities of the source by a multichannel analyser. The velocity of the source is driven by a function generator, usually providing a speed profile in the shape of a triangle function. Mössbauer spectra are normally plotted featuring a horizontal axis giving the energy difference between the emitted and the absorbed radiation in units of relative velocity between source and sample. The relationship between the gamma photon energy E_γ (in the rest frame of the sample) and the relative velocity v is

$$E_\gamma = E_0 \left(1 + \frac{v}{c} \right),$$

where E_0 is the transition energy of the source (in the rest frame of the source) and c is the speed of light [91].

If emission and absorption were to take place at the exact same energy, the Mössbauer spectrum would only show one peak at zero relative velocity. Real Mössbauer spectra however show a shifting and splitting of spectral lines due to three effects: Isomer shift, quadrupole splitting and magnetic splitting, as shown in figure 4.

Isomer shift is caused by the electric monopole interaction between the nuclear charge distribution and the electronic charge density at the nucleus. The energies of emission and absorption show a small difference, visible in the spectrum as a horizontal offset. This is explained by the different nuclear volume of the excited state of the emitting atom and the ground state of the absorbing atom. Besides this, the electron density changes depending on the material containing the Mössbauer active atoms. Therefore,

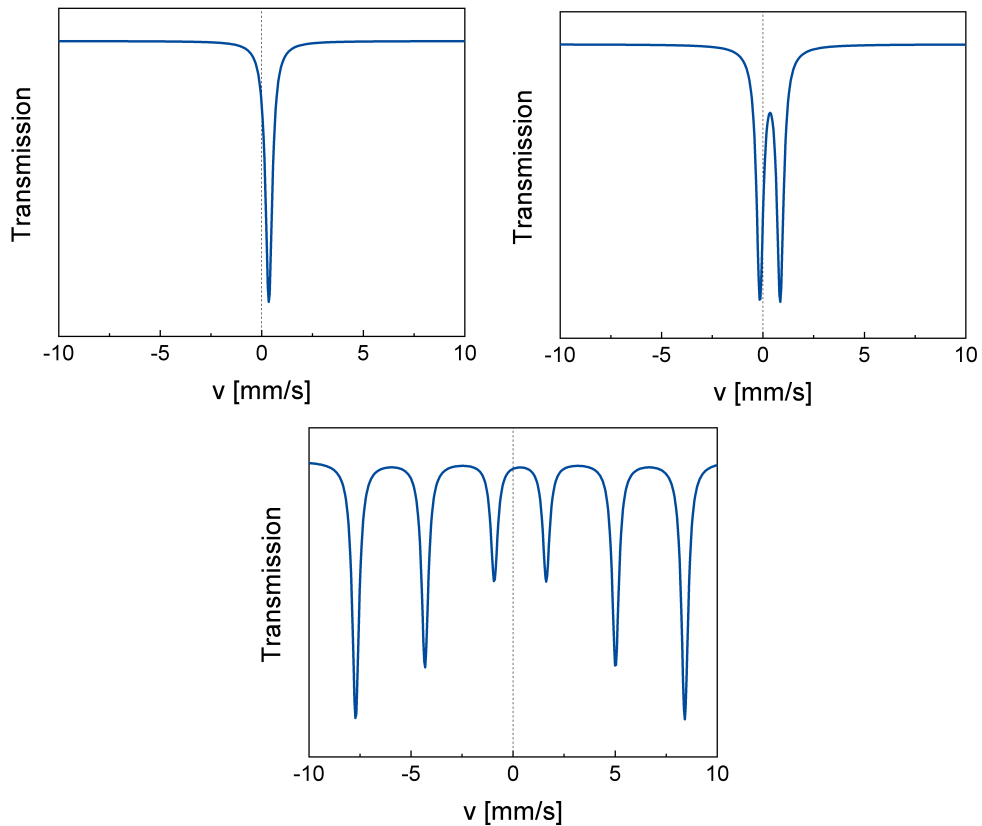


Figure 4: Calculated Mössbauer spectra showing a singlet with energy shift due to isomer splitting (top left), a doublet caused by quadrupole splitting (top right) and a sextet due to magnetic splitting (bottom).

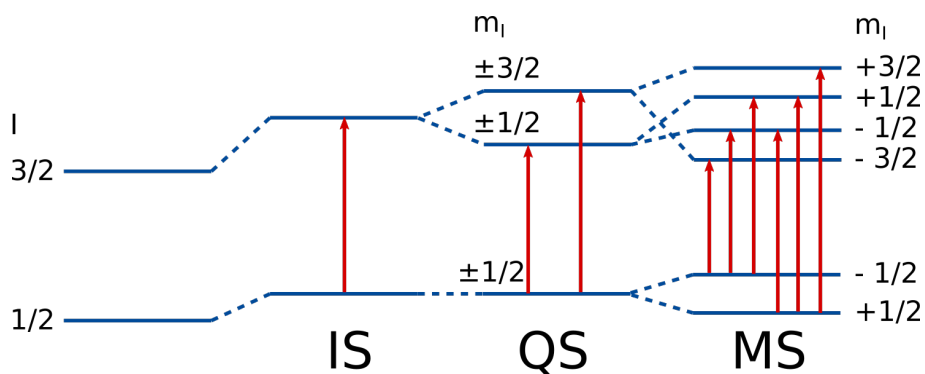


Figure 5: Schematic showing the nuclear levels under the influence of isomer splitting (IS), quadrupole splitting (QS) and magnetic splitting (MS). After [90].

the isomer shift contains information on the oxidation state, spin state and the bonding environment [92]. For example, the isomer shift assumes larger values for divalent iron than for trivalent iron. This is due to the stronger shielding of the nucleus from s-electrons caused by a higher number of d-electrons in divalent iron [91].

Quadrupole splitting results from a non-spherical nuclear charge distribution causing an electric quadrupole moment. This is the case for nuclei with a nuclear angular momentum quantum number $I > \frac{1}{2}$. In the case of ^{57}Fe with $I = \frac{3}{2}$, the excited state splits into two substates characterized by magnetic quantum numbers $m_I = \pm\frac{1}{2}$ and $m_I = \pm\frac{3}{2}$ (see figure 5), resulting in a doublet in the spectrum. The quadrupole moment reflects the symmetry of the bonding environment, containing information on the oxidation state, spin state and site symmetry [92].

Magnetic splitting occurs due to the magnetic dipole interaction between the nuclear magnetic moment and a magnetic field at the nucleus. It is caused by an unpaired spin of the atom's electrons, depending on the oxidation state and spin state of the atom. A state with nuclear angular momentum quantum number $I > 0$ splits into $2I + 1$ substates. For ^{57}Fe , the ground state $I = \frac{1}{2}$ splits into two substates, while the excited state $I = \frac{3}{2}$ splits into four substates [90]. According to the selection rule $\Delta m_I = 0, \pm 1$, six transitions are possible (see figure 5), visible as a sextet in the spectrum. The splitting of spectral lines is proportional to the magnetic hyperfine field experienced by the nucleus, featuring substates with energies E_{I,m_I} :

$$E_{I,m_I} = -\frac{m_I}{I}\mu B,$$

with μ being the nuclear magnetic moment and $B = \mu_0 H_{\text{hf}}$ being the magnetic hyperfine field [93]. The magnetic hyperfine field experienced by the nucleus is a superposition of an internal field induced by the magnetic moments of valence electrons and an external field which is applied externally or which is due to the magnetization of the surrounding material [94]. This leads to the phenomenological description of the average magnetic hyperfine field at a specific iron site \bar{H}_{Fe} as a function of the material's magnetic moment [95],

$$\bar{H}_{\text{Fe}} = a\bar{\mu}_{\text{Fe}} + b\bar{\mu},$$

where $\bar{\mu}_{\text{Fe}}$ is the average magnetic moment of the iron atom at that site, a and b are proportionality constants, and $\bar{\mu}$ is the average magnetic moment of the alloy or chemical compound or the magnetic moment inside a particle.

The spectral intensity distribution of a line in the Mössbauer spectrum is described by a Lorentz distribution [91],

$$I(E) = \frac{I_0 \left(\frac{\Gamma_n}{2}\right)^2}{(E - E_0)^2 + \left(\frac{\Gamma_n}{2}\right)^2},$$

where I_0 is the maximum intensity at transition energy E_0 , Γ_n is the natural line width with $\Gamma_n = \frac{\hbar}{\tau}$, τ being the mean lifetime of the radiating state.

Given the splitting of spectral lines into doublets and sextets, the spectrum can be fitted assuming a superposition of Lorentz profiles. For the analysis of $\gamma\text{-Fe}_2\text{O}_3$ with space group $\text{P}4_12_12$, a superposition of two sextets can be assumed [96]. One sextet refers to Fe^{3+} ions in tetrahedral sites (A-sites) and the other one to Fe^{3+} ions in octa-

hedral sites (B-sites). For bulk maghemite, these two sextets have similar values for their hyperfine interaction parameters and appear as a single sextet. In the case of nanoparticulate maghemite, contributions of surface atoms are no longer neglectable, as the volume of surface layers makes up for a significant proportion of the total particle volume [97]. These surface atoms have a different local environment compared with atoms in the inner region because they lack neighbours at least in one direction. Contributions of Fe^{3+} ions located at A- and B-sites within the surface region are responsible for the appearance of additional sextets in the spectrum, and these can be identified by their smaller magnetic hyperfine splitting compared with contributions from the inner region [97]. The fitting model used in this work is therefore a superposition of four sextets, as shown in figure 6. Contributions of surface atoms will be referred to as sites A_s and sites B_s . Sextets with hyperfine parameters close to bulk values are assigned to the inner region of nanoparticles. The bulk contributions of Fe^{3+} ions at the A- and B-sites will be referred to as sites A_b and sites B_b .

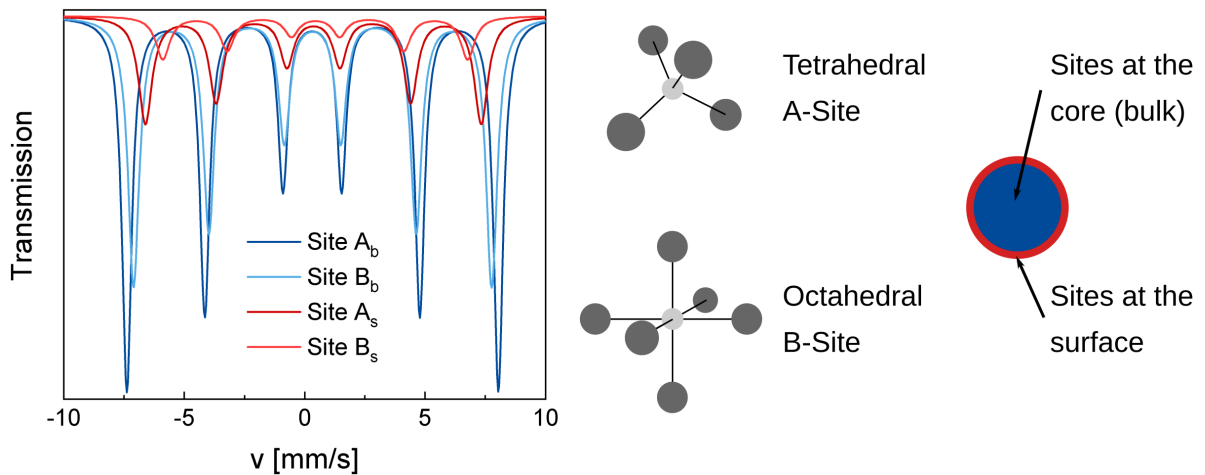


Figure 6: The fitting model used in this work is a superposition of four sextets (plot on the left), containing contributions of iron atoms at tetrahedral sites (A-sites) and octahedral sites (B-sites), located at the core and surface region of a particle, as shown schematically.

The ^{57}Fe Mössbauer spectroscopy studies were performed in transmission geometry at room temperature. The γ -ray source was 25 mCi ^{57}Co embedded in a Rh-matrix, mounted on a FAST Comtec Mössbauer drive unit working in constant acceleration mode. Mössbauer transmission spectra were collected with a scintillation counter in a velocity range $\pm 11\text{mm/s}$ with 1024 channels before folding. A standard α -Fe foil was used for calibration and the isomer shift is given with respect to iron at room temperature. The Mössbauer spectra were analysed with the software RECOIL [98], assuming a superposition of Lorentz distribution shaped peaks.

4 AC susceptometry

AC susceptometry is a dynamic method for the characterization of magnetic properties of a material. It is possible to perform measurements on both solid bulk materials and magnetic particles in suspension. Besides the frequency dependent measurement of magnetic susceptibilities, it is possible to determine parameters such as relaxation times, magnetic core diameters and hydrodynamic diameters [99, 100].

A schematic picture of the measuring setup used for dynamic susceptibility measurements is shown in figure 7. It consists of three cylindrical, coaxial coils. One coil is used to generate an alternating electromagnetic field which is detected by the other two coils. The sample is placed within one of the detection coils, while the other one remains empty, generating a reference signal [101, 102]. The differential signal between the two detection coils is amplified and allows the determination of the real and imaginary part of the dynamic susceptibility [103, 104].

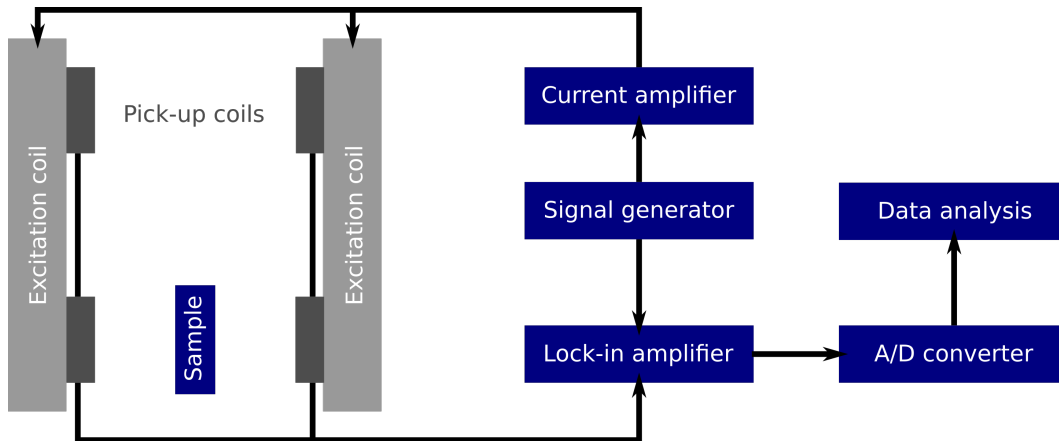


Figure 7: Schematic picture of the excitation and detection coil system, the attached electronics and data acquisition (after [102]).

The magnetic susceptibility χ is defined as the slope of the magnetization curve, being the partial derivative of the magnetization M with respect to the driving field amplitude H [25]:

$$\chi = \frac{\partial M}{\partial H}.$$

Magnetic susceptibility is a frequency dependent, complex quantity,

$$\chi(\omega) = \chi'(\omega) - i\chi''(\omega),$$

where, according to the Debye model [105],

$$\chi'(\omega) = \frac{\chi_0}{1 + (\omega\tau)^2} \quad \text{and} \quad \chi''(\omega) = \frac{\chi_0\omega\tau}{1 + (\omega\tau)^2}.$$

ω is the angular frequency, τ is the relaxation time and χ_0 is the initial static susceptibility. A plot of the resulting real and imaginary parts of the susceptibility curve is shown in figure 8.

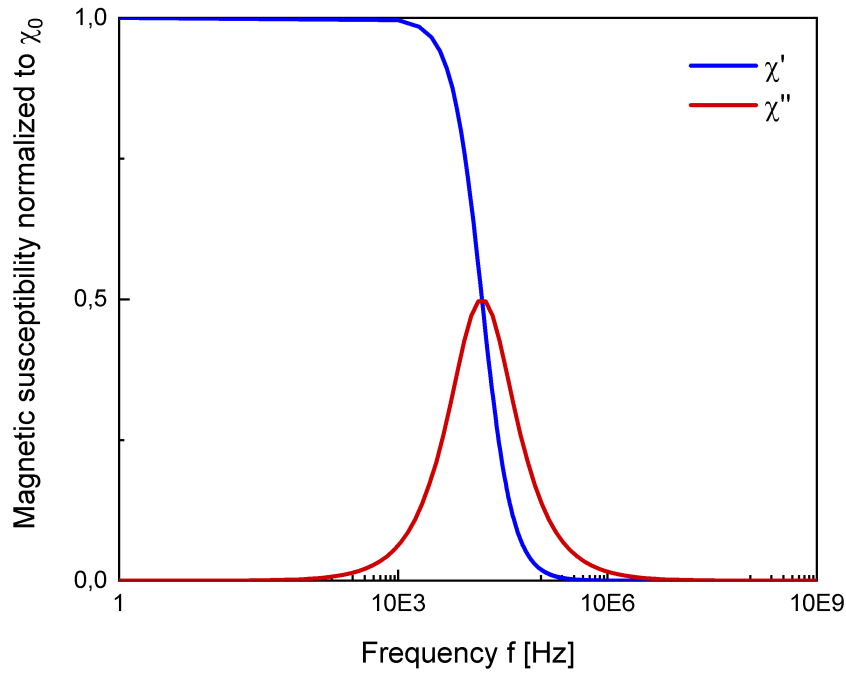


Figure 8: The real part χ' and the imaginary part χ'' of the magnetic susceptibility according to the Debye model are plotted for a relaxation time $\tau = 1\mu\text{s}$. The angular frequency is replaced using $\omega = 2\pi f$.

Particles in a suspension can relax out of a magnetized state by randomly rotating out of the magnetization direction due to Brownian motion. This effect is called Brownian relaxation and is described by the relaxation time t_B [31, 32]:

$$\tau_B = \frac{4\pi r_H^3 \eta}{k_B T},$$

where r_H is the hydrodynamic radius of a particle, η is the viscosity of the liquid phase, k_B is the Boltzmann constant and T the temperature.

Neel relaxation, on the other hand, describes the internal flipping of the magnetic moment around the magnetic easy axis of the particle [30, 106]. The Néel relaxation time τ_N is given by the magnetic anisotropy of the single-domain crystals K , their magnetic core volume V_c , the Boltzmann constant k_B , Temperature T and the characteristic

relaxation time τ_0 :

$$\tau_N = \tau_0 \cdot e^{\frac{KV_C}{k_B T}}.$$

An effective relaxation time τ_{eff} is introduced to account for contributions by both Néel and Brownian relaxation [106, 32],

$$\tau_{\text{eff}} = \frac{\tau_B \tau_N}{\tau_B + \tau_N}.$$

For the analysis of AC susceptibility measurements performed on single-core magnetic particles, i.e. particles containing one single domain crystal, the following model is used [101, 107]:

$$\chi(\omega) = C \int \frac{r_C^6}{1 + i\omega\tau_{\text{eff}}(r_C, \delta)} f(r_C) dr_C + \chi_\infty$$

Here, C is a constant including contributions of the temperature, particle number density and intrinsic particle magnetization, $f(r_C)$ is the distribution of magnetic core sizes r_C and δ is the thickness of the hydrodynamic surface layer, where $\delta = r_H - r_C$. AC susceptibility spectra of magnetic nanoparticle superstructures containing multiple crystallites are analysed with an extended multicore model [107]. The Debye model for the susceptibility of particles with a distribution $f(r_H)$ of hydrodynamic diameters r_H is used to describe particles undergoing Brownian relaxation. The contribution of particles undergoing Néel relaxation is added separately using a Cole-Cole expression, where the distribution of relaxation times is defined by the parameter α which can assume values between 0 and 1:

$$\chi(\omega) = \chi_{0B} \int \frac{1}{1 + i\omega\tau_B(r_H)} f(r_H) dr_H + \frac{\chi_{0N}}{1 + (i\omega\tau_N)^\alpha} + \chi_\infty.$$

χ_{0B} and χ_{0N} are the contributions of Brownian and Néel relaxation to the initial static susceptibility.

Dynamic susceptibility measurements were performed by micromod Partikeltechnologie GmbH, Warnemünde, using a DynoMag AC susceptometer over a frequency range from 6 Hz to 250 kHz. Sample suspensions were diluted to reach an iron concentration of 1 mg/ml. Frequency dependent susceptibility curves were fitted with the help of an extended multi-core model.

5 Atomic force microscopy

In atomic force microscopy (AFM), a sharp probe tip is used to scan a sample surface while measuring the force of local interactions between the tip and the sample on an atomic to nanometer scale [108]. These interactions include several types of

electromagnetic interactions. Besides the acquisition of a topographic image, there are more specialized applications such as magnetic force microscopy measuring the local magnetization, Kelvin probe force microscopy measuring the local work function, or a mapping of mechanic properties [109]. A great advantage of AFM is that it is applicable to all kinds of materials regardless of their electromagnetic, mechanical or crystallographic properties.

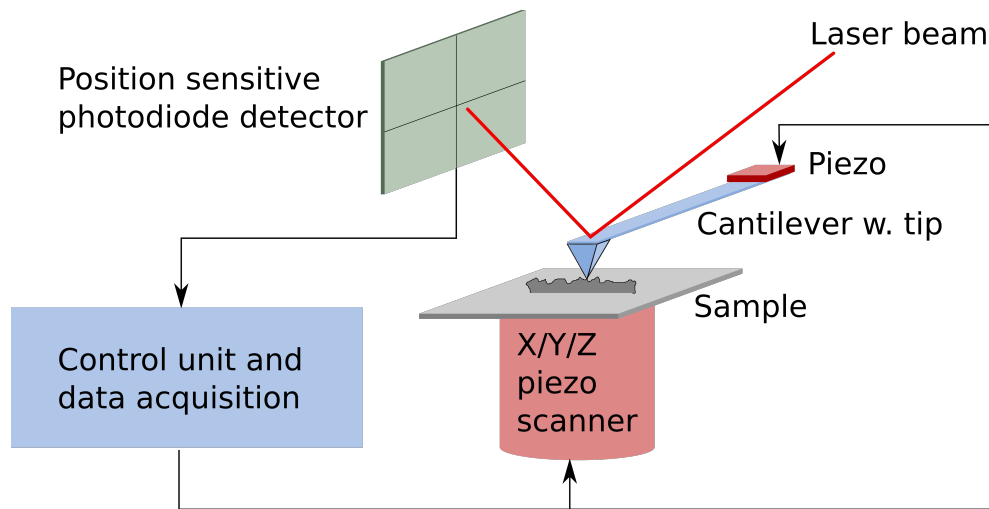


Figure 9: Schematic picture of an atomic force microscope, after [110].

Samples for investigation by AFM are placed on a three-axis piezo scanner which is able to actuate the sample in the x-y plane performing a linewise scan (see figure 9). A fine tip with a curvature radius of a few nanometers is brought into close proximity of the sample's surface [110]. The tip is attached to a cantilever which is typically of a micrometer dimension. The interaction between the tip and the sample causes the cantilever to bend, this can be detected by measuring the deflection of a laser beam that is reflected off the back of the cantilever. The deflection of the laser beam is measured with the help of a position sensitive photodiode detector. The signal is sent to the control and data acquisition unit which can work in several modes of operation. It is possible to either move the tip at a line of constant force using a feedback loop that controls the z coordinate of the piezo scanner - in this case, the z coordinate is used to build an image - or to move the sample at a constant height while measuring the changing force acting on the cantilever. The AFM can be operated in static and dynamic modes [110]. In static modes, the force acting on the tip causes the cantilever to bend according to its spring constant. In dynamic modes, the cantilever is excited by a piezo crystal at an oscillation frequency near its resonance and the dynamic behaviour is measured. Another parameter for distinguishing modes of operation is contact or non-contact with the sample surface. For dynamic measurements, the tip may also be in temporary contact. In this work, tapping mode (semi-contact mode) is used. Here, the cantilever amplitude is kept constant, while the z coordinate and the phase

shift between the cantilever oscillation and the driving signal are variable [110]. The advantage of this mode is the reduction of lateral forces acting on the tip and cantilever, reducing the risk of damage while maintaining a resolution similar to that in contact mode [110]. The tip's oscillation amplitude, resonance frequency and phase shift are directly linked to the tip-sample interactions [111]. For a discussion of tip-sample interactions, one needs to distinguish between attractive and repulsive interaction, as well as between long-range and short-range interactions. The Lennard-Jones potential $U(r)$ (see figure 10) is frequently used as a model for the superposition of attractive and repulsive interactions between the tip and the sample [109]:

$$U(r) = 4U_0 \left[\left(\frac{R_a}{r} \right)^{12} - \left(\frac{R_a}{r} \right)^6 \right].$$

r is the distance between the tip and the sample, U_0 describes the depth of the potential well and R_a is the distance of zero potential. It is visible that for larger tip-sample distances, attractive interactions are dominant, while repulsive interactions dominate the shorter distances. The two regimes are separated by the potential minimum.

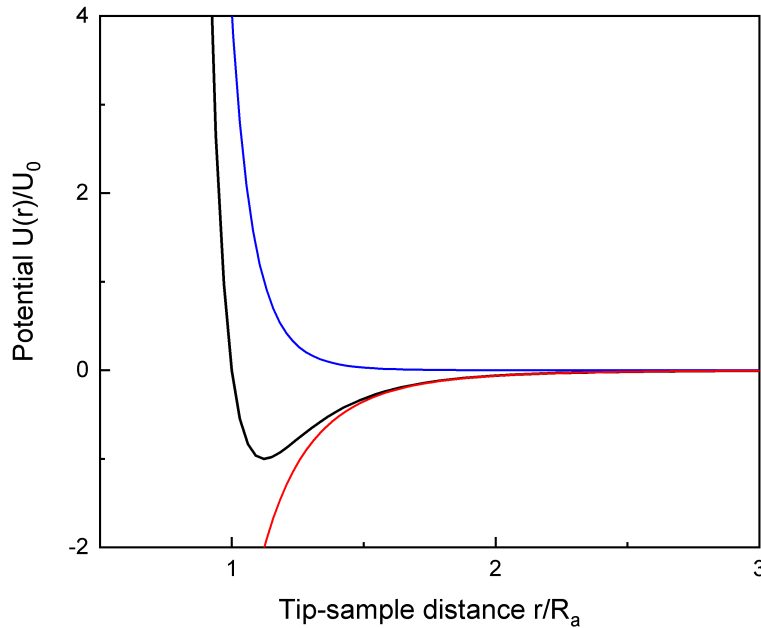


Figure 10: The Lennard-Jones potential is a model for tip-sample interactions (black line). It contains both attractive (blue line) and repulsive (red line) contributions.

In the long-range regime, i.e. for distances larger than 1 nm, attractive van der Waals interactions play the dominant role [109]. They are caused by spontaneous charge fluctuations of atoms or molecules without a permanent dipole moment. In the short-range regime, i.e. at less than 1 nm distance, chemical bonds are one major type of interaction. They are caused by an overlap of wave functions of valence electrons and

can be repulsive or attractive. Besides these, when bringing the atoms of the tip and the sample even closer, strong repulsive forces come into play. They are caused by both the ionic repulsion due to an overlap of inner electron shells, as well as by the Pauli repulsion due to the quantum mechanic Pauli exclusion principle [109].

The AFM's precision and imaging accuracy are limited by thermal drift, feedback overshoot, piezo creep and electrical noise, but the main source of artefacts is the tip geometry, since image acquisition always produces a convolution of the sample topography and the tip [109]. Generally speaking, topographic features with a curvature radius smaller than the tip's will be imaged with strong artefacts [109]. An accurate tracking of features on the sample surface can be expected for features with a radius greater than twice the tip curvature radius [112]. This limitation needs to be considered when characterizing thin films. An important parameter in the characterization of thin films is roughness [113]. It has been shown that vertical roughness measurements are relatively insensitive towards errors caused by the finite tip radius [114]. The roughness of a surface area is described by the root mean square roughness [113, 114],

$$R_{\text{rms}} = \sqrt{\frac{1}{n} \sum_{i=1}^n (y_i - \bar{y})^2},$$

with y_i being the data points of a height profile, n being the number of data points and \bar{y} being the mean height of the surface.

Measurements were carried out using an NT-MDT SOLVER scanning probe microscope with an NT-MDT NSG01 AFM probe with gold coating and a tip curvature radius of nominally 10 nm. Semicontact topography scans were conducted at a line frequency of 0.2 Hz with feedback gain set to 1.0. Data processing, visualization and analysis were performed using Gwyddion software [115].

Results

1 Synthesis and optimization of magnetic nanoflowers

Magnetic iron oxide nanoparticles were synthesized using a polyol route [62, 41, 40, 50]. Iron(II) and iron(III) chlorides were used as precursors at variable stoichiometric ratios, in a 1:1(wt./wt.) solvent mixture of N-methyldiethanolamine (NMDEA) and diethylene glycol (DEG). The molar fraction of iron(III) ions contained in the initial precursor solution is characterized by the stoichiometric parameter ζ , which is defined as follows [116]:

$$\zeta = \frac{[\text{Fe}^{3+}]}{[\text{Fe}^{3+}] + [\text{Fe}^{2+}]}$$

An alkaline environment was provided by adding 0.8 wt.-% NaOH. The precursor solution was heated from room temperature to target temperature at 2 K/min under vigorous stirring in a flask equipped with a reflux condenser. Two different target temperatures, namely 180°C and 220°C, were held constant for 2 h or 12 h, as listed in tables 1 and 2. The mixture was left to cool down to room temperature under stirring. Two series of samples were produced with individual subsequent treatments.

Investigation of synthesis parameters

Following the procedure described above, three samples A, B and C with $\zeta = 0.67$ were prepared with target temperatures and holding times listed in table 1. The precursor solution for sample A was heated up to 180°C and kept at this temperature for 2 h. The small quantity of sediment was separated magnetically, washed with ethanol and prepared for characterization by transmission electron microscopy. Sample B was prepared at a target temperature of 180°C but with a significantly longer holding time of 12 h to increase the yield. Sample C was prepared at a target temperature of 220°C and a holding time of 2 h. After synthesis the precipitates of samples B and C were separated with the help of a magnet and washed three times with a 1:1 (v/v) mixture of ethanol and acetic acid ethyl ester, once with 10% nitric acid and twice in acetone to remove both organic and inorganic residues, including iron hydroxide byproducts. Finally, the sediments were dispersed in pure water to obtain stable suspensions.

| Sample | A | B | C |
|------------|------|------|------|
| ζ | 0.67 | 0.67 | 0.67 |
| T_t [°C] | 180 | 180 | 220 |
| t_h [h] | 2 | 12 | 2 |

Table 1: Synthesis parameters for samples A,B and C. The stoichiometric parameter ζ , target temperature T_t , and holding time t_h .

Variation of the precursor stoichiometry

A series of samples was prepared varying the precursor stoichiometry as shown as in table 2 to investigate the influence of the stoichiometric parameter ζ . A target temperature of 220°C and a holding time of 2 h were chosen. After the thermal treatment the precursor solutions were left to cool down to room temperature. Next, the sediment was separated magnetically and washed three times with a 1:1 (v/v) mixture of ethanol and acetic acid ethyl ester and once with 10% nitric acid. In contrast to previous experiments, the sediments obtained were added to a 30% iron(III)nitrate nonahydrate solution and kept at 80°C for 45 min under manual stirring to ensure complete oxidation. After cooling to room temperature, washing in 10% nitric acid once and twice in acetone, the sediment was dispersed in pure water.

| ζ | 1.0 | 0.67 | 0.4 | 0.0 |
|------------|-----|------|-----|-----|
| T_t [°C] | 220 | 220 | 220 | 220 |
| t_h [h] | 2 | 2 | 2 | 2 |

Table 2: Synthesis parameters for samples with variable ζ . Target temperature T_t , and holding time t_h .

1.1 Investigation of synthesis parameters

TEM images and the corresponding particle size distributions of samples A, B and C are shown in figure 1. After heating to a target temperature of 180°C and holding this temperature for 2 h, globular primary particles with an average diameter (5.1 ± 1.2) nm are obtained (sample A). They show strong agglomeration after washing. Nevertheless, the formation of nanoflowers is possible at this temperature after longer reaction time with an average diameter of (21.1 ± 1.2) nm as can be seen in figure 1 (sample B). Sample C also yields nanoflowers, with a smaller average size of (14.3 ± 1.2) nm. Furthermore, few non-aggregated primary particles can also be observed in samples B

and C leading to a broader particle size distribution. Sample B shows a broader particle size distribution than sample C.

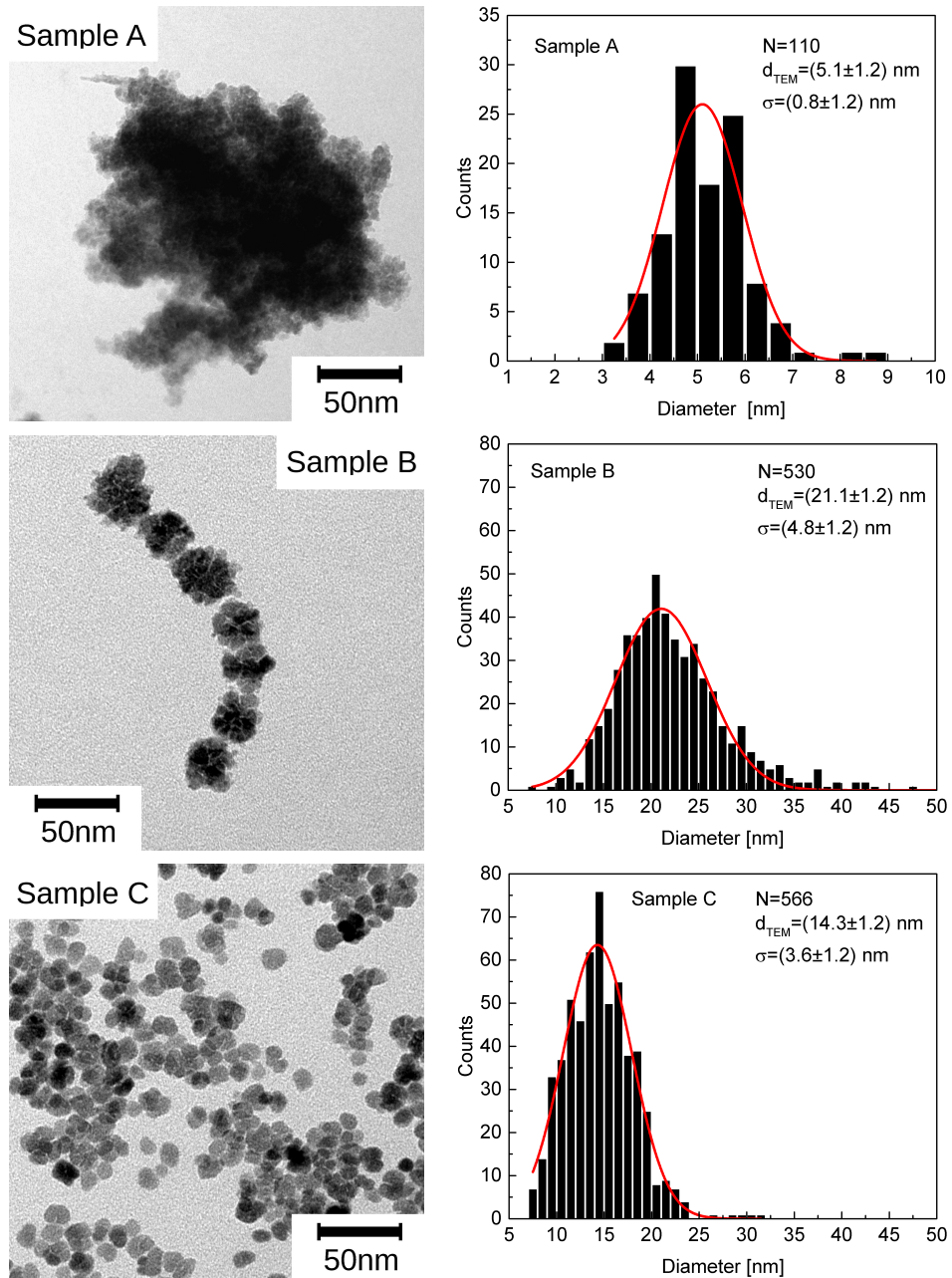


Figure 1: Exemplary TEM images for samples prepared at different target temperatures and holding times and their corresponding particle size distributions. N is the number of evaluated particles, d_{TEM} is the mean value and σ is the standard deviation of the normal distribution.

High energy X-ray diffractograms were taken for samples B and C (Figure 2). The best agreement was found with the tetragonal phase of maghemite for all samples. Lattice parameters a and c (Table 3) were found to deviate from reported values by less than 0.5 % [55, 54]. Both samples have a crystallite size of 14.9 nm despite the different synthesis conditions and particle sizes.

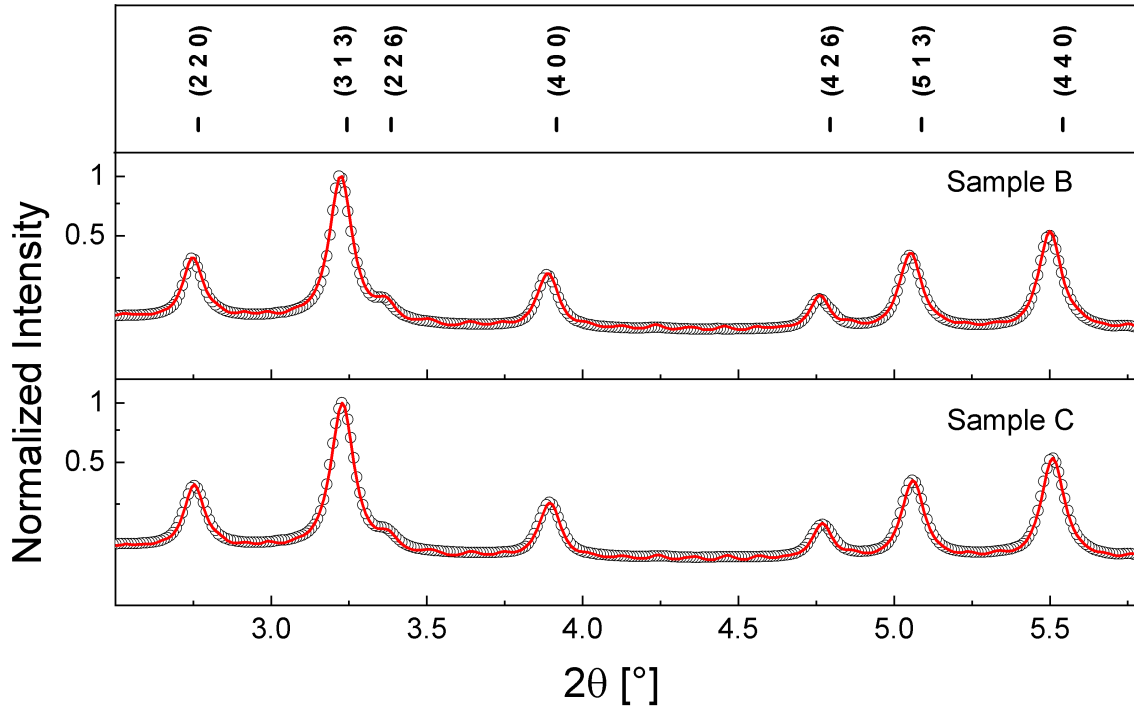


Figure 2: High energy X-ray diffractograms for samples B and C. Circles represent measured intensities, the solid line shows the refined intensity. Bragg reflexes of maghemite with space group $P4_12_12$ are marked and indexed.

Mössbauer spectra for sample B and C were fitted assuming four sextets each (Figure 3). For sample B, magnetic hyperfine fields $\mu_0 H_{\text{hf}} = (47.24 \pm 0.04)$ T and (45 ± 0.07) T were found at A_b - and B_b -sites, respectively. Two additional sextets corresponding to A_s - and B_s -sites can be distinguished with the magnetic hyperfine fields (41.89 ± 0.09) T and (38.13 ± 0.13) T. These values are smaller compared to the magnetic hyperfine fields of bulk maghemite being 50.5 T and 50.0 T [96]. This is caused by fluctuations of the particles' magnetization vector that occur in nanocrystallites [116]. Isomer shifts of the respective sextets are within the reported interval from $(0.32 \pm 0.01) \frac{\text{mm}}{\text{s}}$ to $(0.45 \pm 0.08) \frac{\text{mm}}{\text{s}}$ [97] being characteristic of nanocrystalline maghemite. Quadrupole splitting is zero within the margin of error for all samples and sextets. The spectrum of sample C contains a doublet contribution which can be assigned to particles in the superparamagnetic state [97].

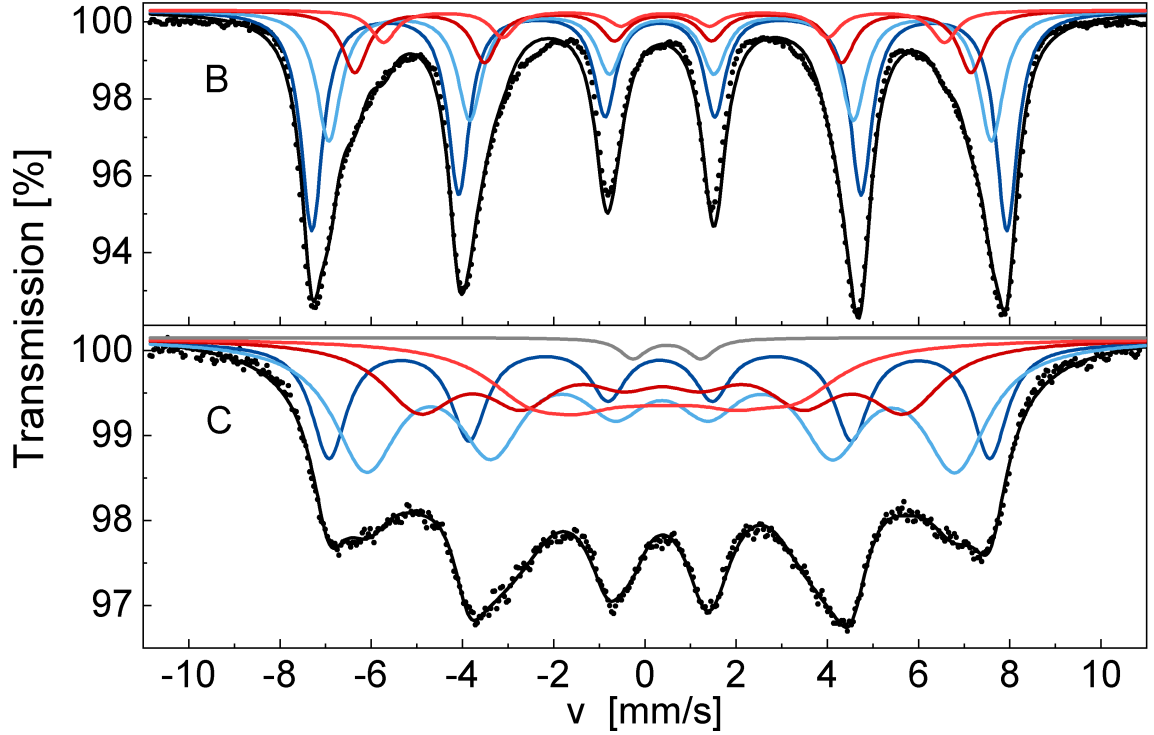


Figure 3: ^{57}Fe transmission Mössbauer spectra of samples B and C. Measured data (dots), fit (black line), A_b contribution (dark red line), B_b contribution (red line), A_s contribution (dark blue line), B_s contribution (light blue line), contribution from particles in the superparamagnetic state (grey line).

| Sample | a [Å] | c [Å] | d_{XRD} [nm] | d_{TEM} [nm] |
|--------|-------------------|--------------------|-----------------------|-----------------------|
| A | - | - | - | 5.1 ± 1.9 |
| B | 8.383 ± 0.001 | 25.265 ± 0.005 | 14.9 ± 0.6 | 21.1 ± 1.2 |
| C | 8.370 ± 0.001 | 25.225 ± 0.004 | 14.9 ± 0.5 | 14.3 ± 1.2 |

Table 3: Maghemite crystal lattice parameters a and c and crystallite sizes d_{XRD} for samples A, B and C obtained by Rietveld refinement, average particle sizes d_{TEM} measured on TEM images.

1.2 Variation of the precursor stoichiometry

Superstructures with nanoflower morphology can be identified on the TEM images of all samples with varying ζ (see figure 5). Boundaries between primary particles are visible. A small fraction of the primary particles is not aggregated. The average particle diameter d_{TEM} increases with ζ , as shown in table 5. It rises from (18.4 ± 1.2) nm for $\zeta = 0$ to (28.7 ± 1.2) nm for $\zeta = 1$. The narrowest size distribution is found at $\zeta = 0$, while it is widest at $\zeta = 0.67$. However, the discrepancies in the width of the size

distributions are insignificant. Nevertheless, Sample $\zeta = 0.67$ differs considerably from the Gaussian profile shape that was assumed for all samples. Possibly, this deviation is due to a non-monomodal distribution of particle sizes.

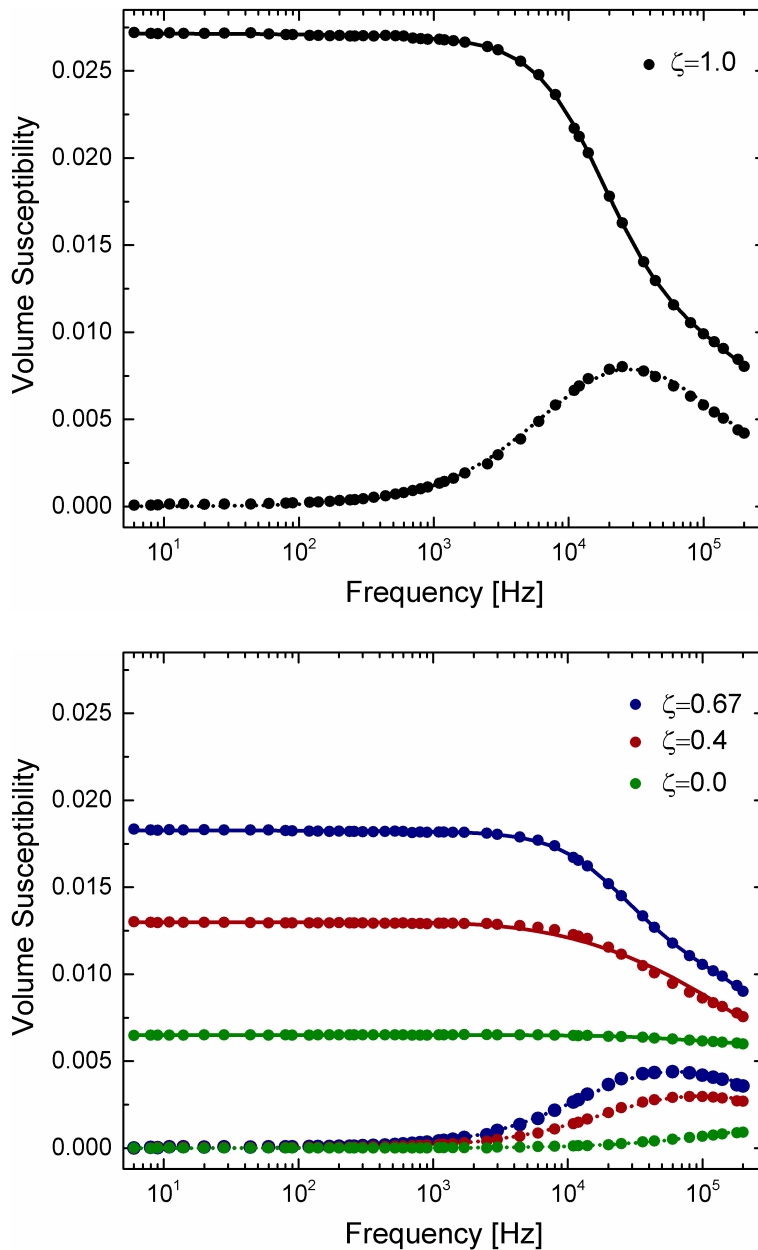


Figure 4: Susceptibility in dependence of frequency for samples prepared varying ζ . Experimental data - measured for samples $\zeta=1.0$ (black dots), 0.67 (blue dots), 0.4 (red dots), 0.0 (green dots). Fit of the real (continuous line) and imaginary part (dashed line) of the dynamic magnetic susceptibility.

Frequency dependent magnetic susceptibility measurements of samples with variable ζ are shown in figure 4. The respective magnetic core sizes d_{ACS} , median Brown relaxation times $\tau_{\text{B}}^{\text{Median}}$, peak frequencies of the imaginary part of the susceptibility f_{max} and the initial static magnetic susceptibility χ_0 are given in table 4. In order to determine the mass magnetic susceptibility with respect to the iron content, colorimetric method was used to determine the iron concentration. Since all samples contain one chemical species exclusively the iron concentrations c_{Fe} also reveal an increase in synthesis yield with decreasing ζ .

Both the real and imaginary part of the susceptibility show an increasing amplitude. This is visible in the low frequency regime of the real part, where static susceptibility is approached and in the peak height of the imaginary part of the susceptibility. Furthermore, a shift in the peak frequency of the imaginary susceptibility towards lower frequencies with increasing ζ can be observed. The decreasing resonance frequency is connected with longer Brownian relaxation times and can be understood as a result of an increasing particle size [52]. Both observations are caused by the increasing magnetic moments and the particle moments. The magnetic core diameters d_{ACS} follow the general trend of growing particle sizes with rising ζ . However, the magnetic core diameter is significantly smaller than particle sizes for $\zeta=0$. The conclusion that these particles contain more than one magnetic core has to be regarded with caution. The peak of the imaginary part of the susceptibility lies outside of the measured frequency regime, which makes the fitting parameters rather uncertain. For all other samples the magnetic core diameters are equivalent to the average nanoflower sizes. This reveals cooperative magnetic behaviour among the primary particles within nanoflowers being characteristic of superferrimagnetism [42].

| ζ | d_{ACS} [nm] | $\tau_{\text{B}}^{\text{Median}}$ [μs] | f_{max} [kHz] | χ_0 | c_{Fe} [$\frac{\text{mg}}{\text{ml}}$] |
|---------|-----------------------|---|------------------------|-----------------------|---|
| 1.0 | 27.9 | 9.04 | 19.5 | 0.0275 ± 0.0003 | 9.24 |
| 0.67 | 24.3 | 8.16 | 29.03 | 0.01861 ± 0.00016 | 13.76 |
| 0.4 | 21.8 | 3.92 | 40.6 | 0.01318 ± 0.00006 | 13.17 |
| 0 | 7.9 | 0.19 | 842 | 0.00615 ± 0.00004 | 15.66 |

Table 4: Magnetic core diameters d_{ACS} , median Brown relaxation times $\tau_{\text{B}}^{\text{Median}}$, peak frequencies f_{max} of the imaginary part of the susceptibility and the static magnetic susceptibility χ_0 , as obtained from fitting the dynamic susceptibility to an extended multi-core model. The iron concentration c_{Fe} was determined using colorimetric method.

In the low frequency regime, volume magnetic susceptibilities approach values ranging from $\chi_0=0.0275$ to $\chi_0=0.00615$, respectively (see figure 4). The magnetic moment μ of a particle can be calculated from the initial static magnetic susceptibility χ_0 using

the following equation [107, 34, 35]:

$$\chi_0 = \frac{\mu_0 n \mu^2}{3k_B T} \Rightarrow \mu = \sqrt{\frac{\chi_0 3k_B T}{\mu_0 n}}.$$

μ_0 is the magnetic constant, n is the number of particles per unit volume, k_B the Boltzmann constant and T is the temperature. To calculate n , which is the number of particles N per unit volume V , one can insert the ratio between the mass of all particles per unit volume m_{sample} and the mass of a single particle m_P . This leads to an expression containing the particle concentration inside the sample $c_{\text{Sample}}[\text{Particles}]$. The mass of a single particle can be expressed by its volume V_P and density $\rho_{\text{Fe}_2\text{O}_3}$.

$$n = \frac{N}{V} = \frac{m_{\text{sample}}/m_P}{V} = \frac{c_{\text{Sample}}[\text{Particles}]}{m_P} = \frac{c_{\text{Sample}}[\text{Particles}]}{\rho_{\text{Fe}_2\text{O}_3} V_P}$$

All samples were diluted to reach an iron concentration $c_{\text{Sample}}[\text{Fe}]$ of 1 mg/ml. Therefore, the particle concentration $c_{\text{Sample}}[\text{Particles}]$ is the product of the iron concentration $c_{\text{Sample}}[\text{Fe}]$ and the dilution factor $c_0[\text{Particles}]/c_0[\text{Fe}]$, which is determined from the as-prepared suspension. The particle volume is approximated by the volume of a sphere with diameter d_{TEM} , as measured on TEM images (Figure 5).

$$n = \frac{c_{\text{Sample}}[\text{Fe}] \cdot c_0[\text{Particles}]}{c_0[\text{Fe}] \cdot \rho_{\text{Fe}_2\text{O}_3} \cdot \pi/6 \cdot d_{\text{TEM}}^3}$$

The density of maghemite is $\rho_{\text{Fe}_2\text{O}_3} = 4.87 \text{ g/cm}^3$ [29]. Using all equations and values mentioned, magnetic moments ranging from $\mu_{\zeta=0} = (0.8 \pm 0.1) \text{ A} \cdot \text{nm}^2$ to $\mu_{\zeta=1} = (3.7 \pm 0.5) \text{ A} \cdot \text{nm}^2$ are obtained (Table 5).

| ζ | d_{TEM} [nm] | $c_0[\text{Fe}]$ [mg/ml] | $c_0[\text{Particles}]$ [mg/ml] | χ_0 | n [$10^{13}/\text{mL}$] | μ [$\text{A} \cdot \text{nm}^2$] |
|---------|--------------------------|-----------------------------|------------------------------------|-----------------|--------------------------------|---|
| 0.0 | 18.4±1.2 | 15.66 | 24.0 | 0.00615±0.00004 | 13±4 | 0.8±0.1 |
| 0.4 | 21.9±1.3 | 13.17 | 19 | 0.01318±0.00006 | 7.2±1.7 | 1.55±0.19 |
| 0.67 | 24.1±1.5 | 13.76 | 19 | 0.01861±0.00016 | 5.2±1.3 | 2.2±0.3 |
| 1.0 | 28.7±1.2 | 9.24 | 11.0 | 0.0275±0.0003 | 2.7±0.6 | 3.7±0.5 |

Table 5: Stoichiometric parameter ζ , particle diameter d_{TEM} , iron concentration after synthesis $c_0[\text{Fe}]$, particle concentration after synthesis $c_0[\text{Particles}]$, static magnetic susceptibility χ_0 , number density of particles n , magnetic moment μ

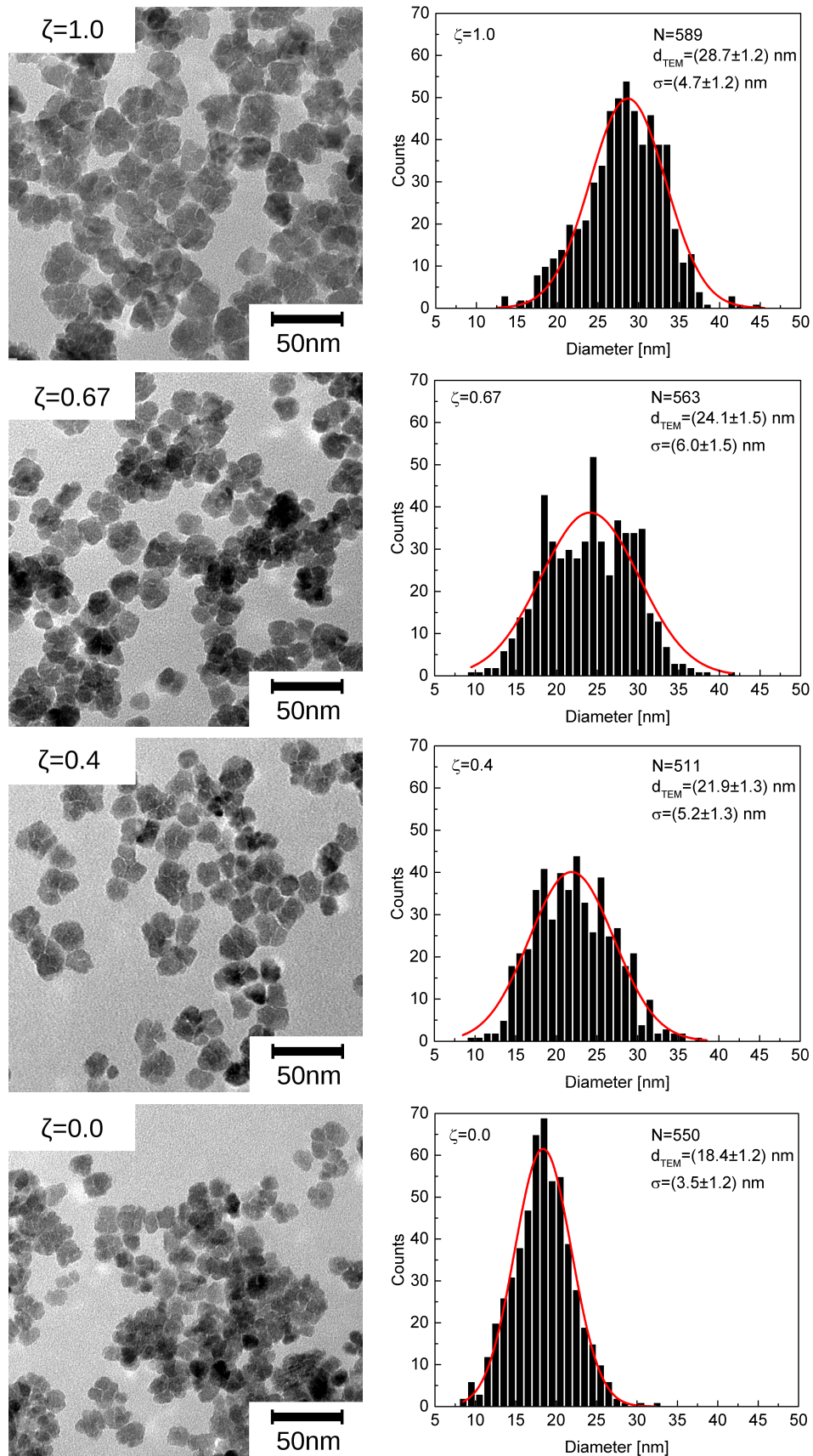


Figure 5: Exemplary TEM images of samples prepared with variable ζ and their corresponding particle size distributions. N is the number of evaluated particles, d_{TEM} is the mean value and σ is the standard deviation of the normal distribution.

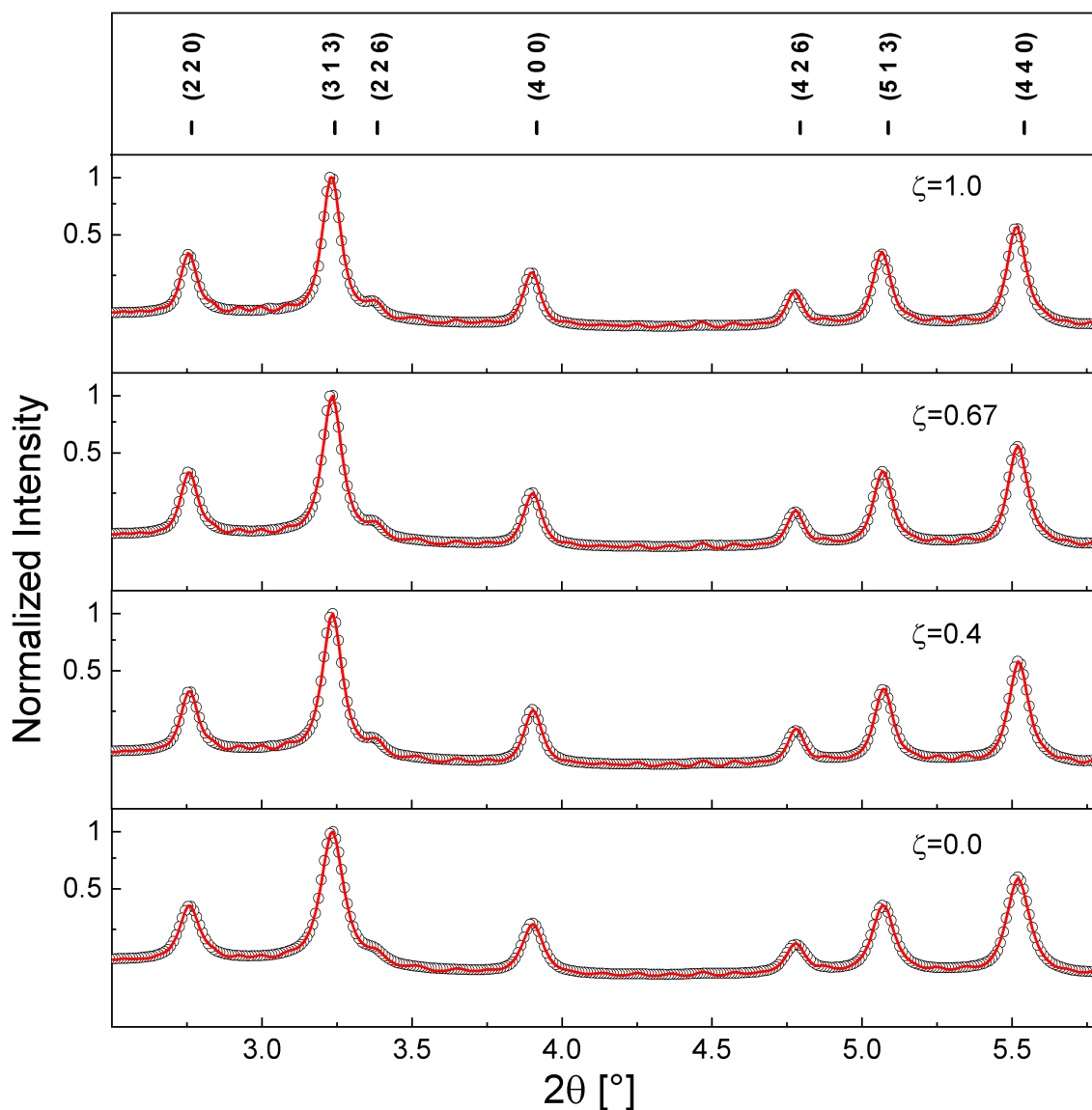


Figure 6: High energy x-ray diffractograms for samples prepared with variable ζ . Circles represent measured intensities, the solid line shows the refined intensity. Bragg reflexes of maghemite with space group $P4_12_12$ are marked and indexed.

The tetragonal crystal structure of maghemite was identified in all diffractograms (Figure 6). The lattice parameters a and c as well as the crystallite sizes d_{XRD} are given in table 7. Lattice parameters are comparable to the ones determined for sample B and C. A significant increase can be observed in crystallite size from (13.8 ± 0.3) nm for the sample prepared with $\zeta = 0$ to (18.4 ± 0.9) nm for the sample prepared with $\zeta = 1$. The Mössbauer spectra measured for the series varying ζ are shown in figure 7. The fitting model assuming four sextets delivers good agreement with the measured values. The isomer shift lies in the interval from $(0.32 \pm 0.01) \frac{\text{mm}}{\text{s}}$ to $(0.45 \pm 0.08) \frac{\text{mm}}{\text{s}}$ [97] and the quadrupole splitting is zero within the margin of error. As for the magnetic hyperfine field $\mu_0 H_{\text{hf}}$, a general trend can be observed (Figure 8). Similarly to the results from

samples B and C, the magnetic hyperfine field is smaller compared to bulk maghemite.

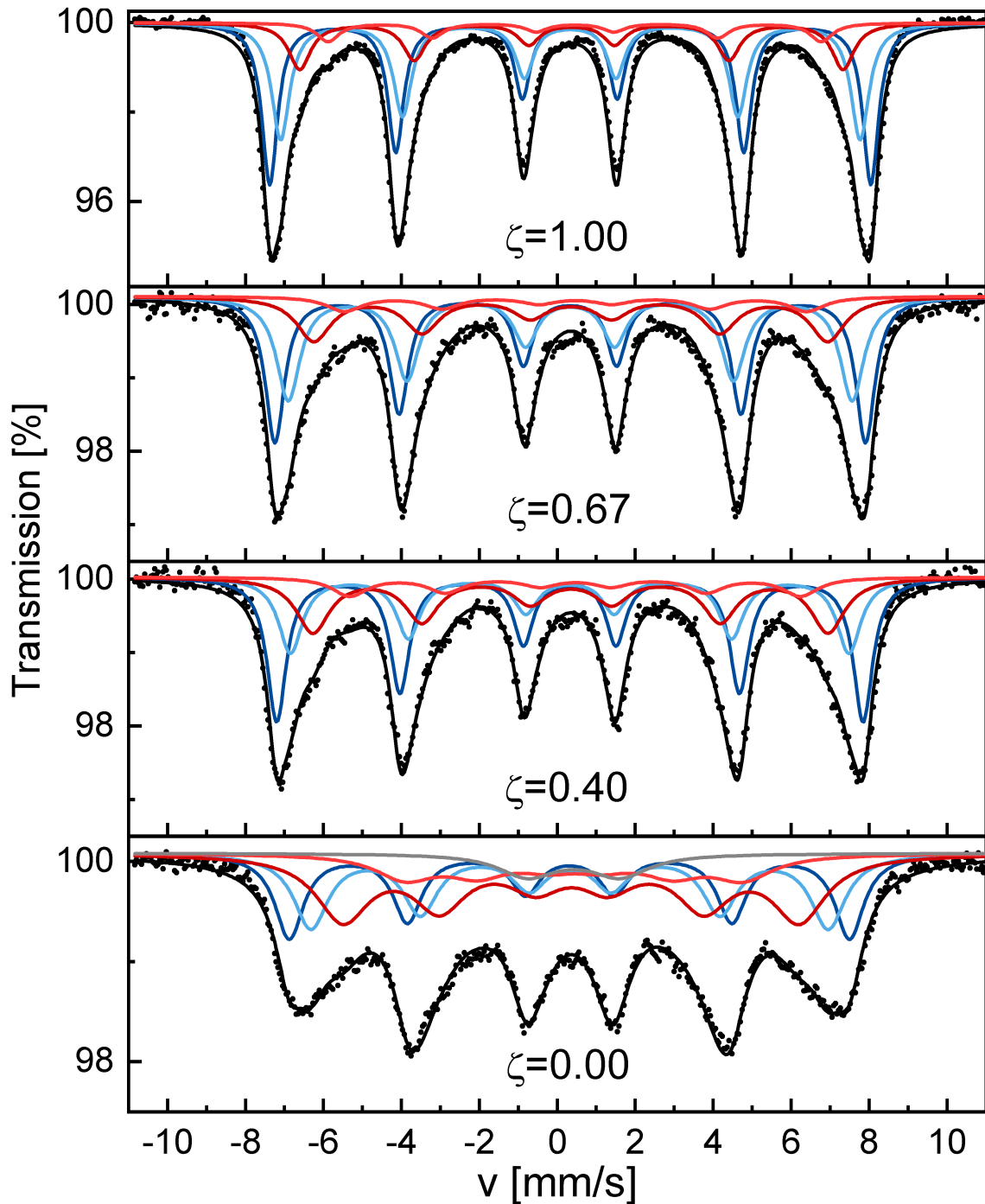


Figure 7: ^{57}Fe transmission Mössbauer spectra of samples with stoichiometry ζ . Measured data (dots), fit (black line), A_b contribution (dark red line), B_b contribution (red line), A_s contribution (dark blue line), B_s contribution (light blue line), contribution from particles in the superparamagnetic state (grey line).

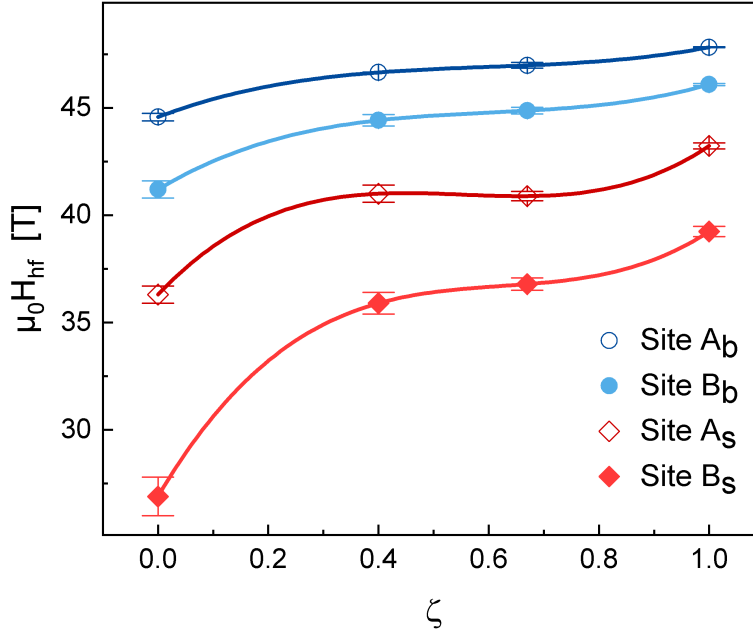


Figure 8: Magnetic hyperfine fields $\mu_0 H_{\text{hf}}$ of contributing subspectra at sites A_b (dark red), B_b (red), A_s (dark blue), B_s (light blue), calculated for samples with variable ζ . Data points are connected for better visualization.

For each sextet, $\mu_0 H_{\text{hf}}$ is reduced with decreasing ζ . The changing hyperfine field is accompanied by a change in particle size and, in particular, crystallite size as shown as in figure 8. The average magnetic hyperfine field at the iron sites \bar{H}_{Fe} can be described phenomenologically as a function of the material's magnetic moment [95],

$$\bar{H}_{\text{Fe}} = a\bar{\mu}_{\text{Fe}} + b\bar{\mu},$$

where $\bar{\mu}_{\text{Fe}}$ is the average magnetic moment of the iron atom at that site, a and b are proportionality constants, and $\bar{\mu}$ is the average magnetic moment of the alloy or chemical compound, or in this case the magnetic moment inside a particle. The magnetic moment of a multicore nanoparticle μ_{eff} depends in turn on the number of primary particles N as well as their magnetization M_S and volume V [35]:

$$\mu_{\text{eff}} = \sqrt{N}M_S V.$$

Therefore, the observed change of the hyperfine field can be regarded as a direct result of a change in crystallite size and in the degree of aggregation during nanoflower formation.

For $\zeta=0$, an additional doublet can be observed which is assigned to particles in a superparamagnetic state. The observation of superparamagnetic behaviour is only possible if the characteristic time constant of the measurement is smaller than the superparamagnetic relaxation time. In the case of Mössbauer spectroscopy this limit is in the order of 10^{-8} s [117]. This is the case for an intensity fraction of 5.6%.

Relaxation time is strongly influenced by the particle size and is shorter for smaller particles [52]. Therefore, the doublet can be assigned to the smallest, non-aggregated particles in the superparamagnetic state.

The intensity fraction of sextets assigned to the surface region I_s/I_{total} can be used to calculate particle radii r using a core-shell model [97],

$$\frac{I_s}{I_{\text{total}}} = \frac{4\pi r^2 \Delta r}{4/3\pi r^3}.$$

Assuming the shell thickness equals the shortest side length of a crystal unit cell, $\Delta r = a$, values ranging from (21.1 ± 1.0) nm to (10.8 ± 0.4) nm are obtained for $d_{\text{MB}} = 2r$ (table 6). These values are comparable to the crystallite size d_{XRD} . The assumption of a surface region thickness equal to the lattice parameter is only a rough estimate as well as the approximation of the particle geometry by a sphere. The resulting particle diameters however illustrate that the trends of the changing magnetic moments of the particles in the Mössbauer spectra are mainly a result of changing crystallite sizes and that the core-shell model describes the surface and core regions of primary particles. The intensity fraction assigned to the surface region I_s/I_{total} increases for smaller crystallites due to an increased surface to volume ratio, reaching up to $(46.6 \pm 1.5)\%$.

| ζ | I_s/I_{total} | d_{MB} [nm] |
|---------|------------------------|----------------------|
| 1.0 | 0.24 ± 0.01 | 21.1 ± 1.0 |
| 0.67 | 0.28 ± 0.01 | 17.4 ± 0.7 |
| 0.4 | 0.35 ± 0.01 | 14.3 ± 0.5 |
| 0 | 0.466 ± 0.015 | 10.8 ± 0.4 |

Table 6: Mössbauer intensity fraction of surface contributions I_s/I_{total} and resulting particle sizes d_{MB} calculated for samples with variable ζ .

| ζ | a [Å] | c [Å] | d_{XRD} [nm] | d_{TEM} [nm] |
|---------|-------------------|--------------------|-----------------------|-----------------------|
| 1.0 | 8.365 ± 0.006 | 25.161 ± 0.006 | 18.4 ± 0.9 | 28.7 ± 1.2 |
| 0.67 | 8.357 ± 0.001 | 25.164 ± 0.004 | 17.3 ± 0.6 | 24.1 ± 1.5 |
| 0.4 | 8.354 ± 0.001 | 25.149 ± 0.004 | 16.9 ± 0.5 | 21.9 ± 1.3 |
| 0 | 8.356 ± 0.001 | 25.162 ± 0.006 | 13.8 ± 0.3 | 18.4 ± 1.2 |

Table 7: Maghemite crystal lattice parameters a and c and crystallite sizes d_{XRD} for nanoflowers prepared with different stoichiometric parameters ζ , obtained by Rietveld refinement. Additionally, average particle sizes d_{TEM} derived from TEM images are shown.

2 Comparison with spherical iron oxide nanoparticles

The polyol route described previously was adapted to synthesize globular iron oxide nanoparticles. If, instead of mixing of NMDEA and DEG, only DEG is used, the formation of superstructures is inhibited and globular primary particles are obtained [50, 62]. Sample 1 was prepared using 18 mmol iron(II) chloride as iron precursor. Iron(III) chloride was the iron precursor for samples 2 to 4 and its concentration was varied as listed in table 8. To achieve this, samples were produced based on precursor solutions containing 18 mmol, 36 mmol and 54 mmol iron(III) chloride. An alkaline environment was provided by adding 0.8 wt.-% NaOH. The precursor solution was heated from room temperature to 220°C at 2 K/min under vigorous stirring in a flask equipped with a reflux condenser. Target temperature was held constant for 4 h. After thermal treatment, the mixture was left to cool down to room temperature under stirring. Next, the sediment was separated magnetically and washed three times with a 1:1 (v/v) mixture of ethanol and acetic acid ethyl ester, once with 10% nitric acid and twice with acetone. Finally, the sediments were dispersed in pure water to obtain stable suspensions.

| Sample | 1 | 2 | 3 | 4 |
|---------------------------------|-----|-----|-----|-----|
| ζ | 0 | 1 | 1 | 1 |
| T_t [°C] | 220 | 220 | 220 | 220 |
| t_h [h] | 4 | 4 | 4 | 4 |
| $n_{\text{Fe chloride}}$ [mmol] | 18 | 18 | 36 | 54 |

Table 8: Synthesis parameters for samples 1 to 4. The stoichiometric parameter ζ , target temperature T_t , holding time t_h , and molar amount of iron chloride $n_{\text{Fe chloride}}$.

2.1 Magnetic properties in dependence of the particle size

TEM images and the corresponding particle size distributions of samples 1, 2 and 3 are shown in figure 9. All samples contain more or less globular particles of different sizes. A general trend of increasing particle size with an increasing iron precursor concentration can be observed. Average particle sizes rise from (8.8 ± 1.2) nm in sample 1 to (11.3 ± 1.3) nm in sample 3. However, considering the error margins, this observation is on the limit of being insignificant. The standard deviations of the normal distributions assumed in the fitting procedure are all within each other's error margins, ranging from (2.3 ± 1.3) nm in sample 1 to (3.1 ± 1.5) nm in sample 2. It can be observed that with increasing iron precursor concentrations, there is an increasing asymmetry in particle size distributions caused by increasing number of particles larger than 18 nm.

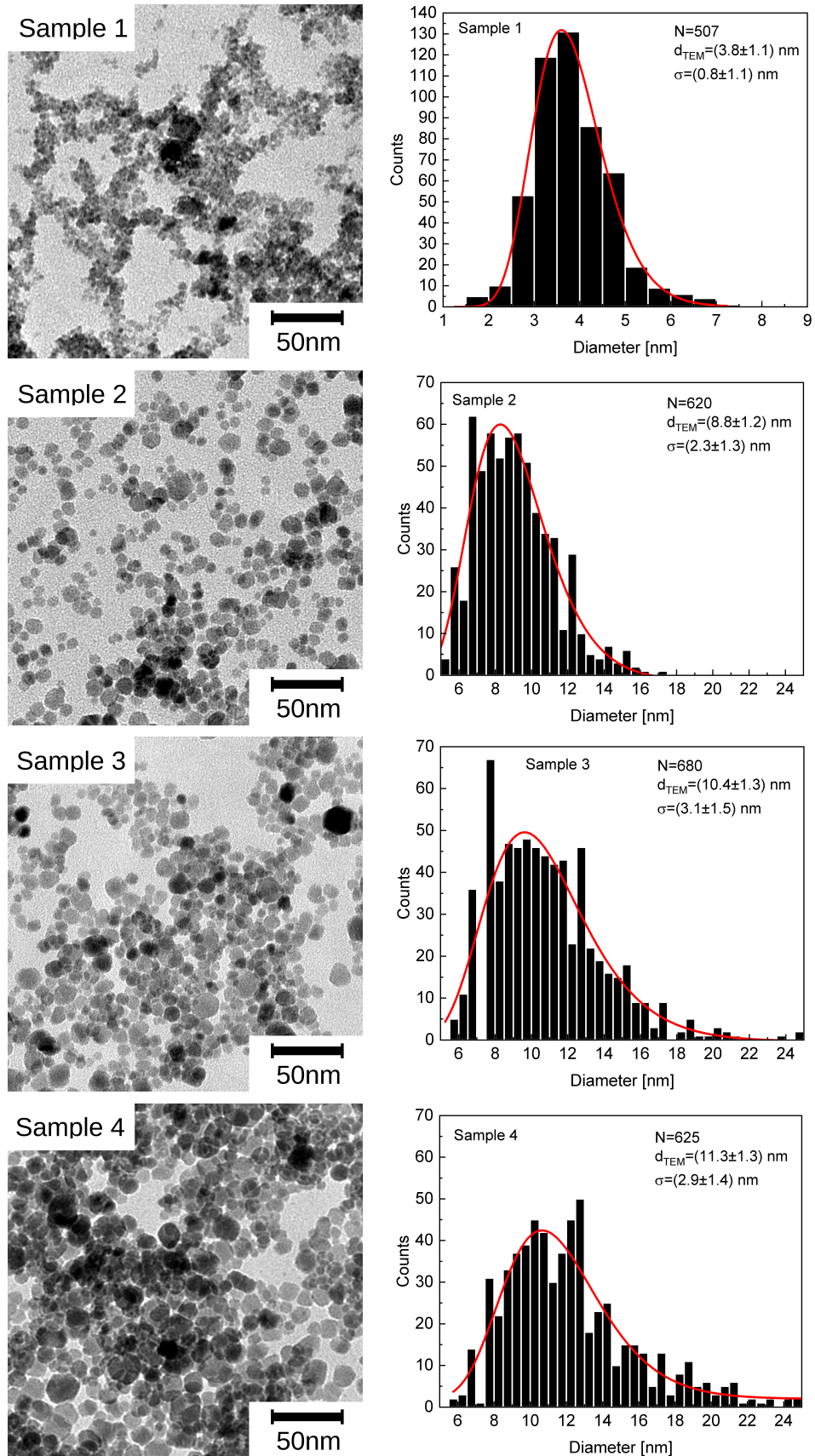


Figure 9: Exemplary TEM images for samples prepared at different precursor concentrations. N is the number of evaluated particles, d_{TEM} is the mean value and σ is the standard deviation of the normal distribution.

The samples were further investigated by frequency dependent magnetic susceptibility measurements, the susceptibility curves are shown in figure 10. The characteristic drop of the the real part of the susceptibilities and the corresponding maximum in their imaginary parts lie outside the measurement range for samples 1 to 3, indicating very short

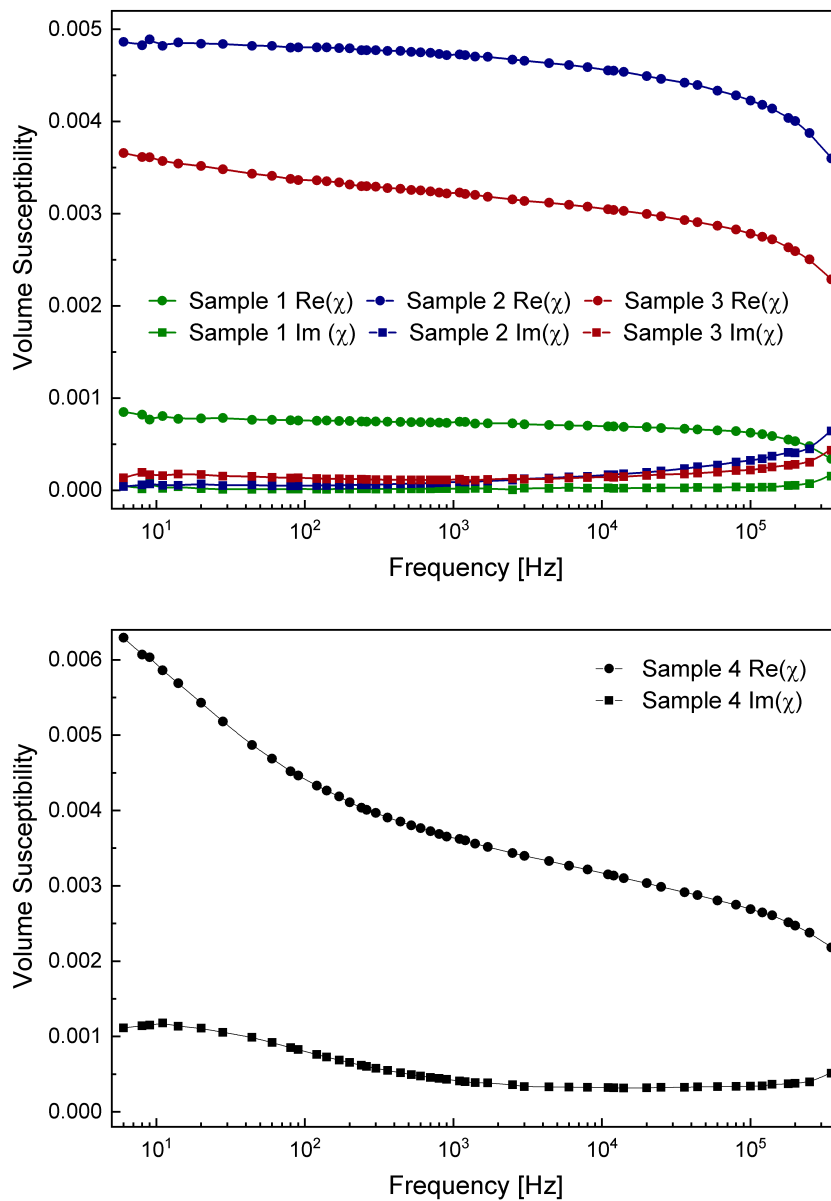


Figure 10: Susceptibility in dependence of frequency for samples prepared varying precursor concentrations. Measurements of the real part are indicated by dots, measurements of the imaginary part are indicated by squares. Sample 1 (green), sample 2 (blue), sample (red) and sample 4 (black) are shown.

| Sample | d_{TEM} [nm] | $c_0[\text{Fe}]$ [mg/ml] | $c_0[\text{Particles}]$ [mg/ml] | χ_0 [10^{-3}] | n [$10^{13}/\text{mL}$] | μ [$\text{A} \cdot \text{nm}^2$] |
|--------|--------------------------|-----------------------------|------------------------------------|---------------------------|--------------------------------|---|
| 1 | 3.8 ± 1.1 | 14.71 | 25 | 0.79 ± 0.07 | 1600 ± 1500 | 0.022 ± 0.011 |
| 2 | 8.8 ± 1.2 | 15.33 | 27 | 4.84 ± 0.07 | 135 ± 70 | 0.19 ± 0.05 |
| 3 | 10.4 ± 1.3 | 31.66 | 50 | 3.5 ± 0.3 | 73 ± 30 | 0.22 ± 0.05 |
| 4 | 11.3 ± 1.3 | 42.64 | 66 | 5.5 ± 1.5 | 56 ± 30 | 0.31 ± 0.10 |

Table 9: Particle diameter d_{TEM} , iron concentration after synthesis $c_0[\text{Fe}]$, particle concentration after synthesis $c_0[\text{Particles}]$, static magnetic susceptibility χ_0 , number density of particles n and magnetic moment μ for samples 1 to 4.

relaxation times. This is expected considering the findings for the smallest nanoflowers measuring 18.4 nm in diameter where the peak of the imaginary susceptibility also lies outside the measured frequency regime. For the much smaller, spherical particles of this sample series, even shorter relaxation times can be expected. The result of such short relaxation times can also be observed in sample 4, however another maximum in the imaginary part of the susceptibility can be found in the low-frequency regime and the real part of the susceptibility continues to rise towards lower frequencies. Therefore, the existence of two populations of particles with different size distributions needs to be considered for sample 4. Yet, the particle size distribution determined from TEM images does not give any evidence for this. Possibly, the curve shape of the magnetic susceptibility is due to agglomeration. As described previously, longer relaxation times are expected for larger structures, making large agglomerates responsible for the observed behaviour. Given these uncertainties, the susceptibility curves are not analysed using a fitting model. Instead, the behaviour in the low-frequency regime is examined. A general trend of increasing initial static susceptibilities with increasing particle size can be observed with the exception of sample 3. From sample 2 to sample 3, a reduced susceptibility is measured overall despite the increasing average particle size. In order to understand this behaviour, the parameters of the suspension need to be analysed in the same way as described in the previous section. Dynamic magnetic susceptibility measurements were conducted at a fixed iron concentration of 1 mg/ml. Depending on the particle size and iron content per particle, this iron concentration of the suspension may result in different particle number densities. These parameters are taken into account in the calculation of magnetic moments, allowing for a better comparability of results. The average magnetic moment per particle was determined as described earlier. Iron and particle concentrations after synthesis, static magnetic susceptibility, number density of particles at 1 mg/ml iron concentration and the resulting magnetic moments are shown in table 9. Magnetic moments ranging from $(0.022 \pm 0.011) \text{ A} \cdot \text{nm}^2$ to $(0.31 \pm 0.10) \text{ A} \cdot \text{nm}^2$ are obtained, strictly increasing along with particle size. These values are very low compared with the magnetic moments of nanoflowers. Magnetic nanoflowers, being superferrimagnetic structures, exceed the size of superparamagnetic primary particles and therefore exhibit greater magnetic moments and longer relax-

ation times. The spherical particles examined in this section, on the other hand, are characterized by very fast relaxation and low magnetic moments. As shown by particle size analysis, they are for the most part below the size limit for superparamagnetic behaviour appearing around 10 nm [29]. The dynamic susceptibility curve of sample 4 pointing to particle agglomeration may well be explained by a beginning transition from the superparamagnetic to the blocked state, making it difficult to obtain stable suspensions of bigger particles [118].

3 Preparation and optimization of polymer coatings

In the following, the development of a PMMA-based composite coating is presented. The goal is to incorporate maghemite nanoflowers originating from the polyol-based synthesis described earlier into a homogeneous polymer layer. With the intention of finding a coating routine that can be applied to three-dimensional, porous titanium-based bone implant surfaces, simple dip coating using a polymer solution is the method of choice. Achievable layer thickness and roughness are initially assessed using glass substrate. The next step is to find favourable conditions for evenly distributing the maghemite nanoflowers over a titanium surface. Finally, a thin PMMA composite coating on titanium substrate containing maghemite nanoflowers is successfully prepared.

3.1 Single dip coatings on glass substrate

In order to obtain an overview over the achievable layer thicknesses using simple dip coating with PMMA dissolved in acetone, a model system is needed which can be easily examined by AFM. Most importantly, a microscopically smooth surface is needed to accurately measure the coating thickness. Additionally, a surface with little or no reflectivity is preferable in order to avoid interference with the laser beam used to measure cantilever deflection. Glass slides are a commonly used substrate for a first examination of surface coatings, as they meet the requirements mentioned to a sufficient extent [119]. Prior to the coating process, each glass slide was cleaned with isopropanol, treated in an ultrasonic bath, rinsed with pure water and left to dry. The PMMA solution in acetone was prepared a few days before coating to make sure that PMMA dissolves completely. The average molecular weight of the polymer was $M_w = 550000 \frac{\text{g}}{\text{mol}}$. Solutions of different concentration were prepared as a dilution series. To apply the PMMA coating, the glass slider was dipped into the PMMA solution and slowly withdrawn. Samples were left to dry for at least an hour before examination by AFM. In order to prepare cross sections of the coating, small parts were scratched away using a scalpel. Scans of these cross sections were evaluated by extracting height profiles along the step edge, calculating average coating and substrate levels for each of them, with their difference being the layer thickness (see figure 11). The layer thicknesses d_{layer} stated in table 10 are the average of these profile measurements, with an error interval resulting from standard deviation, as statistical errors are dominant. Average surface roughness is given as the root-mean-square R_{rms} . As layer thickness varies by two orders of magnitude over the sample series, it is difficult to compare surface roughness. Therefore, the relative roughness R_{rel} is introduced with

$$R_{\text{rel}} = \frac{R_{\text{rms}}}{d_{\text{layer}}}.$$

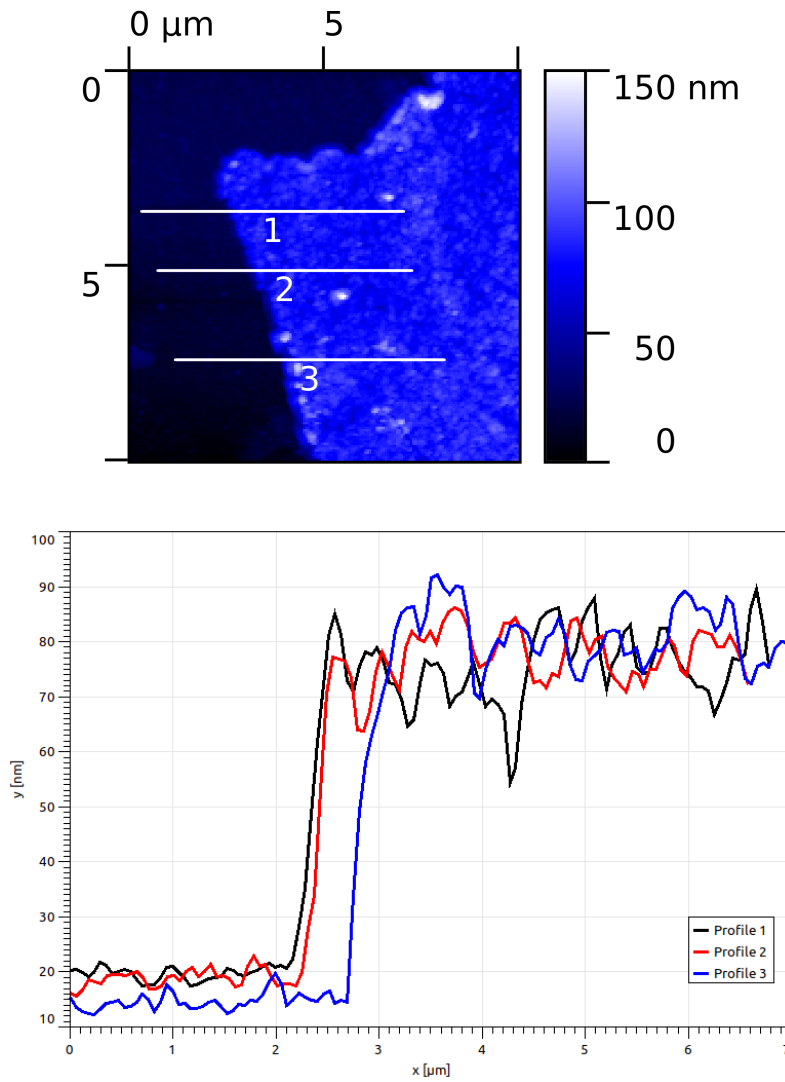


Figure 11: The extraction of height profiles from AFM scans is shown here exemplarily for 0.5 wt.-% PMMA concentration. The layer thickness is calculated from the difference between average substrate and coating levels.

| c_{PMMA} [wt.-%] | 5.0 | 2.5 | 1.25 | 0.5 | 0.25 | 0.10 |
|---------------------------|----------|--------|--------|-------|-------|-------|
| d_{layer} [nm] | 1500±300 | 290±40 | 128±30 | 71±40 | 61±14 | 30±30 |
| R_{rms} [nm] | 45.7 | 4.5 | 7.4 | 7.6 | 7.5 | 10.1 |
| R_{rel} [%] | 3.1 | 1.6 | 5.8 | 10.7 | 12.3 | 33.3 |

Table 10: PMMA concentration c_{PMMA} in acetone, layer thickness d_{layer} of the resulting coating, the average root-mean-square surface roughness R_{rms} and the roughness relative to the coating thickness, R_{rel} .

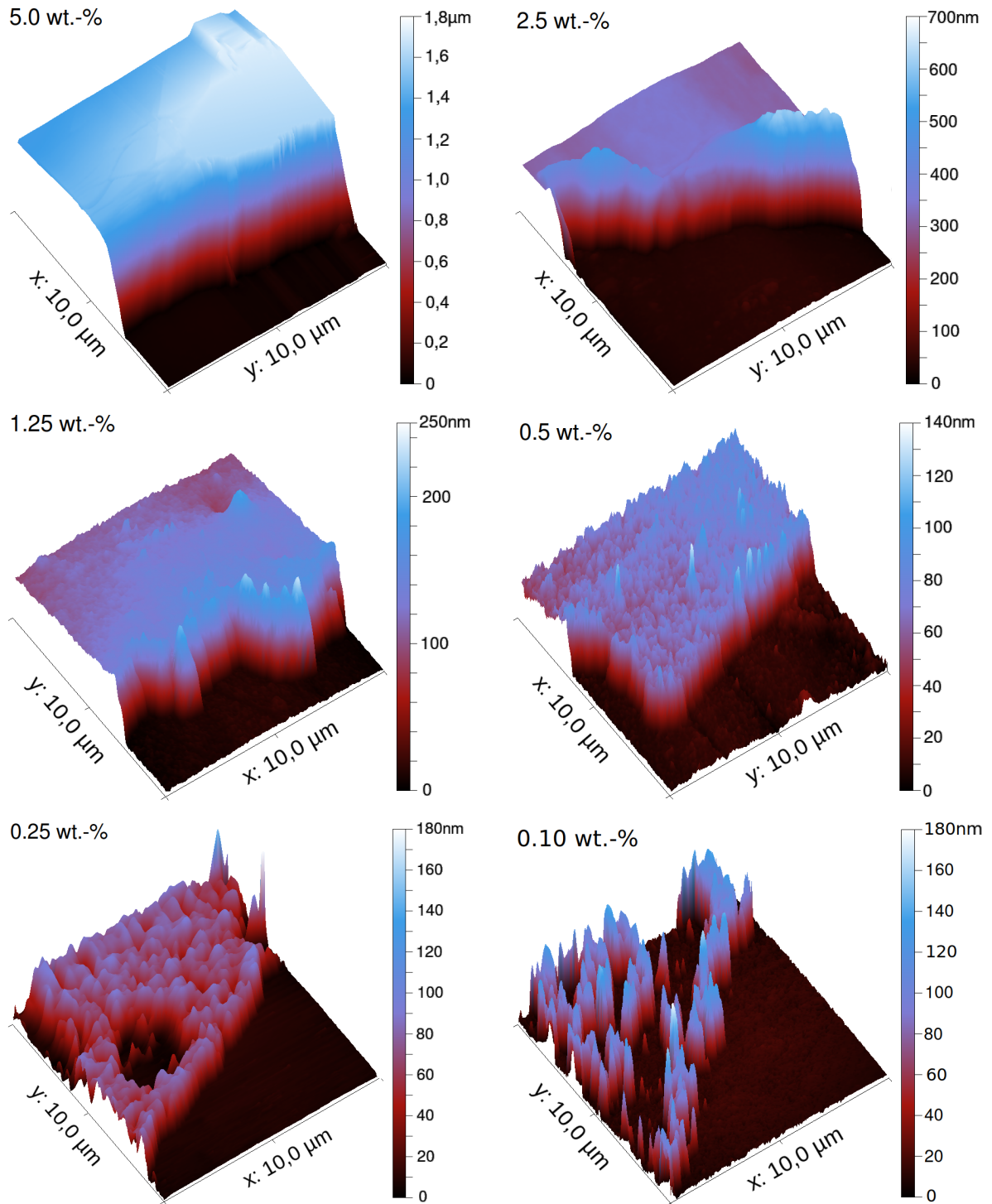


Figure 12: AFM topography scans of samples prepared by dip coating a glass slide in a solution of PMMA in acetone, while varying the concentration from 5 wt.-% to 0.1 wt.-%. Cross sections of the surface layer were prepared by scraping with a scalpel.

As visible in table 10, PMMA coatings with thicknesses ranging from $(1.5 \pm 0.3) \mu\text{m}$ to $(30 \pm 30) \text{ nm}$ were prepared. Comparing the surface morphology of the coatings presented in figure 12, one can see that smooth coatings are possible using 5 wt.-% and 2.5 wt.-% PMMA. This is underlined by the relative surface roughness which is lowest for these samples. However in absolute numbers, roughness decreases by a factor 10 from 45.7 nm for 5 wt.-% to 4.5 nm for 2.5 wt.-%. The latter is the lowest value obtained for absolute surface roughness. For 1.25 wt.-% and 0.5 wt.-%, an increase in surface roughness is observed, continuing for coatings with 0.25 wt.-% and 0.1 wt.-% which are highly irregular and do no longer cover the substrate homogeneously. During this transition, holes appear in the layer, followed by the formation of islands. The observed decreasing layer thickness with decreasing PMMA concentration, along with the increasing surface roughness are in line with the measured values (see Figure 13). Lowering the concentration, layer thicknesses around 100 nm are feasible. For PMMA concentrations below 1 wt.-%, an accelerating increase in relative roughness is observed, revealing the degradation of homogeneity. Therefore, the limit of this method is reached in this regime.

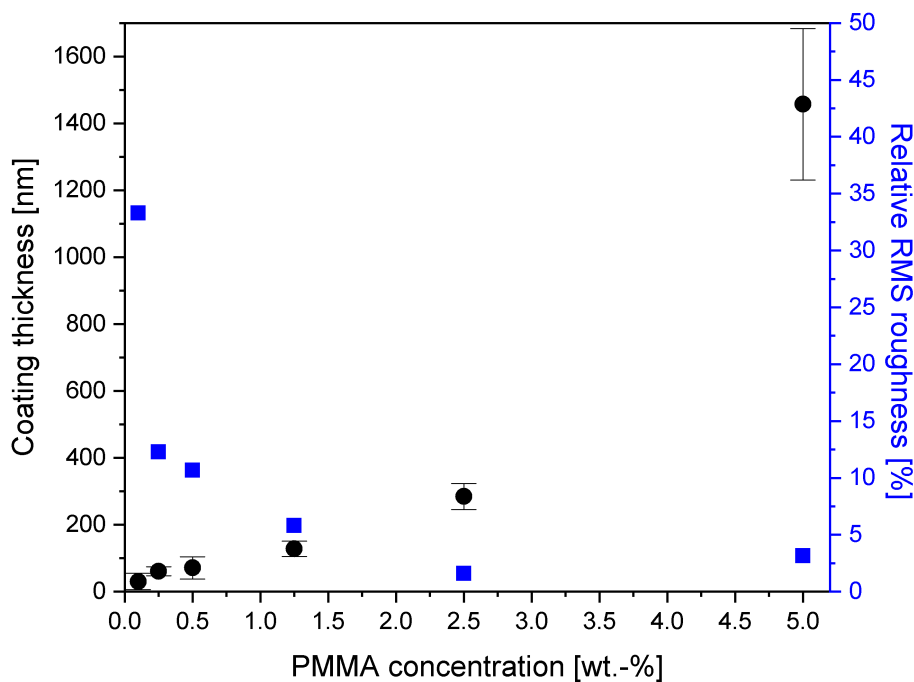


Figure 13: Mean layer thicknesses (black dots) are plotted in dependence of the PMMA concentration. The relative root-mean-square roughness is plotted on a separate scale (blue squares).

3.2 Double dip coatings on glass substrate

The previously described dip coating process fails to deliver homogeneous surface coatings thinner than 100 nm. To further decrease this limit, a second application of the coating is favourable, as it has been shown that this can create a smoother surface [120]. Therefore, the dip coating was applied twice in the following sample series, with 10 seconds drying time in between. The AFM topography scans of cross sections prepared with 0.50 wt.-% to 0.10 wt.-% PMMA concentration are shown in Fig 14. As expected, coatings are more homogeneous and holes occur only at 0.15 wt.-% PMMA and less. However, surfaces are still rough. This is reflected by the analysis of height profiles extracted from AFM measurements, as shown in table 11 and figure 15. The coating thickness ranges from (130 ± 40) nm to (25 ± 30) nm. For concentrations of 0.50 wt.-% to 0.20 wt.-%, both coating thickness and surface roughness are close to the values for single coatings, however a more homogeneous coverage of the surface was achieved. The lowest absolute roughness is 5.5 nm and is obtained for 0.25 wt.-% which is only a tenth of the concentration of lowest absolute roughness for single dip coatings. The coatings on samples prepared with 0.15 wt.-% and 0.10 wt.-% PMMA show no significant change in thickness, however they are strongly inhomogeneous, and they show an increased absolute and relative surface roughness. Therefore, it can be concluded that the thinnest and most consistent coating layer is formed at 0.25 wt.-%, with an average thickness of (46 ± 7) nm and 11.9 % relative surface roughness. Layer thickness needs to be considered in relation to the size distributions of nanoflowers synthesized in this work. Very few particles exceed a diameter of 35 nm. For this reason, a PMMA of this dimension will be able to protect the nanoflowers from degradation and from being released into the organism. At the same time, it is crucial to avoid making the coating unnecessarily thick in order to maximize the exposure of bone cells to the particle's stray fields. Additionally, it is important to mention that such a nanoscale surface coating will have only little impact on the bone implant structure with respect to pore size, which is ideally a few hundred micrometers [7].

| c_{PMMA} [wt.-%] | 0.50 | 0.25 | 0.20 | 0.15 | 0.10 |
|---------------------------|-------------|-----------|------------|------------|------------|
| d_{layer} [nm] | 130 ± 40 | 46 ± 7 | 40 ± 30 | 41 ± 10 | 30 ± 30 |
| R_{rms} [nm] | 13.5 | 5.5 | 7.1 | 12.8 | 9.1 |
| R_{rel} [%] | 10.7 | 11.9 | 19.4 | 31.3 | 36.7 |

Table 11: PMMA concentration c_{PMMA} in acetone, layer thickness d_{layer} of the resulting coating, the average root-mean-square surface roughness R_{rms} and the roughness relative to the coating thickness, R_{rel} .

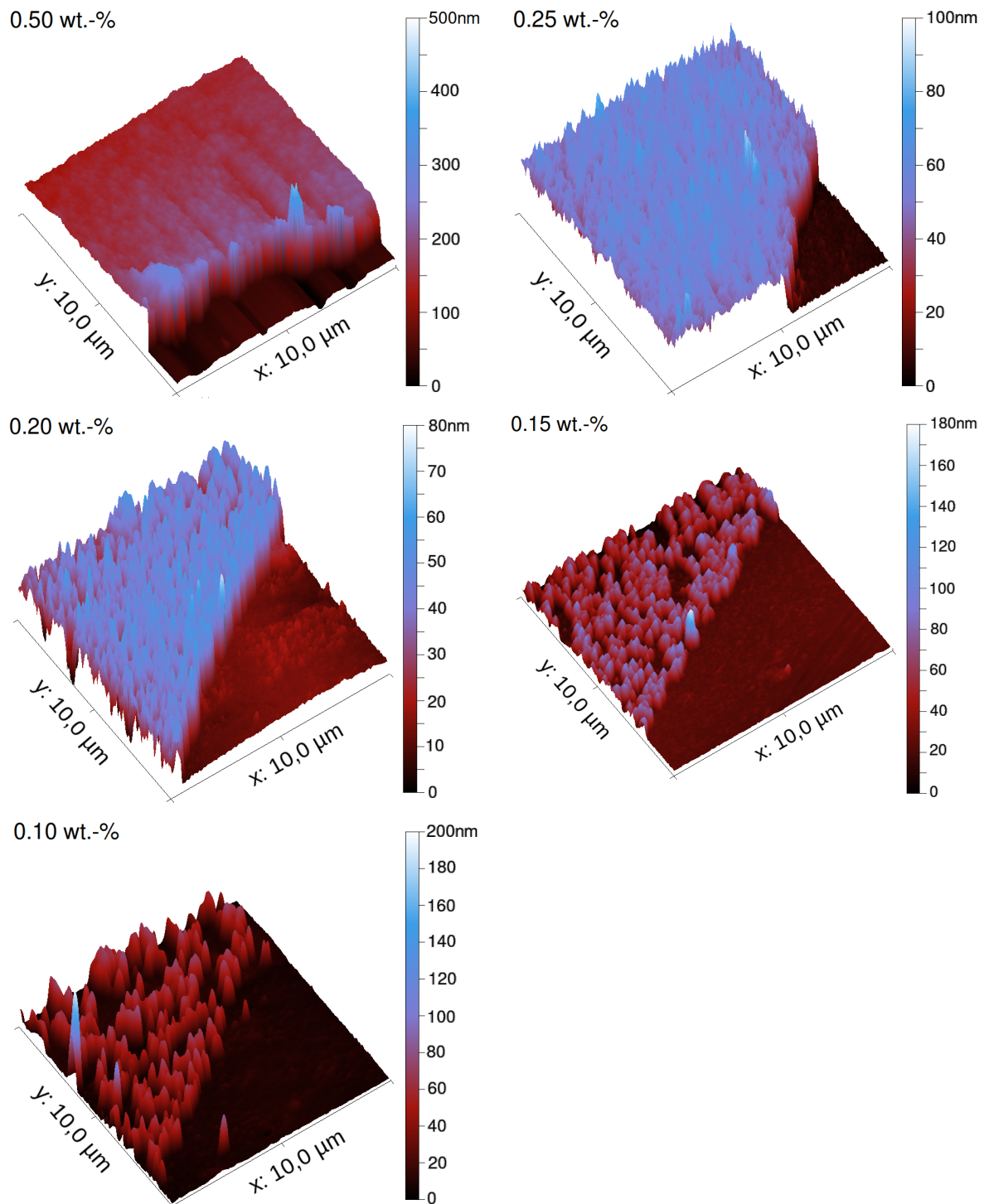


Figure 14: AFM topography scans of samples prepared by dip coating a glass slide twice in a solution of PMMA in acetone, while varying the concentration from 0.50 wt.-% to 0.1 wt.-%. Cross sections of the surface layer were prepared by scraping with a scalpel.

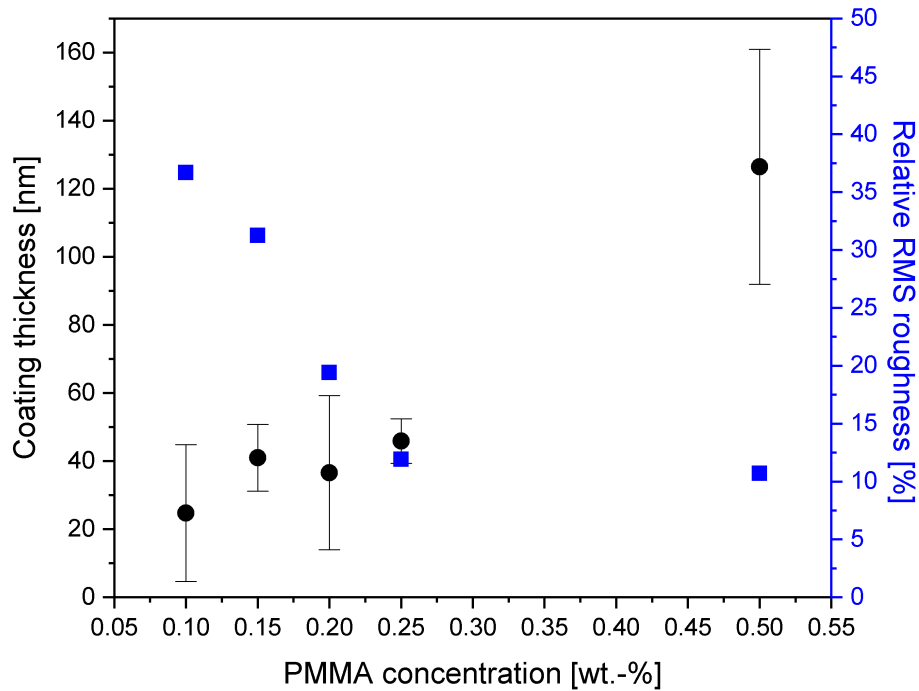


Figure 15: Mean layer thicknesses (black dots) are plotted in dependence of the PMMA concentration. The relative root-mean-square roughness is plotted on a separate scale (blue squares).

3.3 Application of magnetic nanoflowers to titanium surfaces

As a first approach for embedding nanoflowers in a PMMA composite coating on a titanium surface, they were added directly to the PMMA solution in acetone. During sample preparation, it was observed that it is hardly possible to disperse the nanoflowers in the PMMA solution, a visible sediment of agglomerated particles is formed. Upon investigation by SEM, it was found that particles with a size of $10\ \mu\text{m}$ to $20\ \mu\text{m}$ were deposited on the titanium substrate (Figure 16). By EDX element mapping, it was found that these agglomerates have a high iron content which confirms that they consist of maghemite nanoflowers. Due to the strong agglomeration, their nanoscale structure is lost, rendering this coating procedure unusable for the desired application. The magnetic properties of the particles are strongly altered if they are in close contact with each other [33]. If the implant system is to rely exclusively on the relaxation of these particles, close contact and increased interaction between particles will be detrimental.

Therefore, the method is altered. The nanoparticles and the PMMA layer are applied separately to avoid complications. As a first test, maghemite nanoflowers are applied by dip coating using an aqueous suspension (see Figure 17). Investigations by SEM show that a densely packed layer of nanoflowers forms on the titanium surface. Compared with the previous sample, an improved homogeneity of the coating is observed.

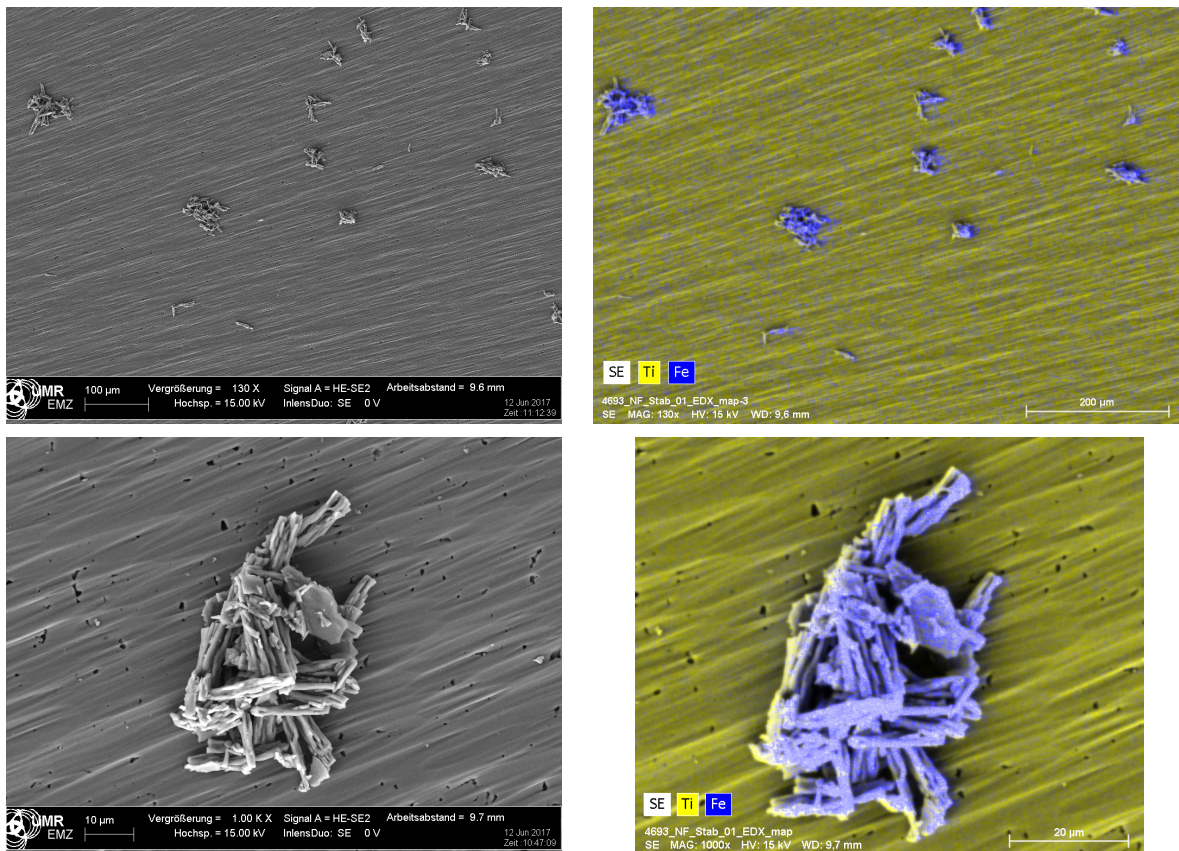


Figure 16: After dip coating with (28.7 ± 1.2) nm maghemite nanoflowers added directly to a 0.5wt.-% PMMA solution in acetone, agglomerates in excess of $10 \mu\text{m}$ in size are observed. SEM images (left) and EDX mapping (right) for the elements Ti (yellow) and Fe (blue) are shown.

However, with respect to the application on bone implants, the more or less closed layer has some disadvantages. Firstly, the close contact between particles is undesirable with respect to magnetic relaxation properties, as mentioned earlier. Secondly, if a PMMA coating is applied on top of this layer, it would have no contact with the titanium implant and therefore could possibly exhibit compromised mechanical properties such as weaker adhesion and lower scratch resistance.

In order to avoid the agglomeration of particles during the coating process the formation of a liquid film on the substrate should be avoided. This way, particles are immobilized and will remain dispersed. Besides this, the amount of particles applied should be controlled so that ideally, only a single layer is formed. These requirements are met by the spray coating technique which is a versatile method for the preparation of functional nanoscale layers [121]. A straightforward implementation of this technique is realized by using a conventional airbrush. This device produces an aerosol by letting a stream of air pass by a nozzle containing the coating liquid which is in

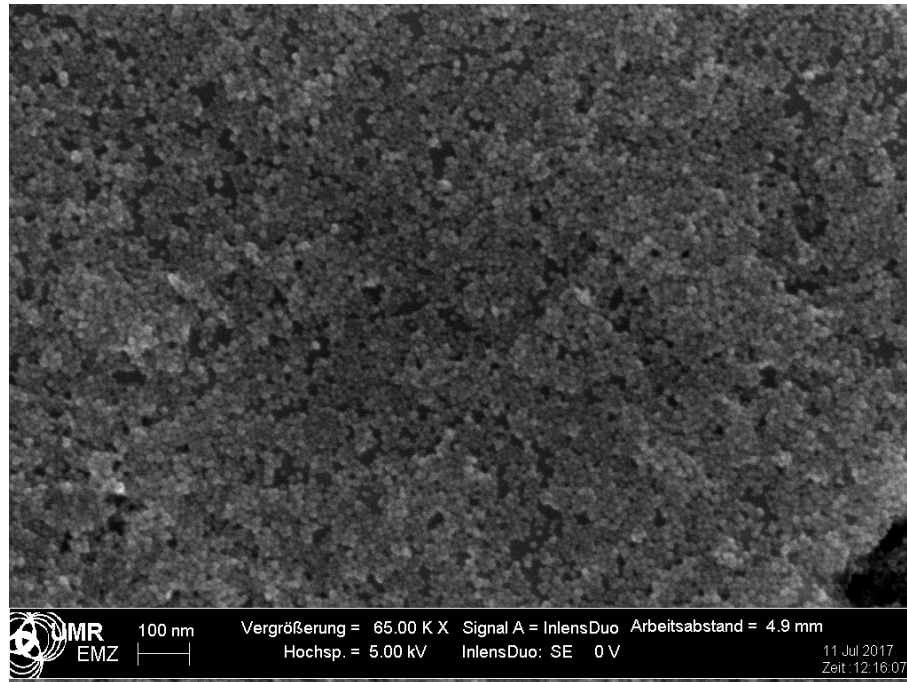


Figure 17: The SEM image shows a titanium surface after dip coating with an aqueous suspension of maghemite nanoflowers with a diameter of (28.7 ± 1.2) nm.

this case an aqueous suspension of nanoflowers. The air stream carries along small droplets ejected from the nozzle. A schematic picture of an airbrush is shown in Figure 18. It is important to control the amount of aerosol sprayed onto the substrate in such a way that coalescence of droplets is avoided and drying takes place quickly

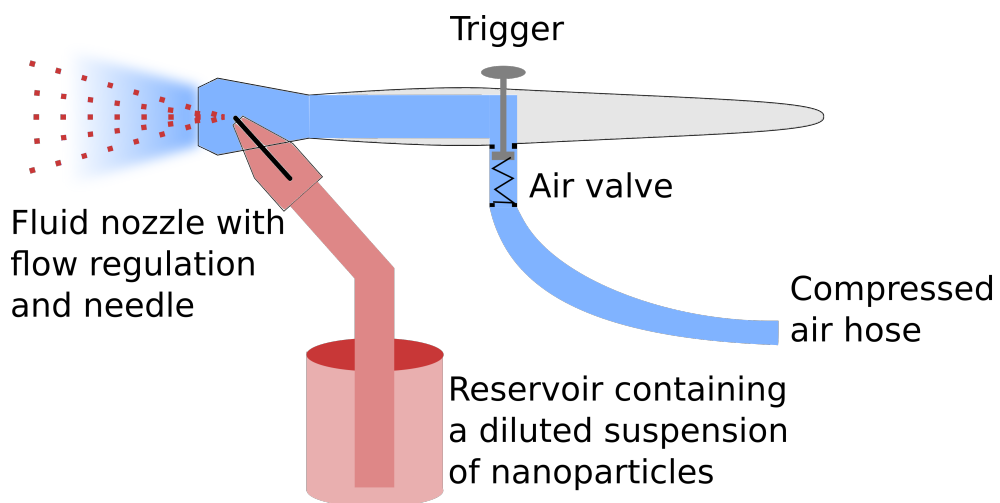


Figure 18: Schematic picture of the spray coating process, using an airbrush to apply an aqueous suspension of nanoparticles while avoiding aggregation.

enough to immobilize particles. This means that the finer the aerosol is, the more homogeneous coatings can be achieved. Compared with dip coating, this technique has great advantages: a much smaller volume of coating suspension is needed and the properties of the coating are easily reproducible if the concentration, spraying duration and drying time are controlled. In combination with a rotating substrate holder, the airbrush has already been integrated into a spray coating procedure for the application of a bioactive coating on titanium cylinders for an in vivo study [122].

Using the technique described above, an aqueous dispersion of maghemite nanoflowers was applied to the titanium substrate. The aerosol was applied in three pulses of 1 s duration, with 10 s drying time in between, using a Silverline airbrush with 2 bar air pressure and 0.8 mm nozzle diameter [123], operating at the finest setting. In this way, fine droplets were deposited on the substrate, visibly drying within a few seconds. Investigation by SEM reveals a mostly even distribution of monodisperse nanoflowers (Figure 19). While some larger agglomerates are visible, most of the structures are between 15 nm and 30 nm in diameter and can therefore be identified as non-agglomerated nanoflowers. This shows that the setup delivers the desired distribution of particles.

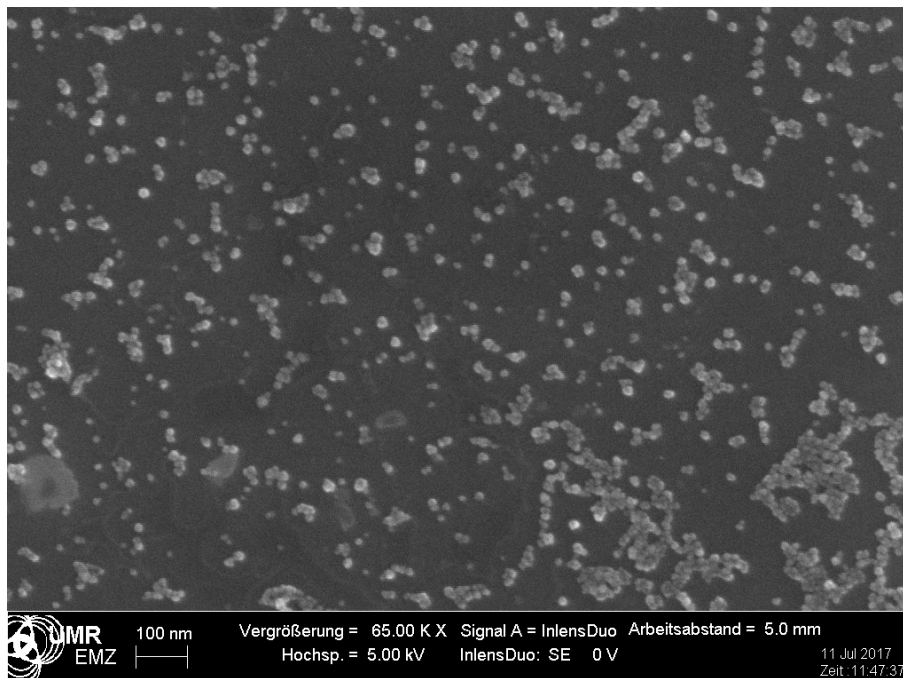


Figure 19: The SEM image shows a titanium surface after spray coating using an airbrush loaded with an aqueous suspension of maghemite nanoflowers with a diameter of (28.7 ± 1.2) nm.

3.4 Composite coatings on titanium substrate

With maghemite nanoflowers successfully applied via spray coating, using the exact same procedure as described previously, the PMMA dip coating was added in a second step. PMMA dip coating was applied twice, with 10 seconds drying time in between. Samples with 0.20wt.-%, 0.25wt.-%, 0.50wt.-% and 1.0wt.-% PMMA in acetone were prepared.

These composite coatings were investigated by SEM. As visible in figure 20 and figure 21, a mostly even distribution of nanoflowers on the titanium surface was achieved. However, local variations in particle distribution are present. Again, particles measure about 15 nm to 35 nm, showing that agglomeration was avoided to a large extent. Figure 21 shows some agglomerated particles, likely due to a slight variation in the coating process. The PMMA surface layer can be identified as it covers magnetic nanoparticles and reduces their visibility in the image. Only a small fraction of the surface is covered by PMMA, large holes are visible.

When dip coating is performed with PMMA concentrations 0.5 wt.-% (Figure 22) and 1.0 wt.-% (Figure 23), homogeneous PMMA films are achieved. No irregularities such as holes or agglomerates are observed. Maghemite nanoflowers appear blurred. This is due to the fact that the electron beam is able to penetrate the thin surface layer, allowing the nanoflowers to generate image contrast, however due to strong interaction with this surface film, it is not possible to obtain a clear image. Figure 23 shows the edge of an area that was not reached by the PMMA coating. Nanoflowers appear slightly different compared to previous images. Firstly, they have an almost featureless, spherical shape. Secondly, particles are slightly enlarged, especially near the coating's edge. Here, almost all particles are around 35 nm large. Possibly, these observations indicate that during the coating process, a PMMA layer formed around some of the particles that were not covered by the coating. As described above, the different resolution of particles with and without PMMA cover illustrates the effect of the coating on the image quality.

Comparing the samples with respect to how particles are distributed over the surface, some differences appear. In the sample shown in figure 20, particles are almost ideally dispersed. Figures 22 and 23 are difficult to interpret in this respect, yet no large agglomerates are visible. The coating in figure 21 has a quite different appearance, exhibiting more pronounced agglomeration. The varying PMMA concentration does not deliver a plausible explanation for these changes, as it is applied on top of the particles. Preliminary tests showed that particles exhibit strong adhesion with the surface, making it difficult to remove particles from the surface once applied. Fluctuations in the spray coating application of nanoflowers are a more likely reason for these observations. This shows the limitations to the manual operation of the airbrush and underlines the need of an automated setup for obtaining more reproducible results.

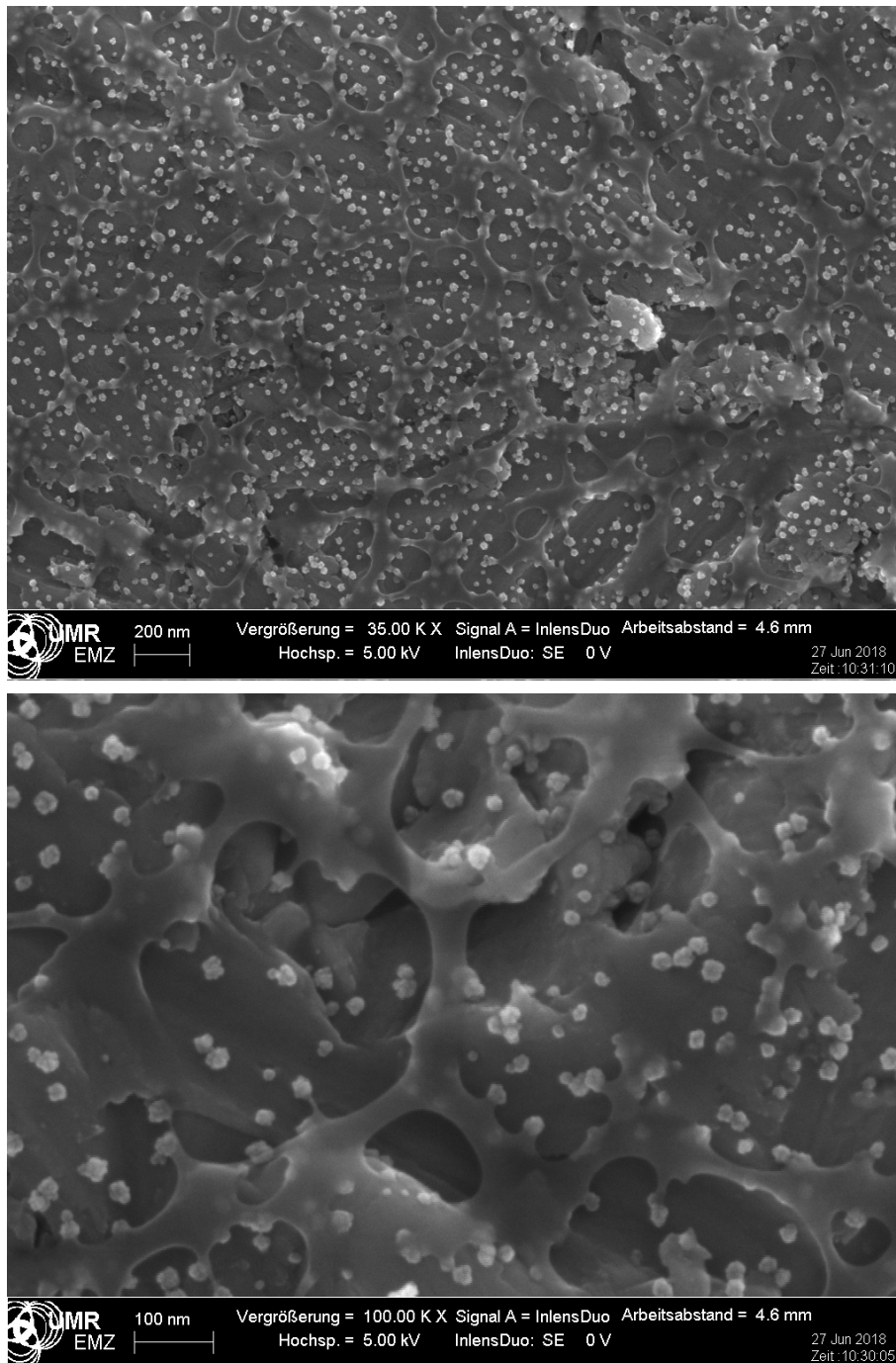


Figure 20: The SEM image shows a titanium surface with composite coating. Maghemite nanoflowers were applied by spray coating, followed by the application of a 0.20wt.-% PMMA solution in acetone by dip coating. The nanoflower diameter before coating is (28.7 ± 1.2) nm.

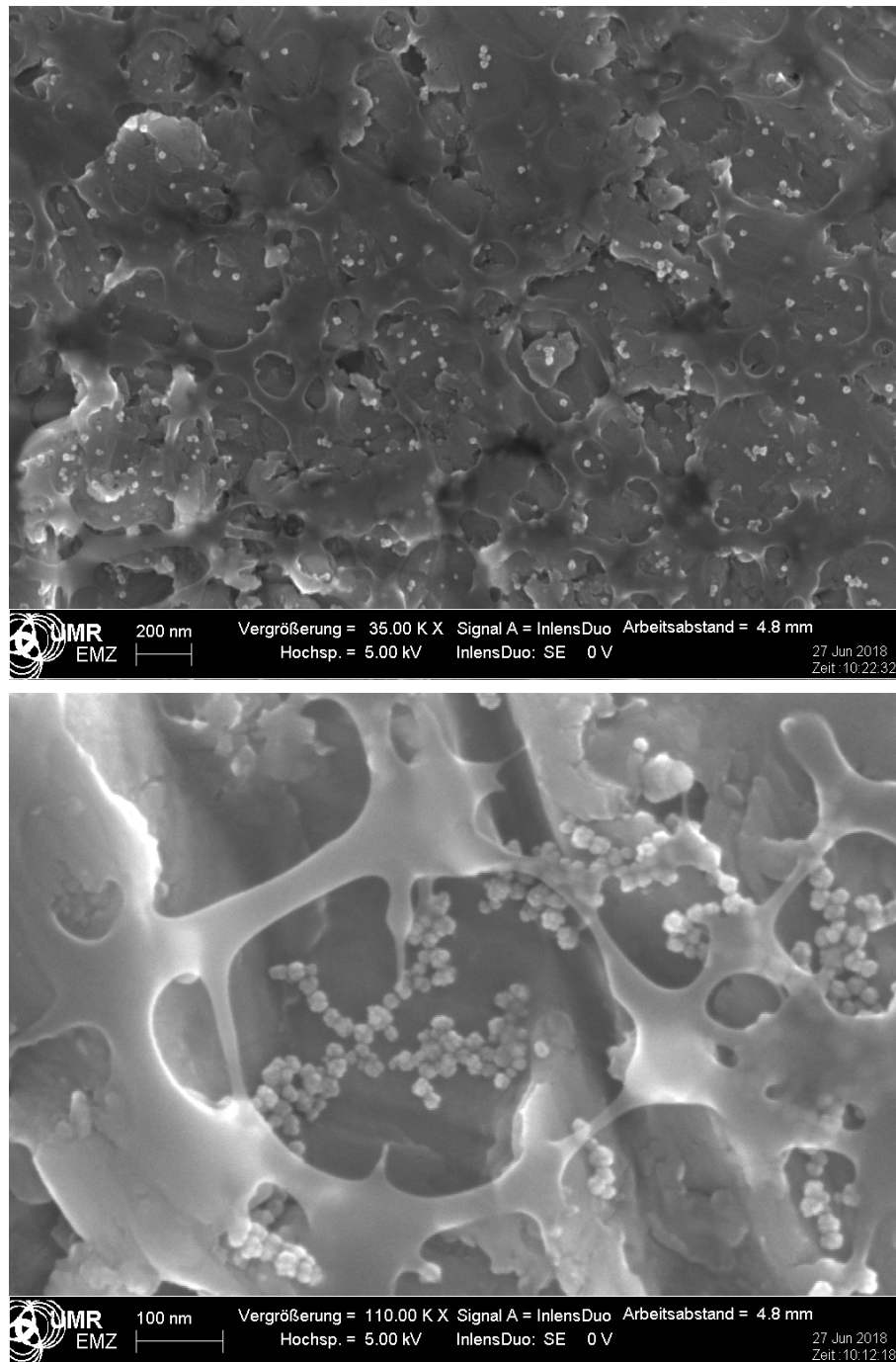


Figure 21: The SEM image shows a titanium surface with composite coating. Maghemite nanoflowers were applied by spray coating, followed by the application of a 0.25wt.-% PMMA solution in acetone by dip coating. The nanoflower diameter before coating is (28.7 ± 1.2) nm.

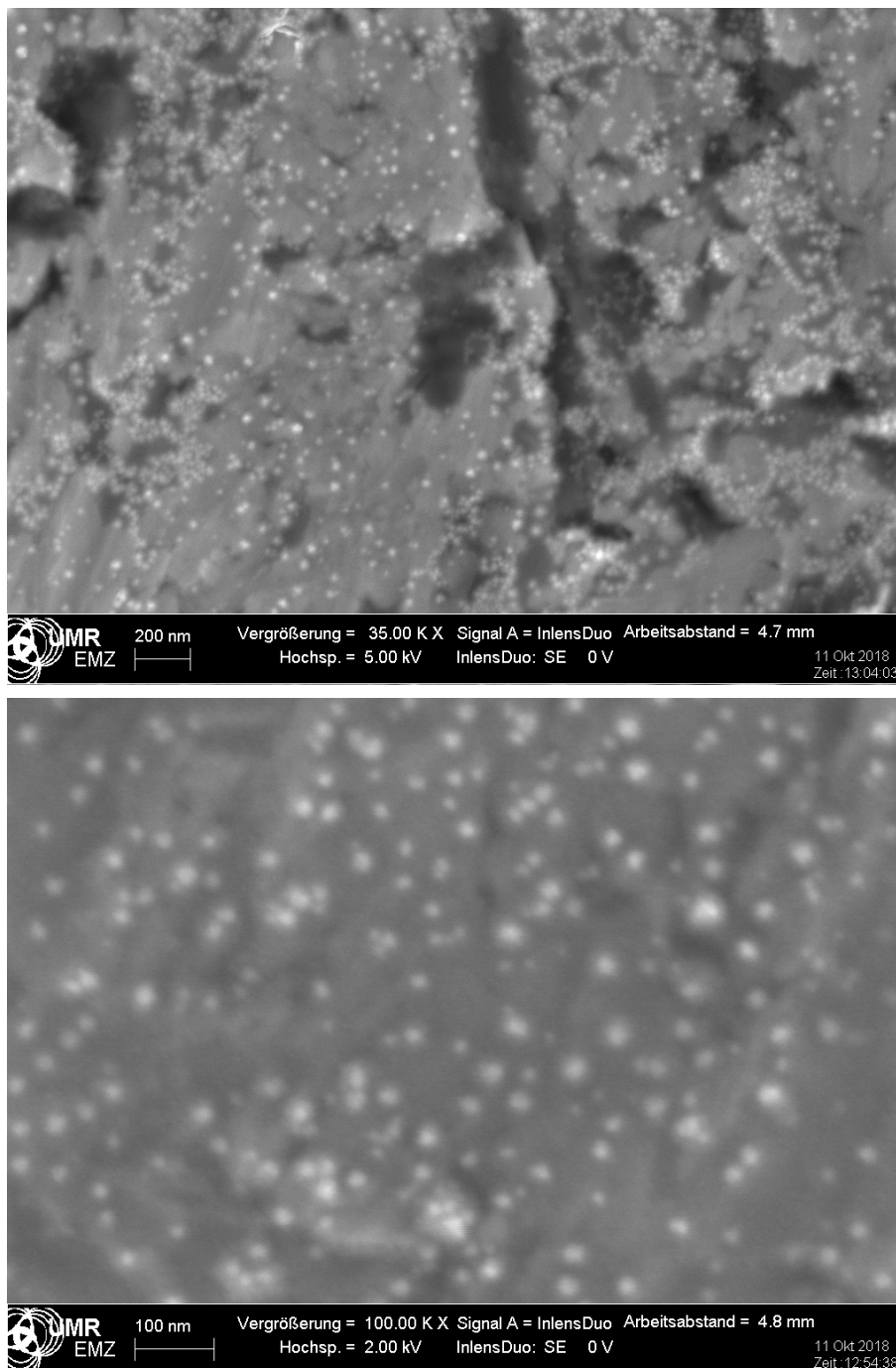


Figure 22: The SEM image shows a titanium surface with composite coating. Maghemite nanoflowers were applied by spray coating, followed by the application of a 0.50wt.-% PMMA solution in acetone by dip coating. The nanoflower diameter before coating is (28.7 ± 1.2) nm.

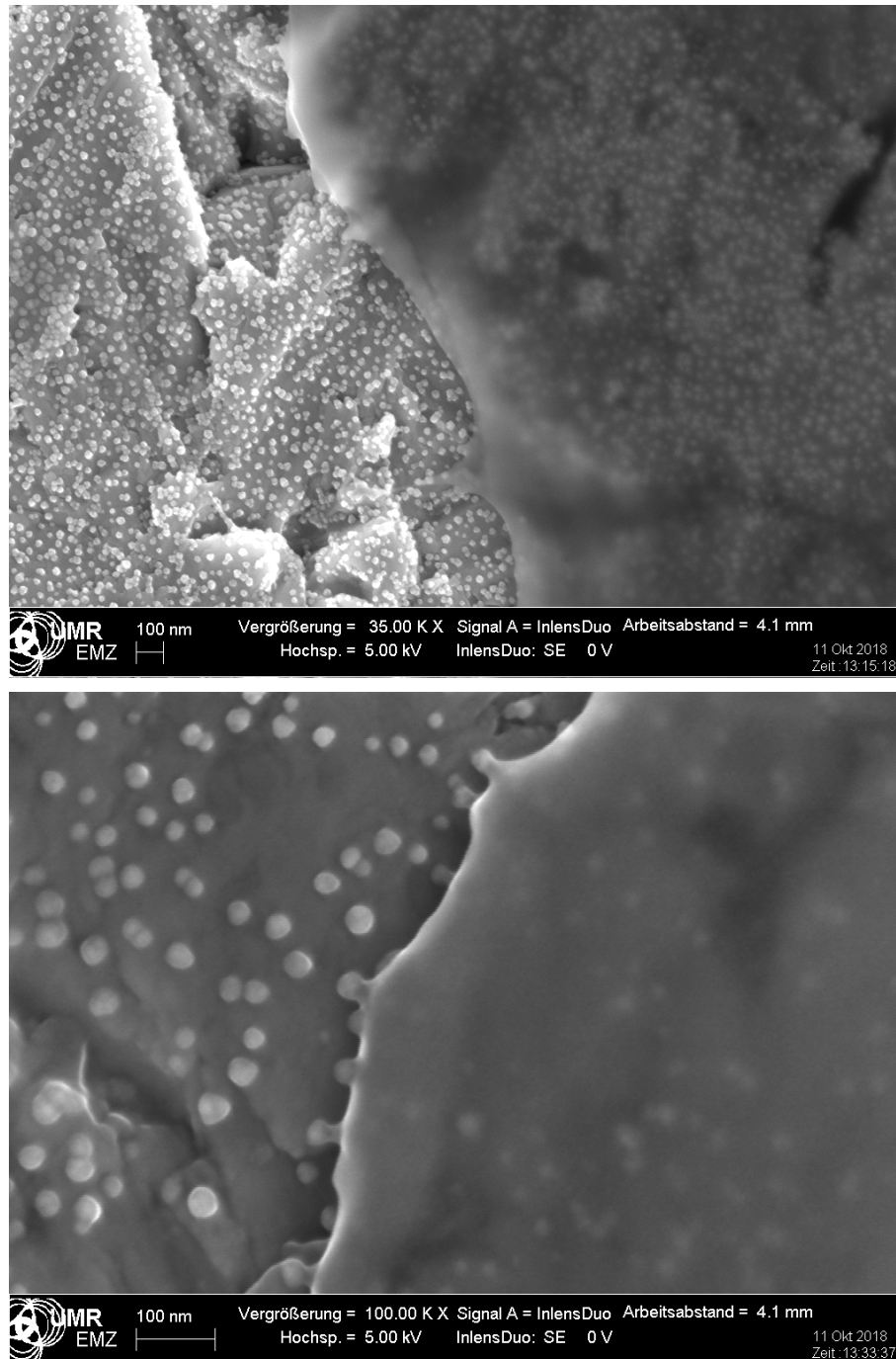


Figure 23: The SEM image shows a titanium surface with composite coating. Maghemite nanoflowers were applied by spray coating, followed by the application of a 1.0wt.-% PMMA solution in acetone by dip coating. The nanoflower diameter before coating is (28.7 ± 1.2) nm. The left part of both images shows an area that was not covered by the PMMA coating.

Discussion

This work investigates the polyol-assisted formation of maghemite nanoflowers over a wide range of synthesis conditions. X-ray diffraction studies reveal the presence of maghemite in tetragonal crystal structure with space group $P4_12_12$ for all samples examined. It has to be noted that despite the high resolution of the diffractograms, it is difficult to distinguish between this crystal structure and the cubic phases of maghemite and magnetite. The crystal structures of magnetite and cubic maghemite are closely related and have nearly the same lattice constant, with the presence of cation vacancies in maghemite being a distinguishing feature [29]. Rietveld refinements of the X-ray diffractograms assuming a cubic crystal structure delivered R_w values ranging from 4.7 % to 6.7 % for the individual samples. Using the tetragonal configuration for all refinements, significantly lower R_w values between 3.2 % and 4.1% were obtained. Indeed, the tetragonal space group is the energetically most stable configuration of maghemite, exhibiting complete vacancy ordering. At the synthesis temperature of 220°C, it occurs with a probability exceeding 99.9 % [53]. Additionally, Mössbauer spectra show a superposition of two sextets with hyperfine parameters characteristic of this structure [96, 97]. They were found to contain different contributions from core and surface regions, but no separate crystallographic phases could be detected by XRD. These results are identical for all samples, independent of the additional treatment with iron nitrate that all samples received except for samples B and C.

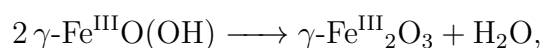
The nanoflower's size, shape and primary particle content are strongly influenced by a number of factors. Besides the iron precursor's stoichiometric parameter ζ , these include the precursor concentration, the type of polyol solvent and its mixing ratio with NMDEA, as well as the reaction temperature and time. Testing different synthesis temperatures and holding times provided an insight into the conditions necessary for nanoflower formation. Morphologic studies by transmission electron microscopy revealed the existence of superstructures with typical nanoflower morphology in samples B and C. Comparing the TEM images of the samples A and B, the superstructures are formed by aggregation of primary particles. The nanoflowers in sample B and C are polycrystalline with crystallite sizes corresponding to the size of primary particles comparing both particle and crystallite sizes.

Particle nucleation has scarcely begun after 2 h of thermal treatment at 180°C, as can be seen in the TEM images of sample A. Particles are globular and have a narrow size distribution. When applying the same target temperature over a longer period of time, these particles will both grow and aggregate to form nanoflowers as the TEM images of sample B indicate. Brownian motion causes the particle to shake, rotate and collide

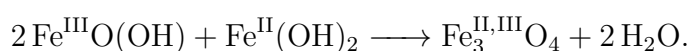
with each other during the aggregation process. This allows adjacent particles to reach a state of reduced surface free energy if their crystal lattices are aligned and form one defective single crystal [39]. However, the discrepancy between particle and crystallite size in sample B shows that such an alignment does not take place in this synthesis, or only to a limited extent. Instead, these nanoflowers can be regarded as polycrystalline superstructures containing single crystalline primary particles [37]. Sample C, on the other hand, has nearly identical mean particle size and crystallite size. A possible explanation for this is that a considerable fraction of primary particles in this sample is not aggregated. As a result, sample C contains a higher fraction of particles in a superparamagnetic state compared with sample B as indicated by the appearance of a doublet in Mössbauer spectra and smaller magnetic hyperfine fields. This reduction of the magnetic hyperfine field is different for each site, leading to a broader spectrum [116].

The time necessary for nanoflower formation can be shortened by increasing synthesis temperature. However, this has an impact on crystallite size and particle size. For sample C prepared with a target temperature of 220°C, a crystallite size of about 15 nm is already reached after a holding time of 2 h, compared to 12 h at 180°C. Nevertheless, particles are smaller overall. Therefore, 220°C and 2 h were chosen as target temperature and holding time for the following syntheses respectively due to the better time efficiency combined with a narrower particle size distribution.

The stoichiometric parameter ζ was found to be suitable for tuning the average particle size. It is important to emphasize that chemical and crystallographic composition does not change within the sample series, irrespective of the iron precursor's oxidation state. Both particle and crystallite sizes are rising for increasing ζ indicating stronger growth during synthesis. This can be explained by a reduction in the number of nucleation centres. Samples with lower ζ , i.e. smaller particles, have a higher synthesis yield as the iron concentration shows, which implies a stronger nucleation generating a higher yield despite the slower growth. Stronger growth is observed for growing ζ , yet the yield is lower pointing at weaker nucleation. During the polyol-assisted synthesis, a set of reactions takes place, leading to the formation of iron hydroxides and oxide-hydroxides [63]. Two reaction pathways are being discussed for the nucleation reaction [63]: Either, maghemite is formed by thermal decomposition of lepidocrocite (γ -Fe^{III}O(OH)),



or magnetite is formed in a condensation reaction between iron(III) oxide-hydroxide and iron(II) oxide and later oxidized to maghemite,



An indication for the latter being true is the observation that magnetite is formed if the reaction takes place under inert gas atmosphere [62]. Magnetite contains divalent and trivalent iron in a stoichiometric ratio 1:2, equivalent to $\zeta = 0.67$. Accordingly, the presence of both divalent and trivalent iron are required for nucleation. Varying

the stoichiometric ratio of the iron precursor should therefore alter the rates at which the intermediates involved in the nucleation reaction are formed. In a polyol based synthesis, solid particles are formed in a burst type nucleation [58]. This type of nucleation is characterized by the formation of a supersaturated solution of monomers. Following burst nucleation, the concentration of monomers drops below the nucleation barrier, inhibiting further nucleation [59]. Depending on the rate at which monomers are produced, nucleation may progress in a different way. This will also affect the adsorption of monomers during diffusive growth. At elevated temperature and in an environment containing oxygen, the trivalent form of iron will be prevailing. This is being counteracted by the reducing environment provided by polyol, which makes nucleation possible even when the initial stoichiometric parameter is $\zeta = 1$. By choosing an initial stoichiometry with lower ζ , a higher concentration of monomers should be reached prior to nucleation. The results of this work show that adding Fe^{2+} to the precursor solution indeed favours the nucleation process. It is therefore concluded that magnetite is formed in the nucleation reaction.

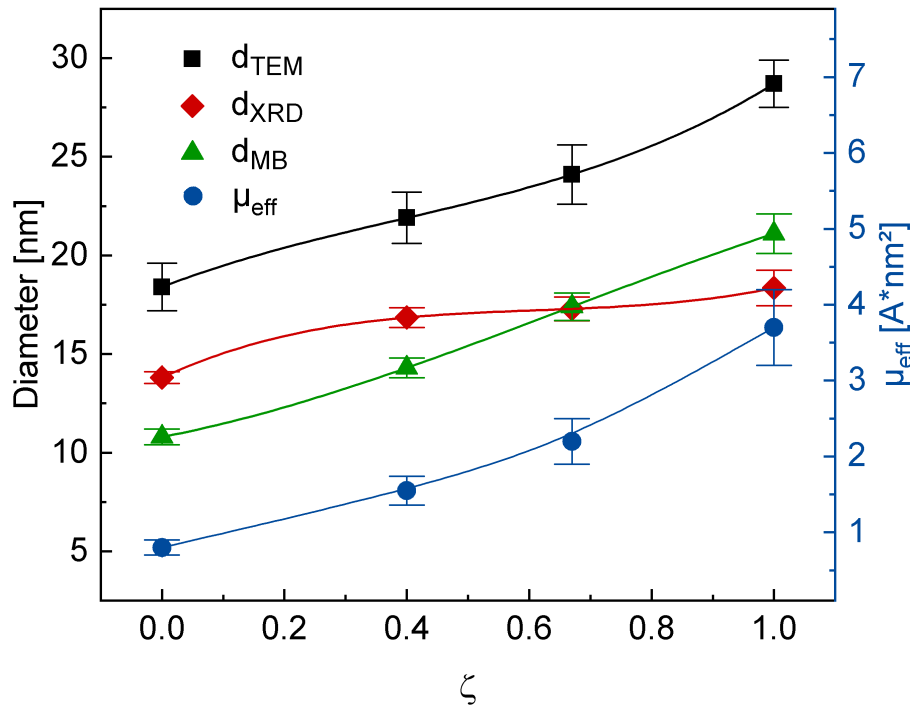


Figure 1: Particle sizes d_{TEM} , d_{MB} , crystallite sizes d_{XRD} and magnetic particle moments μ_{eff} for variable ζ . Data points are connected for better visualization.

The trend of increasing magnetic hyperfine fields with increasing ζ can be explained with increasing magnetic moments of the nanoflowers (see figure 1). As crystallite sizes are generally smaller than particle sizes, it can be assumed that nanoflowers are polycrystalline structures consisting of aggregated primary particles [37]. The increase of magnetic moments from $\zeta = 0$ to $\zeta = 1$ is related to particle size more than to

crystallite size, which shows only an insignificant increase between $\zeta = 0.4$ and $\zeta = 1$. In terms of superstructure formation, this means that for higher ζ , particles are bigger due to stronger aggregation-based growth - the contain more primary particles - rather than due to stronger diffusive growth of primary particles. Cooperative behaviour between primary particles within a nanoflower is more pronounced for bigger nanoflowers. This cooperative behaviour is controlled by magnetic dipole and exchange interactions [124]. A higher degree of interaction between primary particles suppresses superparamagnetic behaviour in favour of their superferrimagnetic character [33]. In the Mössbauer spectrum of the sample with $\zeta=0$, the onset of a transition towards superparamagnetic behaviour was observed. This shows that cooperative magnetic behaviour increases for samples with higher ζ , which also have bigger particle and crystallite sizes. The peak frequency of the imaginary part of the susceptibility rises towards $\zeta=0$. This is directly connected with shorter relaxation times.

| Particle type | Particle size [nm] | μ [$\text{A} \cdot \text{nm}^2$] | Source |
|----------------------------|--------------------|--|--------|
| Single-core maghemite NPs | 6 | 0.033 | [50] |
| Single-core maghemite NPs | 7 | 0.0556 | [125] |
| Spherical MNPs | 18.7 | 0.856 | [24] |
| Single-core iron oxide NPs | 35 | 3.1 | [34] |
| Maghemite nanoflowers | 21 | 1.936 | [50] |
| Maghemite nanoflowers | 22 | 1.792 | [50] |
| Maghemite nanoflowers | 24 | 2.891 | [50] |
| Maghemite nanoflowers | 28 | 4.59 | [50] |
| Maghemite nanoflowers | 34 | 6.615 | [50] |
| Maghemite nanoflowers | 39.0 | 3.5 | [37] |
| Maghemite nanoflowers | 42 | 13.04 | [50] |
| Multi-core iron oxide NPs | 69 | 6.5 | [34] |
| Multi-core iron oxide NPs | 97 | 11.9 | [34] |

Table 1: Overview over literature values for magnetic moments μ of different types of particles.

An overview over literature values for magnetic moments of single core and multi-core iron oxide nanoparticles is given in Table 1. As the comparison shows, the magnetic moments calculated in this work are within the range of literature values for particles similar in size. Therefore, the approximations made here appear realistic. For the smaller nanoflowers with $\zeta=0$, at a diameter of (18.4 ± 1.2) nm, there is no significant difference with spherical single-core particles of the same size. An enhanced magnetic moment can be observed in bigger nanoflowers with $\zeta=1$. At a particle size of (28.7 ± 1.2) nm, they reach nearly the same magnetic moment as single-core

particles with 35 nm diameter. From the observation that bigger nanoflowers contain more primary particles follows that their increased magnetic moments are a result of more primary particle's magnetic moments adding up to one large collective magnetic moment of the nanoflower. If the nanoflower size is further increased, even larger magnetic moments are possible, such as $13.04 \text{ A} \cdot \text{nm}^2$ for 42 nm particles [50]. This trend is visualized in figure 2.

The excellent dispersibility of the maghemite nanoflowers investigated in this work is another characteristic feature and is caused by their superferrimagnetic behaviour. As for maghemite single core particles, the transition from the superparamagnetic state to the blocked state around 10 nm particle diameter sets a size limit to dispersibility [118], although it is possible to improve dispersibility to some extent by surface modification. The spherical single core particles synthesized as part of this work are in a superparamagnetic size regime, exhibiting faster relaxation than nanoflowers, and possess magnetic moments ranging from $(0.022 \pm 0.011) \text{ A} \cdot \text{nm}^2$ to $(0.31 \pm 0.10) \text{ A} \cdot \text{nm}^2$, which are typical values for particles of this size as found in literature. This result underlines the enhanced magnetic properties of nanoflowers, featuring magnetic moments that are one order of magnitude larger than those of single core particles.

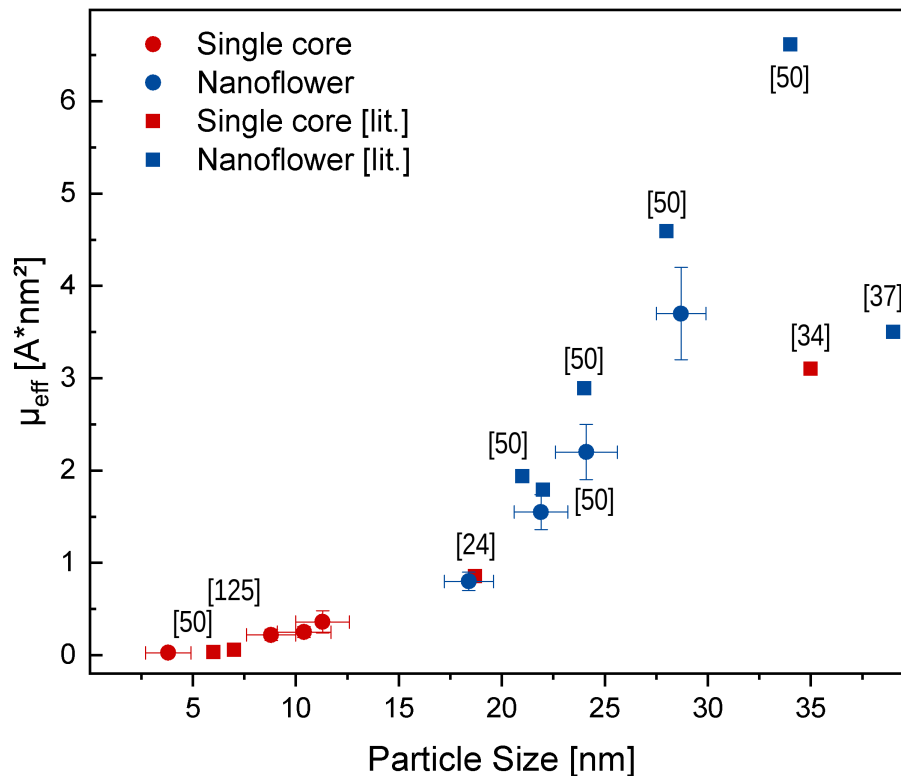


Figure 2: Magnetic particle moments μ_{eff} plotted in dependence of the particle size for iron oxide single core particles and nanoflowers, including both the results from this work as well as literature values. References are given in brackets.

Maghemite nanoflowers were successfully incorporated in a PMMA composite coating after a series of tests. Using a glass surface as a model, the influence of the PMMA concentration in acetone on the dip coating process was investigated. The AFM measurements show that by decreasing the PMMA concentration, thinner layers can be achieved. However, a limit is found at around 100 nm coating thickness, where the coating homogeneity deteriorates. By introducing a second dip coating application, this minimum achievable thickness can be cut in half. Among the samples prepared in this work, applying twice a 0.25 wt.-% PMMA solution represents the most suitable parameters for a thin and smooth coating, obtaining a (46 ± 7) nm thick layer with 11.9% relative roughness.

The investigation of composite coatings on Titanium by SEM showed different results compared with results obtained by AFM using glass substrate. While two applications of PMMA solutions with 0.25 wt.-% concentration and less showed large holes in the coating, no major holes were found by AFM on glass substrate for concentrations higher than 0.15 wt.-% following the same coating procedure. Two different possible explanations for this need to be considered. Firstly, different substrates were used, meaning that titanium and glass are not identical with respect to hydrophilic or hydrophobic properties. Also, the glass substrate has a very smooth surface with very low roughness. The same is not true for the titanium substrate used in this work. SEM images clearly show the existence of roughness on the observable scale. Substrate roughness strongly impacts wettability [113, 126] which will impact the adhesion of the polymer and thereby change layer thickness and morphology:

$$\cos \theta_R = W_R \cos \theta_0,$$

with θ_R and θ_0 being the contact angles of droplets on rough and smooth surfaces, respectively, and W_R being the ratio between the true surface area and its two-dimensional projection, called roughness area ratio [127]. The contact angle is a measure of wettability, indicating wettability at angles between 0° and 90° and indicating non-wettability at angles larger than 90° . As a result of the relation described above, increasing surface roughness will increase wettability or non-wettability. Secondly, differences in the investigation methods need to be taken into account. Both SEM and AFM images may show artefacts characteristic of each method. In particular, small holes in the surface can be hidden on AFM images due to artefacts caused by the tip geometry. Features on the sample surface with a radius smaller than twice the tip curvature radius can be expected to be displayed inaccurately [112]. AFM scans were conducted using a tip with nominally 10 nm curvature radius, meaning that all features with a radius larger than 20 nm will be displayed correctly. The curvature radius R_f of a feature can be estimated using a truncated sphere model as

$$R_f = \frac{h^2 + (\frac{w}{2})^2}{2h},$$

where h is its height and w its full width [112]. On the SEM images of the samples in question, holes with diameters well in excess of 100 nm are visible. Assuming a hole

with height $h = 50$ nm and width $w = 100$ nm, $R = 50$ nm is obtained. Therefore, the differences in surface coverage observed between AFM and SEM images are clearly not due to artefacts.

The same is not true for holes with sizes closer to the tip radius, putting a limit to the characterization of coating homogeneity by AFM. The RMS roughness was discussed relative to the layer thickness as a means of describing this coating homogeneity quantitatively. This appears to be a viable approach, given that artefacts caused by finite tip radius have only little influence on vertical roughness measurements [114]. The strong increase in relative roughness for thinner coatings is possibly caused by the development of holes in the coating rather than by the roughness of the PMMA layer itself, as visible when comparing these values to the appearance of AFM topography scans.

The most homogeneous coating on glass substrate with a suitable thickness of (46 ± 7) nm exhibits 5.5 nm RMS roughness. Using the spin coating method, thinner and smoother surfaces are achievable, reaching a film thickness around 10 nm to 20 nm at about 2 nm roughness [119]. In the context of this work, the results obtained here appear sufficient. Surface roughness of a homogeneous film is not necessarily a disadvantage, as it can be conducive to osseointegration [5].

The tendency to form agglomerates is a major obstacle when trying to evenly disperse suspended nanoscale particles on a solid surface while maintaining their nanostructure. The samples prepared in this work illustrate the importance of withdrawing the dispersion medium in such a way that particles are immobilized before agglomeration can set in. This was realized with the spray coating technique which allows the application of small amounts of suspension in a controlled manner. The method shows excellent results in conjunction with highly stable suspensions of magnetic nanoflowers as obtained by the polyol-assisted synthesis. The stability of the suspension is another crucial factor, as preliminary tests conducted with magnetic iron oxide nanoparticles obtained by a simple coprecipitation method failed to deliver comparable results.

Conclusions

One of the most fundamental requirements for the application of iron oxide nanoparticles in biomedicine is that particles and their agglomerates have no tendency to grow beyond a critical size of approximately 5 μm which is harmful for blood flow [128]. Therefore, it is important to note that all samples prepared in this work are easily dispersible. Three samples were produced varying the target temperature and holding time for the thermal synthesis of maghemite nanoflowers via the polyol route. It was found that after the nucleation and growth of globular primary particles, aggregation takes place in a second step which leads to the formation of nanoflowers. A target temperature of 220°C and a holding time of 2 h were confirmed as suitable parameters for thermal treatment yielding a narrow particle size distribution. Highly stable, aqueous nanoflower suspensions were obtained. All samples were found to be composed purely of maghemite ($\gamma\text{-Fe}_2\text{O}_3$) in tetragonal structure. A consistent formation of nanoflowers for all iron precursor stoichiometries was observed. It was successfully achieved to influence both the particle and crystallite sizes by varying the precursor stoichiometry. Average particle sizes changed in an interval from (18.4 ± 1.2) nm to (28.7 ± 1.2) nm. Crystallite sizes are slightly smaller and range from (13.8 ± 0.3) nm to (18.4 ± 0.9) nm. Particle diameters estimated from Mössbauer spectra range from (10.8 ± 0.4) nm to (21.1 ± 1.0) nm. The increasing particle size and the rising magnetic hyperfine fields show that the particles' magnetic moments increased. It was found that mixtures which contain a larger proportion of Fe^{3+} ions led to larger particles and crystallites, while a higher content in Fe^{2+} ions favoured nucleation at the expense of growth. The additional treatment with iron nitrate led to further growth in crystallite and particle size, however no additional surface layer with a different chemical or crystallographic composition was found. An increase in Brownian relaxation times from approximately 0.2 μs to 9 μs and an increase in both static and dynamic susceptibilities with increasing particle size were observed. The dynamic susceptibilities and magnetic moments were compared with those of superparamagnetic single-core particles to illustrate the enhanced magnetic properties of superferrimagnetic nanoflowers due to collective behaviour. It was shown that in the polyol based synthesis of maghemite nanoflowers, the iron precursor stoichiometry can be exploited to tune structural properties such as particle and crystallite size. These strongly impact the particles' magnetic properties and relaxation behaviour offering the opportunity to use and optimize them for applications in biomedicine such as magnetic hyperthermia treatment or magnetic particle imaging.

For the application as a bioactive coating on a bone implant, the relaxation time τ and particle's magnetic moments μ are key parameters. For a coating system that

relies exclusively on the relaxation of particles and uses no external drive field, the nanoflower sample with $\zeta = 0.0$ appears most promising, containing the smallest particles with the shortest relaxation times. As detailed previously, the achievable electric field induced by a magnetic nanoparticle at the distance r from the particle's centre is estimated as

$$E_{\text{eff}} = \frac{\mu_0 \cdot \mu}{2\sqrt{2}\pi r^2}.$$

The effective value of the electric field is proportional to the particle's magnetic moment and inversely proportional to the relaxation time. Consequently, reducing relaxation times has a stronger impact on the achievable electric field than increasing magnetic moments. Only considering this aspect, smaller superparamagnetic single-core particles might be a more promising choice. However, the effective magnetic field is independent of relaxation time,

$$B_{\text{eff}} = \frac{\mu_0 \mu}{2\sqrt{2}\pi r^3}.$$

To maximize this parameter, magnetic moments need to be maximized. This is possible using large nanoflowers. The question of finding a suitable compromise between the effective electric and magnetic field to provide an optimal stimulus for bone regeneration extends far beyond the scope of this work. The same is the case for other stimulation parameters such as frequency and duration of application. External inductive coupling stimulation devices provide electric fields of 1 mV/cm to 100 mV/cm and magnetic fields of 0.01 mT to 2 mT [21]. The composite coating presented here reaches a similar electric field only for relaxation times or drive frequencies in the high-frequency regime. The magnetic field, however, exceeds these values by one or two orders of magnitude in the vicinity of a particle. Accordingly, a biologic cell, being larger than a magnetic nanoparticle by a few orders of magnitude, will receive strong local electromagnetic stimuli from a few hundred nanoparticles. This approach is substantially different from known macroscopic stimulation devices and thus presents an interesting new starting point for biomedical research.

In contrast to this, if the switching of magnetic dipoles of the particles was triggered by an external drive field, a uniform electromagnetic stimulus would be generated throughout the implant surface, provided that a suitable distribution of particles is realized. In this case, the field frequency is given by the external field. Therefore, the particle's magnetic moments are important to maximize the effect. Among the samples prepared in this work, the largest magnetic moment was found in the nanoflower sample with $\zeta = 1.0$, being $(3.2 \pm 0.4) \text{ A} \cdot \text{nm}^2$.

By performing dip coatings with solutions of PMMA in acetone, an efficient testing environment was used to obtain an overview over achievable film thicknesses and to assess homogeneity. It was successfully demonstrated that two subsequent applications of the dip coating lead to the formation of an even film with no significant deviation in thickness. A suitable starting parameter was found for two applications of 0.25 wt.-%

PMMA, achieving an average coating thickness of (46 ± 7) nm with 5.5 nm surface roughness.

The application of magnetic nanoparticles to titanium surfaces while maintaining an even particle distribution and avoiding agglomeration was found to be hard to achieve. A spray coating method was successfully adapted for this purpose. Highly stable suspensions of iron oxide nanoflowers, as obtained by polyol synthesis route investigated in this work, are ideally suited for spray coating. For implementing this method in industrial scale applications, the airbrush nozzle can be easily mounted on a robotic arm, thereby ensuring highly reproducible results and an even application on the complex surface of titanium-based bone implants. By varying the spraying duration, the particle density can be tuned.

A layer of PMMA was applied on top of the nanoflowers without altering their distribution on the titanium substrate. The formation of holes was avoided by increasing the PMMA concentration up to 0.5 wt.-%, where homogeneous surface layers were observed. An homogeneous PMMA composite coating containing evenly distributed maghemite nanoflowers was successfully developed, allowing further development for applications in bioactive bone implants.

Outlook

It was shown in this work that the nucleation and growth of maghemite nanoflowers in a polyol-assisted synthesis routine can be influenced by varying the precursor stoichiometry. Even though a consistent interpretation of the results of this work was found, further characterization would be helpful to verify the assumption of a nucleation reaction involving magnetite. To achieve this, additional measurements should be conducted on samples taken at certain time intervals during synthesis. Spectroscopic methods, such as infrared spectroscopy, could prove very useful in this context, as well as additional X-ray diffraction measurements. Developing a complete picture of all chemical and crystallographic processes involved in nanoflower formation will open up new possibilities for optimizing their magnetic properties. In particular, the influence of nanoflower size and primary particle size on the effective magnetic moment should be further studied. It has been suggested that the effective magnetic moment of a nanoflower will increase more for bigger nanoflowers if growth is realized by a higher degree of agglomeration rather than by increasing primary particle size [35]. Accordingly, increasing nanoflower size while decreasing primary particle size will maximize effective magnetic moments. To achieve this in a controlled way, it is necessary to selectively influence the diffusional growth and the aggregation-based growth of nanoflowers. Intimate knowledge of the processes involved in nanoflower formation therefore allows to further enhance their magnetic properties.

With respect to the application of magnetic nanoparticles to an implant surface via spray coating, it is desirable to systematically adjust local particle density. This can only be achieved reliably by an automated spray coating device which could be constructed by mounting an airbrush on a robotic arm. Then, the relationship between parameters of the spraying application and the particle distribution needs to be calibrated. For a given particle distribution, local electromagnetic fields should be calculated in a simulation, similarly to studies on electric stimulation devices [19].

Magnetic force microscopy is a suitable tool to quantify achievable magnetic fields on the surface of the coating experimentally. In this technique, an atomic force microscope is operated with a magnetized tip. A mapping of local magnetic fields could prove helpful in the process of optimizing the distribution of particles on the implant surface. Some attempts at calibrating magnetic tips for a quantitative measurement of the interaction with magnetic particles have been made [24], however this is by no means a trivial issue.

Eventually, the effectiveness of the coating system presented in this work should be examined in cell tests. A variety of configurations is possible: letting particles freely change their magnetic moment's orientation due to relaxation, triggering these orientation changes by an external inductive coupling-based stimulation device, or deactivating the particles using a strong static magnetic field. There is a considerable qualitative difference to existing setups, in particular without the use of an external stimulation device. In this case, thermal fluctuations in magnetic nanoparticles permanently cause strong local electromagnetic fields. It yet needs to be understood in which way these fields interact with cells and tissues. Further research is needed to understand the biomedical implications connected with this concept of a substantially novel implant system.

Appendix

1 Magnified TEM image

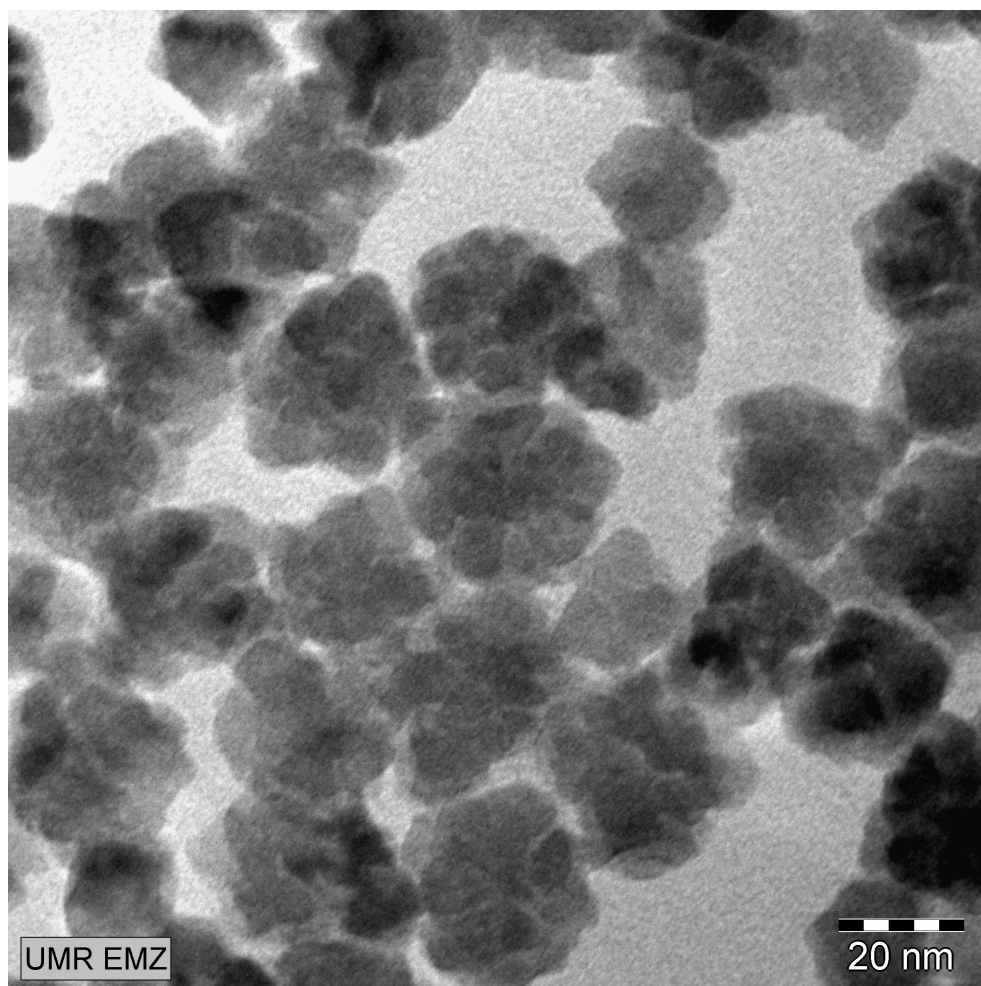


Figure 1: TEM image for the nanoflower sample prepared with stoichiometric parameter $\zeta = 1$.

2 Mössbauer fit parameters

| Sample B | | | | | |
|----------------|-------------------------------------|-------------------------------------|---------------------------|---------------------------------------|---------------|
| Site | IS [$\frac{\text{mm}}{\text{s}}$] | QS [$\frac{\text{mm}}{\text{s}}$] | $\mu_0 H_{\text{hf}}$ [T] | FWHM [$\frac{\text{mm}}{\text{s}}$] | Rel. int. [%] |
| A _b | 0.326 ± 0.002 | -0.007 ± 0.002 | 47.3 ± 0.1 | 0.288 ± 0.005 | 46.1 |
| B _b | 0.352 ± 0.004 | -0.017 ± 0.004 | 45.1 ± 0.1 | 0.326 ± 0.011 | 30.9 |
| A _s | 0.401 ± 0.007 | -0.001 ± 0.006 | 41.9 ± 0.1 | 0.337 ± 0.020 | 15.2 |
| B _s | 0.434 ± 0.011 | -0.01 ± 0.01 | 38.1 ± 0.2 | 0.328 ± 0.024 | 7.7 |
| Sample C | | | | | |
| Site | IS [$\frac{\text{mm}}{\text{s}}$] | QS [$\frac{\text{mm}}{\text{s}}$] | $\mu_0 H_{\text{hf}}$ [T] | FWHM [$\frac{\text{mm}}{\text{s}}$] | Rel. int. [%] |
| A _b | 0.330 ± 0.011 | -0.01 ± 0.01 | 44.9 ± 0.2 | 0.47 ± 0.04 | 19.4 |
| B _b | 0.313 ± 0.016 | -0.010 ± 0.015 | 40.1 ± 0.5 | 0.87 ± 0.09 | 38.6 |
| A _s | 0.38 ± 0.07 | 0.00 ± 0.06 | 33.0 ± 0.8 | 0.98 ± 0.24 | 23.0 |
| B _s | 0.34 ± 0.09 | 0.06 ± 0.06 | 18.3 ± 0.9 | 1.20 ± 0.60 | 17.9 |
| Doublet | 0.48 ± 0.08 | 1.49 ± 0.17 | - | 0.36 ± 0.18 | 1.1 |

Table 1: Hyperfine parameters of all contributing subspectra with bulk and surface contributions for A- and B-sites for samples B, C. One sample was fitted with an additional doublet.

| $\zeta = 1.0$ | | | | | |
|----------------|-------------------------------------|-------------------------------------|---------------------------|---------------------------------------|---------------|
| Site | IS [$\frac{\text{mm}}{\text{s}}$] | QS [$\frac{\text{mm}}{\text{s}}$] | $\mu_0 H_{\text{hf}}$ [T] | FWHM [$\frac{\text{mm}}{\text{s}}$] | Rel. int. [%] |
| A _b | 0.324 ± 0.003 | 0.006 ± 0.002 | 47.8 ± 0.1 | 0.241 ± 0.005 | 41.5 |
| B _b | 0.329 ± 0.004 | 0.002 ± 0.002 | 46.1 ± 0.1 | 0.280 ± 0.011 | 34.7 |
| A _s | 0.361 ± 0.013 | -0.003 ± 0.002 | 43.2 ± 0.2 | 0.343 ± 0.012 | 16.8 |
| B _s | 0.445 ± 0.016 | -0.006 ± 0.004 | 39.2 ± 0.3 | 0.352 ± 0.014 | 7.0 |
| $\zeta = 0.67$ | | | | | |
| Site | IS [$\frac{\text{mm}}{\text{s}}$] | QS [$\frac{\text{mm}}{\text{s}}$] | $\mu_0 H_{\text{hf}}$ [T] | FWHM [$\frac{\text{mm}}{\text{s}}$] | Rel. int. [%] |
| A _b | 0.325 ± 0.008 | 0.002 ± 0.002 | 47.0 ± 0.2 | 0.297 ± 0.014 | 38.4 |
| B _b | 0.327 ± 0.009 | 0.001 ± 0.001 | 44.9 ± 0.2 | 0.366 ± 0.011 | 33.6 |
| A _s | 0.344 ± 0.022 | -0.002 ± 0.002 | 40.9 ± 0.3 | 0.54 ± 0.04 | 20.8 |
| B _s | 0.463 ± 0.028 | -0.003 ± 0.003 | 36.8 ± 0.3 | 0.55 ± 0.08 | 7.2 |
| $\zeta = 0.4$ | | | | | |
| Site | IS [$\frac{\text{mm}}{\text{s}}$] | QS [$\frac{\text{mm}}{\text{s}}$] | $\mu_0 H_{\text{hf}}$ [T] | FWHM [$\frac{\text{mm}}{\text{s}}$] | Rel. int. [%] |
| A _b | 0.317 ± 0.008 | 0.002 ± 0.002 | 46.7 ± 0.1 | 0.301 ± 0.008 | 39.5 |
| B _b | 0.319 ± 0.015 | -0.004 ± 0.002 | 44.4 ± 0.3 | 0.370 ± 0.014 | 25.5 |
| A _s | 0.341 ± 0.022 | -0.007 ± 0.004 | 41.0 ± 0.4 | 0.519 ± 0.026 | 25.7 |
| B _s | 0.46 ± 0.03 | -0.008 ± 0.004 | 35.9 ± 0.5 | 0.55 ± 0.08 | 9.3 |
| $\zeta = 0.0$ | | | | | |
| Site | IS [$\frac{\text{mm}}{\text{s}}$] | QS [$\frac{\text{mm}}{\text{s}}$] | $\mu_0 H_{\text{hf}}$ [T] | FWHM [$\frac{\text{mm}}{\text{s}}$] | Rel. int. [%] |
| A _b | 0.311 ± 0.013 | -0.004 ± 0.002 | 44.6 ± 0.2 | 0.446 ± 0.021 | 23.4 |
| B _b | 0.319 ± 0.015 | -0.008 ± 0.002 | 41.2 ± 0.4 | 0.53 ± 0.04 | 24.4 |
| A _s | 0.358 ± 0.025 | -0.008 ± 0.003 | 36.3 ± 0.4 | 0.82 ± 0.06 | 33.0 |
| B _s | 0.44 ± 0.04 | -0.012 ± 0.004 | 26.9 ± 0.9 | 0.92 ± 0.12 | 13.6 |
| Doublet | 0.41 ± 0.04 | 2.38 ± 0.12 | - | 0.9 ± 0.1 | 5.6 |

Table 2: Hyperfine parameters of all contributing subspectra with bulk and surface contributions for A- and B-sites for samples $\zeta=1.0$; 0.67; 0.4; 0.0. One sample was fitted with an additional doublet.

Bibliography

- [1] Fallpauschalenbezogene Krankenhausstatistik (DRG-Statistik) - Operationen und Prozeduren der vollstationären Patientinnen und Patienten in Krankenhäusern (4-Steller). www.destatis.de/DE/Publikationen/Thematisch/Gesundheit/Krankenhaeuser/OperationenProzeduren.html, 2010-2017. [Online; accessed 29-January-2019].
- [2] R. Gradinger and H. Gollwitzer. *Ossäre Integration*. Springer, 2006.
- [3] A. S. Brydone, D. Meek, and S. Maclaine. Bone grafting, orthopaedic biomaterials, and the clinical need for bone engineering. *Proceedings of the Institution of Mechanical Engineers, Part H: Journal of Engineering in Medicine*, 224(12):1329–1343, 2010.
- [4] S. Arens and M. Hansis. Implantate in der Unfallchirurgie: Osteosynthese mit Titan. *Deutsches Ärzteblatt International*, 95(24):A1516–A1518, 1998.
- [5] R. Agarwal and A. J. García. Biomaterial strategies for engineering implants for enhanced osseointegration and bone repair. *Advanced drug delivery reviews*, 94:53–62, 2015.
- [6] A. Chug, S. Shukla, L. Mahesh, and S. Jadwani. Osseointegration - molecular events at the bone-implant interface: A review. *Journal of Oral and Maxillofacial Surgery, Medicine, and Pathology*, 25(1):1–4, 2013.
- [7] Y. Li, C. Yang, H. Zhao, S. Qu, X. Li, and Y. Li. New developments of Ti-based alloys for biomedical applications. *Materials*, 7(3):1709–1800, 2014.
- [8] R. Nicula, F. Lüthen, M. Stir, B. Nebe, and E. Burkel. Spark plasma sintering synthesis of porous nanocrystalline titanium alloys for biomedical applications. *Biomolecular engineering*, 24(5):564–567, 2007.
- [9] F. Zhang, E. Otterstein, and E. Burkel. Spark plasma sintering, microstructures, and mechanical properties of macroporous titanium foams. *Advanced Engineering Materials*, 12(9):863–872, 2010.
- [10] Y. Quan, F. Zhang, H. Rebl, B. Nebe, O. Keßler, and E. Burkel. Ti₆Al₄V foams fabricated by spark plasma sintering with post-heat treatment. *Materials Science and Engineering: A*, 565:118–125, 2013.
- [11] J. Wolff. Über die innere Architectur der Knochen und ihre Bedeutung für die Frage vom Knochenwachstum. *Virchows Archiv für pathologische Anatomie und*

- Physiologie und für klinische Medicin*, 50:389 – 450, 1870.
- [12] E. Fukada and I. Yasuda. On the piezoelectric effect of bone. *Journal of the physical society of Japan*, 12(10):1158–1162, 1957.
- [13] A. C. Ahn and A. J. Grodzinsky. Relevance of collagen piezoelectricity to "Wolff's Law": a critical review. *Medical engineering & physics*, 31(7):733–741, 2009.
- [14] C. A. L. Bassett, R. J. Pawluk, and R. O. Becker. Effects of electric currents on bone in vivo. *Nature*, 204(4959):652, 1964.
- [15] C. A. L. Bassett, S. N. Mitchell, and S. R. Gaston. Pulsing electromagnetic field treatment in ununited fractures and failed arthrodeses. *Jama*, 247(5):623–628, 1982.
- [16] R. B. Simonis, E. J. Parnell, P. S. Ray, and J. L. Peacock. Electrical treatment of tibial non-union: a prospective, randomised, double-blind trial. *Injury*, 34(5):357–362, 2003.
- [17] S. Meng, M. Rouabhia, and Z. Zhang. Electrical stimulation in tissue regeneration. In *Applied Biomedical Engineering*. InTech, 2011.
- [18] B. Hiemer, J. Ziebart, A. Jonitz-Heincke, P. C. Grunert, Y. Su, D. Hansmann, and R. Bader. Magnetically induced electrostimulation of human osteoblasts results in enhanced cell viability and osteogenic differentiation. *International journal of molecular medicine*, 38(1):57–64, 2016.
- [19] T.J. Dauben, J. Ziebart, T. Bender, S. Zaatreh, B. Kreikemeyer, and R. Bader. A novel in vitro system for comparative analyses of bone cells and bacteria under electrical stimulation. *BioMed research international*, 2016, 2016.
- [20] R. K. Aaron, D. McK. Ciombor, and B. J. Simon. Treatment of nonunions with electric and electromagnetic fields. *Clinical Orthopaedics and Related Research*, 419:21–29, 2004.
- [21] G. Victoria, B. Petrisor, B. Drew, and D. Dick. Bone stimulation for fracture healing: What's all the fuss? *Indian journal of orthopaedics*, 43(2):117, 2009.
- [22] M. Griffin and A. Bayat. Electrical stimulation in bone healing: critical analysis by evaluating levels of evidence. *Eplasty*, 11, 2011.
- [23] K. Witte, C. Grüttner, W. Bodnar, and E. Burkel. Magnetic nanoparticles for biomedical applications. In B. Bhushan, editor, *Encyclopedia of Nanotechnology*, pages 1–9. Springer, 2014.
- [24] S. Sievers, K. F. Braun, D. Eberbeck, S. Gustafsson, E. Olsson, H. W. Schumacher, and U. Siegner. Quantitative measurement of the magnetic moment of individual magnetic nanoparticles by magnetic force microscopy. *Small*, 8(17):2675–2679, 2012.

- [25] N.W. Ashcroft and D.N. Mermin. *Festkörperphysik*. Oldenbourg Verlag, 4 edition, 2013.
- [26] A. S. Teja and P.-Y. Koh. Synthesis, properties, and applications of magnetic iron oxide nanoparticles, 2009.
- [27] A. H. Lu, E. L. Salabas, and F. Schüth. Magnetic nanoparticles: synthesis, protection, functionalization, and application. *Angewandte Chemie International Edition*, 46(8):1222–1244, 2007.
- [28] X. Batlle and A. Labarta. Finite-size effects in fine particles: magnetic and transport properties. *Journal of Physics D: Applied Physics*, 35(6):R15–R42, 2002.
- [29] R. M. Cornell and U. Schwertmann. *The iron oxides: structure, properties, reactions, occurrences and uses*. Wiley-VCH Verlag, 2003.
- [30] Louis Néel. Théorie du traînage magnétique des ferromagnétiques en grains fins avec applications aux terres cuites. *Annales de Géophysique*, 5:99–136, 1949.
- [31] William Fuller Brown Jr. Thermal fluctuations of a single-domain particle. *Physical Review*, 130(5):1677, 1963.
- [32] P.C. Fannin and S.W. Charles. The study of a ferrofluid exhibiting both brownian and neel relaxation. *Journal of Physics D: Applied Physics*, 22(1):187, 1989.
- [33] S. Mørup. Superferromagnetic nanostructures. *Hyperfine Interactions*, 90(1):171–185, 1994.
- [34] F. Ahrentorp, A. Astalan, J. Blomgren, C. Jonasson, E. Wetterskog, P. Svedlindh, A. Lak, F. Ludwig, L. J. Van IJzendoorn, F. Westphal, C. Grüttner, N. Gehrke, S. Gustafsson, E. Olsson, and C. Johansson. Effective particle magnetic moment of multi-core particles. *Journal of Magnetism and Magnetic Materials*, 380:221–226, 2015.
- [35] V. Schaller, G. Wahnström, A. Sanz-Velasco, S. Gustafsson, E. Olsson, P. Enoksson, and C. Johansson. Effective magnetic moment of magnetic multicore nanoparticles. *Physical Review B*, 80(9):092406, 2009.
- [36] V. Schaller, G. Wahnström, A. Sanz-Velasco, P. Enoksson, and C. Johansson. Monte carlo simulation of magnetic multi-core nanoparticles. *Journal of Magnetism and Magnetic Materials*, 321(10):1400–1403, 2009.
- [37] P. Bender, J. Fock, C. Frandsen, M.F. Hansen, C. Balceris, F. Ludwig, O. Posth, E. Wetterskog, L. K. Bogart, P. Southern, W. Szczerba, L. Zeng, K. Witte, C. Grüttner, F. Westphal, D. Honecker, D. González-Alonso, L. Fernández Barquín, and C. Johansson. Relating magnetic properties and high hyperthermia performance of iron oxide nanoflowers. *The Journal of Physical Chemistry C*, 122(5):3068–3077, 2018.

- [38] B. I. Kharisov. A review for synthesis of nanoflowers. *Recent patents on nanotechnology*, 2(3):190–200, 2008.
- [39] J. F. Banfield, S. A. Welch, H. Zhang, T. T. Ebert, R. Penn, and R. Lee. Aggregation-based crystal growth and microstructure development in natural iron oxyhydroxide biomineralization products. *Science*, 289(5480):751–754, 2000.
- [40] L. Lartigue, P. Hugounenq, D. Alloyeau, S. P. Clarke, M. Lévy, J. C. Bacri, R. Bazzi, D. F. Brougham, C. Wilhelm, and F. Gazeau. Cooperative organization in iron oxide multi-core nanoparticles potentiates their efficiency as heating mediators and MRI contrast agents. *ACS nano*, 6(12):10935–10949, 2012.
- [41] H. Gavilán, A. Kowalski, D. Heinke, A. Sugunan, J. Sommertune, M. Varón, L. K. Bogart, O. Posth, L. Zeng, D. González-Alonso, C. Balceris, J. Fock, E. Wetterskog, C. Frandsen, N. Gehrke, C. Grüttner, A. Fornara, F. Ludwig, S. Veintemillas-Verdaguer, C. Johansson, and M. Puerto Morales. Colloidal flower-shaped iron oxide nanoparticles: Synthesis strategies and coatings. *Particle & Particle Systems Characterization*, 34(7):1700094, 2017.
- [42] S. Dutz. Are magnetic multicore nanoparticles promising candidates for biomedical applications? *IEEE Transactions on Magnetics*, 52(9):1–3, 2016.
- [43] J. Ge, Y. Hu, M. Biasini, W.P. Beyermann, and Y. Yin. Superparamagnetic magnetite colloidal nanocrystal clusters. *Angewandte Chemie International Edition*, 46(23):4342–4345, 2007.
- [44] P. Tartaj, M. del Puerto Morales, S. Veintemillas-Verdaguer, T. González-Carreño, and C. J. Serna. Topical review: The preparation of magnetic nanoparticles for applications in biomedicine. *Journal of Physics D: Applied Physics*, 36:R182–R197, 2003.
- [45] Q.A. Pankhurst, J. Connolly, S.K. Jones, and J.J. Dobson. Applications of magnetic nanoparticles in biomedicine. *Journal of physics D: Applied physics*, 36(13):R167–R181, 2003.
- [46] Q. A. Pankhurst, N. T. K. Thanh, S. K. Jones, and J. Dobson. Progress in applications of magnetic nanoparticles in biomedicine. *Journal of Physics D: Applied Physics*, 42(22):224001, 2009.
- [47] A. J. Giustini, A. A. Petryk, S. M. Cassim, J. A. Tate, and P. J. Hoopes I. Baker. Magnetic nanoparticle hyperthermia in cancer treatment. *Nano Life*, 1(01n02):17–32, 2010.
- [48] B. Gleich and J. Weizenecker. Tomographic imaging using the nonlinear response of magnetic particles. *Nature*, 435(7046):1214, 2005.
- [49] R. M. Ferguson, K. R. Minard, and K. M. Krishnan. Optimization of nanoparticle core size for magnetic particle imaging. *Journal of magnetism and magnetic materials*, 321(10):1548–1551, 2009.

- [50] P. Hugounenq, M. Levy, D. Alloyeau, L. Lartigue, E. Dubois, V. Cabuil, C. Ricolleau, S. Roux, C. Wilhelm, and F. Gazeau. Iron oxide monocrystalline nanoflowers for highly efficient magnetic hyperthermia. *The Journal of Physical Chemistry C*, 116(29):15702–15712, 2012.
- [51] M. Levy, N. Luciani, D. Alloyeau, D. Elgrabli, V. Deveaux, C. Pechoux, S. Chat, G. Wang, N. Vats, F. Gendron, C. Factor, S. Lotersztajn, A. Luciani, C. Wilhelm, and F. Gazeau. Long term in vivo biotransformation of iron oxide nanoparticles. *Biomaterials*, 32(16):3988–3999, 2011.
- [52] K. Witte, K. Porath, and E. Burkel. Magnetic nanoparticles and their potential for contrast enhancement in magnetic resonance imaging. *Journal of Spintronics and Magnetic Nanomaterials*, 1(1):40–46, 2012.
- [53] R. Grau-Crespo, A.Y. Al-Baitai, I. Saadoun, and N.H. De Leeuw. Vacancy ordering and electronic structure of γ -Fe₂O₃ (maghemite): a theoretical investigation. *Journal of Physics: Condensed Matter*, 22(25):255401, 2010.
- [54] A. N. Shmakov, G. N. Kryukova, S. V. Tsybulya, A. L. Chuvilin, and L. P. Solovyeva. Vacancy ordering in γ -Fe₂O₃: Synchrotron x-ray powder diffraction and high-resolution electron microscopy studies. *Journal of Applied Crystallography*, 28:141–145, 1995.
- [55] J. E. Jørgensen, L. Mosegaard, L. E. Thomsen, T. R. Jensen, and J. C. Hanson. Formation of γ -Fe₂O₃ nanoparticles and vacancy ordering: an in situ x-ray powder diffraction study. *Journal of Solid State Chemistry*, 180(1):180–185, 2007.
- [56] F. Hu, K. W. MacRenaris, E. A. Waters, E. A. Schultz-Sikma, A. L. Eckermann, and T. J. Meade. Highly dispersible, superparamagnetic magnetite nanoflowers for magnetic resonance imaging. *Chemical Communications*, 46(1):73–75, 2010.
- [57] D. Maity, P. Chandrasekharan, P. Pradhan, K.-H. Chuang, J.-M. Xue, S.-S. Feng, and J. Ding. Novel synthesis of superparamagnetic magnetite nanoclusters for biomedical applications. *Journal of Materials Chemistry*, 21(38):14717–14724, 2011.
- [58] F. Fiévet and R. Brayner. The polyol process. In *Nanomaterials: A Danger or a Promise?*, pages 1–25. Springer, 2013.
- [59] D.T. Robb and V. Privman. Model of nanocrystal formation in solution by burst nucleation and diffusional growth. *Langmuir*, 24(1):26–35, 2008.
- [60] V. K. LaMer and R. H. Dinigar. Theory, production and mechanism of formation of monodispersed hydrosols. *Journal of the American Chemical Society*, 72(11):4847–4854, 1950.
- [61] S. E. Skrabalak, B. J. Wiley, M. Kim, E. V. Formo, and Y. Xia. On the polyol synthesis of silver nanostructures: glycolaldehyde as a reducing agent. *Nano*

- letters*, 8(7):2077–2081, 2008.
- [62] D. Caruntu, G. Caruntu, Y. Chen, C. J. O'Connor, G. Goloverda, and V. L. Kolesnichenko. Synthesis of variable-sized nanocrystals of Fe_3O_4 with high surface reactivity. *Chemistry of materials*, 16(25):5527–5534, 2004.
- [63] H. Gavilán, E. H. Sánchez, M. E. F. Brollo, L. Asín, K. K. Moerner, C. Frandsen, F. J. Lázaro, C. J. Serna, S. Veintemillas-Verdaguer, M. Puerto Morales, and L. Gutiérrez. Formation mechanism of maghemite nanoflowers synthesized by a polyol-mediated process. *ACS Omega*, 2(10):7172–7184, 2017.
- [64] N. Singh, G. J. S. Jenkins, R. Asadi, and S. H. Doak. Potential toxicity of superparamagnetic iron oxide nanoparticles (SPION). *Nano reviews*, 1(1):5358, 2010.
- [65] V. Valdiglesias, G. Kiliç, C. Costa, N. Fernández-Bertólez, E. Pásaro, J.P. Teixeira, and B. Laffon. Effects of iron oxide nanoparticles: cytotoxicity, genotoxicity, developmental toxicity, and neurotoxicity. *Environmental and molecular mutagenesis*, 56(2):125–148, 2015.
- [66] N. Scharnagl, S. Lee, B. Hiebl, A. Sisson, and A. Lendlein. Design principles for polymers as substratum for adherent cells. *Journal of Materials Chemistry*, 20(40):8789–8802, 2010.
- [67] S. J. Breusch and K.-D. Kühn. Knochenzemente auf Basis von Polymethylmethacrylat. *Der Orthopäde*, 32(1):41–50, 2003.
- [68] F. Anagnostou, A. Debet, G. Pavon-Djavid, Z. Goudaby, G. Hélyary, and V. Migonney. Osteoblast functions on functionalized PMMA-based polymers exhibiting staphylococcus aureus adhesion inhibition. *Biomaterials*, 27(21):3912–3919, 2006.
- [69] W. F. Mousa, M. Kobayashi, S. Shinzato, M. Kamimura, M. Neo, S. Yoshihara, and T. Nakamura. Biological and mechanical properties of PMMA-based bioactive bone cements. *Biomaterials*, 21(21):2137–2146, 2000.
- [70] U. Ali, K.J. Bt. Abd Karim, and N. A. Buangh. A review of the properties and applications of poly (methyl methacrylate)(PMMA). *Polymer Reviews*, 55(4):678–705, 2015.
- [71] W. He, K.E. Gonsalves, N. Batina, D.B. Poker, E. Alexander, and M. Hudson. Micro/nanomachining of polymer surface for promoting osteoblast cell adhesion. *Biomedical Microdevices*, 5(2):101–108, 2003.
- [72] Louis De Broglie. *Recherches sur la théorie des quanta*. PhD thesis, Migration-université en cours d'affectation, 1924.
- [73] E. Abbe. Beiträge zur Theorie des Mikroskops und der mikroskopischen Wahrnehmung. *Archiv für mikroskopische Anatomie*, 9(1):413–468, 1873.

- [74] J. Thomas and T. Gemming. *Analytische Transmissionselektronenmikroskopie*. Springer, 2013.
- [75] M. Mulisch and U. Welsch. *Romeis-Mikroskopische Technik*. Springer-Verlag, 2015.
- [76] C. A. Schneider, W. S. Rasband, and K. W. Eliceiri. NIH Image to ImageJ: 25 years of image analysis. *Nature methods*, 9(7):671–675, 2012.
- [77] L. Reimer. *Scanning Electron Microscopy*. Springer, 1998.
- [78] S. Lenz, H. Stegmann, and K. Tsyrlin. Efficient separation of secondary and backscattered electrons with a single detector. *Karl Zeiss Microscopy (technical report)*, 2013.
- [79] E. Burkel. Introduction to X-ray scattering. *Journal of Physics: Condensed Matter*, 13(34):7477–7498, 2001.
- [80] J. Als-Nielsen and D. McMorrow. *Elements of modern X-ray physics*. John Wiley & Sons, 2011.
- [81] N. Schell, A. King, F. Beckmann, H. U. Ruhnau, R. Kirchhof, R. Kiehn, M. Müller, and A. Schreyer. The high energy materials science beamline (HEMS) at PETRA III. volume 1234, pages 391–394. AIP, 2010.
- [82] N. Schell, A. King, F. Beckmann, T. Fischer, M. Müller, and A. Schreyer. The high energy materials science beamline (HEMS) at PETRA III. volume 772, pages 57–61. Trans. Tech. Publ., 2014.
- [83] H. M. Rietveld. A profile refinement method for nuclear and magnetic structures. *Journal of applied Crystallography*, 2(2):65–71, 1969.
- [84] L. Lutterotti. Introduction to Diffraction and the Rietveld Method. <http://www.ing.unitn.it/~luttero/laboratoriomateriali//RietveldRefinements.pdf>. [Online; accessed 01-June-2018].
- [85] L. Spieß, G. Teichert, R. Schwarzer, H. Behnken, and C. Genzel. *Moderne Röntgenbeugung: Röntgendiffraktometrie für Materialwissenschaftler, Physiker und Chemiker*. Springer-Verlag, 2009.
- [86] B.H. Toby. R factors in Rietveld analysis: how good is good enough? *Powder diffraction*, 21(1):67–70, 2006.
- [87] L. Lutterotti, M. Bortolotti, G. Ischia, I. Lonardelli, and H.R. Wenk. Rietveld texture analysis from diffraction images. *Zeitschrift für Kristallographie Supplements*, 26:125–130, 2007.
- [88] L. Lutterotti, S. Matthies, H. R. Wenk, A. S. Schultz, and J. W. Richardson. Combined texture and structure analysis of deformed limestone from time-of-flight neutron diffraction spectra. *Journal of Applied Physics*, 81(2):594–600,

- 1997.
- [89] R.L. Mössbauer. Kernresonanzfluoreszenz von Gammastrahlung in Ir 191. *Zeitschrift für Physik*, 151(2):124–143, 1958.
- [90] D.P.E. Dickson and F.J. Berry, editors. *Mössbauer Spectroscopy*. Cambridge University Press, 1986.
- [91] H. Frauenfelder. *The Mössbauer Effect*. W. A. Benjamin, Inc., New York, 1962.
- [92] P. Gütlich. Physikalische Methoden in der Chemie: Mößbauer-Spektroskopie I. *Chemie in unserer Zeit*, 4(5):133–144, 1970.
- [93] H. Wegener. *Der Mössbauer-Effekt und seine Anwendungen in Physik und Chemie*. Hochschultaschenbücher-Verlag, Mannheim, 2. edition, 1966.
- [94] Y. Chen and D. Yang. *Mössbauer effect in lattice dynamics: experimental techniques and applications*. John Wiley & Sons, 2007.
- [95] I. Vincze, I. A. Campbell, and A. J. Meyer. Hyperfine field and magnetic moments in bcc Fe-Co and Fe-Ni. *Solid State Communications*, 15(9):1495–1499, 1974.
- [96] G. M. da Costa, E. de Grave, and R. E. Vandenberghe. Mössbauer studies of magnetite and Al-substituted maghemites. *Hyperfine Interactions*, 117:207–243, 1998.
- [97] I. N. Zakharova, M. A. Shipilin, V. P. Alekseev, and A. M. Shipilin. Mössbauer study of maghemite nanoparticles. *Technical Physics Letters*, 38:55–58, 2012.
- [98] K. Lagarec and D. G. Rancourt. Recoil - Mössbauer spectral analysis software for Windows. *University of Ottawa, Ottawa, ON*, 1998.
- [99] M. Balanda. AC susceptibility studies of phase transitions and magnetic relaxation: conventional, molecular and low-dimensional magnets. *Acta Phys. Pol. A*, 124(6):964–976, 2013.
- [100] F. Ludwig, O. Kazakova, L.F. Barquín, A. Fornara, L. Trahms, U. Steinhoff, P. Svedlindh, E. Wetterskog, Q.A. Pankhurst, P. Southern, P. Morales, M.F. Hansen, C. Frandsen, E. Olsson, S. Gustafsson, N. Gehrke, K. Lüdtke-Buzug, C. Grüttner, C. Jonasson, and C. Johansson. Magnetic, structural, and particle size analysis of single-and multi-core magnetic nanoparticles. *IEEE transactions on magnetics*, 50(11):1–4, 2014.
- [101] A. P. Astalan, C. Jonasson, K. Petersson, J. Blomgren, D. Ilver, A. Krozer, and C. Johansson. Magnetic response of thermally blocked magnetic nanoparticles in a pulsed magnetic field. *Journal of Magnetism and Magnetic Materials*, 311(1):166–170, 2007.
- [102] F. Ahrentorp, A.P. Astalan, C. Jonasson, J. Blomgren, B. Qi, O.T. Mefford, M. Yan, J. Courtois, J.-F. Berret, J. Fresnais, O. Sandre, S. Dutz, R. Müller, and C. Jo-

- hansson. Sensitive high frequency ac susceptometry in magnetic nanoparticle applications. In *AIP Conference Proceedings*, volume 1311, pages 213–223. AIP, 2010.
- [103] M. Alderighi, G. Bevilacqua, V. Biancalana, A. Khanbekyan, Y. Dancheva, and L. Moi. A room-temperature alternating current susceptometer - data analysis, calibration, and test. *Review of Scientific Instruments*, 84(12):125105, 2013.
- [104] R.B. Goldfarb and J.V. Minervini. Calibration of AC susceptometer for cylindrical specimens. *Review of scientific instruments*, 55(5):761–764, 1984.
- [105] P.J.W. Debye. *Polar molecules*. Chemical Catalog Company, Incorporated, 1929.
- [106] R.M. Ferguson, A.P. Khandhar, C. Jonasson, J. Blomgren, C. Johansson, and K.M. Krishnan. Size-dependent relaxation properties of monodisperse magnetite nanoparticles measured over seven decades of frequency by AC susceptometry. *IEEE transactions on magnetics*, 49(7):3441–3444, 2013.
- [107] F. Ludwig, C. Balceris, C. Jonasson, and C. Johansson. Analysis of ac susceptibility spectra for the characterization of magnetic nanoparticles. *IEEE Transactions on Magnetism*, 53(11):1–4, 2017.
- [108] G. Binnig, C.F. Quate, and Ch. Gerber. Atomic force microscope. *Physical review letters*, 56(9):930, 1986.
- [109] B. Voigtländer. *Scanning Probe Microscopy*. Springer, 2016.
- [110] E. Meyer, H. J. Hug, and R. Bennewitz. *Scanning probe microscopy: the lab on a tip*. Springer Science & Business Media, 2013.
- [111] R. García and R. Pérez. Dynamic atomic force microscopy methods. *Surface science reports*, 47(6-8):197–301, 2002.
- [112] L.L. Westra, A.W. Mitchell, and D.J. Thomson. Tip artifacts in atomic force microscope imaging of thin film surfaces. *Journal of Applied Physics*, 74(5):3608–3610, 1993.
- [113] J.D. Miller, S. Veeramasuneni, J. Drelich, M.R. Yalamanchili, and G. Yamauchi. Effect of roughness as determined by atomic force microscopy on the wetting properties of PTFE thin films. *Polymer Engineering & Science*, 36(14):1849–1855, 1996.
- [114] K. L. Westra and D.J. Thomson. Effect of tip shape on surface roughness measurements from atomic force microscopy images of thin films. *Journal of Vacuum Science & Technology B: Microelectronics and Nanometer Structures Processing, Measurement, and Phenomena*, 13(2):344–349, 1995.
- [115] D. Nečas and P. Klapetek. Gwyddion: an open-source software for SPM data analysis. *Central European Journal of Physics*, 10:181–188, 2012.

- [116] K. Witte, W. Bodnar, T. Mix, N. Schell, G. Fulda, T.G. Woodcock, and E. Burkel. A detailed study on the transition from the blocked to the superparamagnetic state of reduction-precipitated iron oxide nanoparticles. *Journal of Magnetism and Magnetic Materials*, 403:103–113, 2016.
- [117] W.J. Schuele, S. Shtrikman, and D. Treves. Observation of superparamagnetism by the mössbauer effect. *Journal of Applied Physics*, 36(3):1010–1011, 1965.
- [118] R. Hergt, S. Dutz, R. Müller, and M. Zeisberger. Magnetic particle hyperthermia: nanoparticle magnetism and materials development for cancer therapy. *Journal of Physics: Condensed Matter*, 18(38):S2919–S2934, 2006.
- [119] N.G. Semaltianos. Spin-coated PMMA films. *Microelectronics Journal*, 38(6):754–761, 2007.
- [120] S. H. Messaddeq, S. H. Pulcinelli, C. V. Santilli, A. C. Guastaldi, and Y. Messaddeq. Microstructure and corrosion resistance of inorganic-organic (ZrO₂-PMMA) hybrid coating on stainless steel. *Journal of Non-Crystalline Solids*, 247(1-3):164–170, 1999.
- [121] M. Lefort, G. Popa, E. Seyrek, R. Szamocki, O. Felix, J. Hemmerlé, L. Vidal, J.-C. Voegel, F. Boulmedais, G. Decher, and P. Schaaf. Spray-on organic/inorganic films: a general method for the formation of functional nano- to microscale coatings. *Angewandte Chemie International Edition*, 49(52):10110–10113, 2010.
- [122] N. F. Poth. *Applikation von Nanopartikeln als Implantatbeschichtung zur Präsentation von biologisch aktivem BMP-2 an Implantatoberflächen*. PhD thesis, Technische Universität Braunschweig, 2015.
- [123] Silverline Airbrush Manual. www.silverlinetools.com/General/GetImage.ashx?ImageType=PDF&ImageSize=&ImageID=380158_Manual.pdf. [Online; accessed 01-August-2018].
- [124] S. Mørup, M. Hansen, and C. Frandsen. Magnetic interactions between nanoparticles. *Beilstein journal of nanotechnology*, 1:182, 2010.
- [125] K. L. Pisane, E. C. Despeaux, and M. S. Seehra. Magnetic relaxation and correlating effective magnetic moment with particle size distribution in maghemite nanoparticles. *Journal of Magnetism and Magnetic Materials*, 384:148–154, 2015.
- [126] S.J. Hitchcock, N.T. Carroll, and M.G. Nicholas. Some effects of substrate roughness on wettability. *Journal of Materials Science*, 16(3):714–732, 1981.
- [127] R.N. Wenzel. Resistance of solid surfaces to wetting by water. *Industrial & Engineering Chemistry*, 28(8):988–994, 1936.
- [128] R. H. Müller, C. Jacobs, and O. Kayser. Nanosuspensions as particulate drug formulations in therapy: rationale for development and what we can expect for the future. *Advanced drug delivery reviews*, 47(1):3–19, 2001.

Acknowledgement

The author is grateful for the scientific and methodical advice and the encouragement received from the supervisor Prof. Dr. Eberhard Burkel, head of the New Materials working group, during the course of this dissertation project. Also, he thanks Dr. Kerstin Witte and Dr. Wiktor Bodnar, at the time members of the working group, for their substantial scientific input and detailed feedback, as well as for their great efforts enabling synchrotron measurements, in giving an introduction to Mössbauer spectroscopy, and in providing titanium plates.

The author wishes to acknowledge Dr. Armin Springer at the Electron Microscopy Centre, University Medicine Rostock, for producing the TEM and SEM images used in this work and for the very helpful discussions, Fritz Westphal and his staff at micromod Partikeltechnologie GmbH for performing dynamic susceptibility measurements, and Dr. Norbert Schell of Helmholtz Centre Geesthacht for supporting the high energy X-ray diffraction measurements.

The author expresses his gratitude towards the whole New Materials working group, including Abdullah Riaz, Adwaa Ahmed and Dr. Martin Hantusch for the collegial cooperation and support, towards secretary Ulrike Schröder for her most kind support in all administrative affairs and towards assistant Bärbel Przybill for her big help in acquiring chemicals and labware, as well as for her assistance working in the laboratory.

It was with great pleasure that the author got to supervise bachelor and master theses of Jakob Wolansky and Dan-Eric Pfahl and got to host internship students Mariana Mendes, Maria Marchenko and Pavel Evdokimov, all of which contributed to the success of this project.

Finally, the author thanks DFG graduate school "WELISA" for funding and for providing a stimulating environment for the research on electric interactions of implants with biosystems.

Selbstständigkeitserklärung

Hiermit versichere ich an Eides statt, dass ich die vorliegende Arbeit selbstständig angefertigt und ohne fremde Hilfe verfasst habe, keine außer den von mir angegebenen Hilfsmitteln und Quellen dazu verwendet habe und die den benutzten Werken inhaltlich und wörtlich entnommenen Stellen als solche kenntlich gemacht habe.

Rostock, 26.04.2019